ตัวเร่งปฏิกิริยาแพลทินัมกระจายตัวสูงและอะตอมเดี่ยวบนตัวรองรับซิลิกา-อะลูมินาสำหรับ
ปฏิกิริยาออกซิเดชันของคาร์บอนมอนอกไซด์และดีไฮโดรจิเนชันของโพรเพน

นายณัชพล โชติกไกร

วิทยานิพนธ์นี้เป็นส่วนหนึ่งของการศึกษาตามหลักสูตรปริญญาวิศวกรรมศาสตรดุษฎีบัณฑิต
สาขาวิชาวิศวกรรมเคมี ภาควิชาวิศวกรรมเคมี
คณะวิศวกรรมศาสตร์ จุฬาลงกรณ์มหาวิทยาลัย
ปีการศึกษา 2558
ลิขสิทธิ์ของจุฬาลงกรณ์มหาวิทยาลัย

HIGHLY DISPERSED AND A SINGLE-SITE PLATINUM CATALYSTS
SUPPORTED ON SILICA-ALUMINA FOR CO OXIDATION AND PROPANE
DEHYDROGENATION

Mr. Nutchapon Chotigkrai
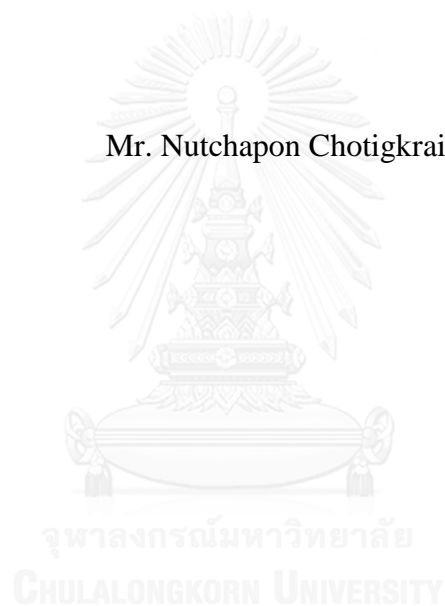
A Dissertation Submitted in Partial Fulfillment of the Requirements

for the Degree of Doctor of Engineering Program in Chemical Engineering

Department of Chemical Engineering

Faculty of Engineering

Chulalongkorn University

Academic Year 2015

Thesis Title	HIGHLY DISPERSED AND A SINGLE-SITE PLATINUM CATALYSTS SUPPORTED ON SILICA-ALUMINA FOR CO OXIDATION AND PROPANE DEHYDROGENATION
By	Mr. Nutchapon Chotigkrai
Field of Study	Chemical Engineering
Thesis Advisor	Professor Piyasan Praserthdam, Dr.Ing.
Thesis Co-Advisor	Professor Bruce C. Gates, Ph.D.

Accepted by the Faculty of Engineering, Chulalongkorn University in Partial Fulfillment of the Requirements for the Doctoral Degree

....Dean of the Faculty of Engineering
(Professor Bundhit Eua-arporn, Ph.D.)

THESIS COMMITTEE

....Chairman
(Associate Professor Kasidit Nootong, Ph.D.)

....Thesis Advisor
(Professor Piyasan Praserthdam, Dr.Ing.)

....Thesis Co-Advisor
(Professor Bruce C. Gates, Ph.D.)

....Examiner
(Associate Professor Joongjai Panpranot, Ph.D.)

....Examiner
(Chutimon Satirapipathkul, D.Eng.)

....External Examiner
(Kanokwan Ngaosuwan, D.Eng.)

ฉัชพล โชติกไกร : ตัวเร่งปฏิกิริยาแพลทินัมกระจายตัวสูงและอะตอมเดี่ยวบนตัวรองรับซิลิกา-อะลูมินาสำหรับปฏิกิริยาออกซิเดชันของคาร์บอนมอนอกไซด์และดีไฮโดรจิเนชันของโพรเพน (HIGHLY DISPERSED AND A SINGLE-SITE PLATINUM CATALYSTS SUPPORTED ON SILICA-ALUMINA FOR CO OXIDATION AND PROPANE DEHYDROGENATION) อ.ที่ปรึกษาวิทยานิพนธ์หลัก: ศ. ดร. ปิยะสาร ประเสริฐธรรม, อ.ที่ปรึกษาวิทยานิพนธ์ร่วม: ศ. ดร. บรูซ ซี เกทส์, 119 หน้า.

การปรับเปลี่ยนคุณลักษณะของตัวรองรับซิลิกา-อะลูมินาสามารถทำได้สามวิธีการเพื่อให้ได้ตัวเร่งปฏิกิริยาแพลทินัมที่กระจายตัวสูงโดยเฉพาะอย่างยิ่งอะตอมเดี่ยวสำหรับปฏิกิริยาออกซิเดชันของคาร์บอนมอนอกไซด์และดีไฮโดรจิเนชันของโพรเพน วิธีการดังกล่าวประกอบด้วยการมีเฟสผสมไดคอะลูมินาในแกมมาอะลูมินาและการเติมซิลิกาลงในแกมมาอะลูมินาด้วยวิธีโซลโวเทอร์มอล มีการปรับเปลี่ยนปริมาณซิลิกาของตัวรองรับแกมมาอะลูมินาเจือด้วยซิลิกาด้วยการเคลือบฝังแบบแห้งและใช้ซีโอไลท์เคแอลทีแอลซึ่งเป็นตัวรองรับที่มีความเป็นผลึกสูง ผลการทดลองแสดงให้เห็นว่าการกระจายตัวของแพลทินัมสามารถเพิ่มอย่างมากโดยการมีเฟสผสมไดคอะลูมินาและซิลิกาในแกมมาอะลูมินา แรงอันตรกิริยาของแพลทินัมและตัวรองรับแข็งแรงขึ้นบนอะลูมินาเจือด้วยซิลิกาโดยเฉพาะอย่างยิ่งเมื่อซิลิกามีปริมาณน้อยซึ่งจะสนับสนุนการกระจายตัวสูงของแพลทินัม ผลของการทดสอบด้วยออกซิเดชันของคาร์บอนมอนอกไซด์แสดงให้เห็นความสัมพันธ์แบบเส้นตรงของความว่องไวต่อตำแหน่งและปริมาณพื้นผิวด่างของตัวรองรับบ่งชี้ว่าการเคลื่อนที่ของออกซิเจนเป็นอีกปัจจัยที่ควบคุมการเกิดปฏิกิริยาบนพื้นผิวระหว่างคาร์บอนมอนอกไซด์และออกซิเจนที่กระตุ้นโดยแพลทินัมต่างตำแหน่งที่ใกล้กัน ความว่องไวต่อตำแหน่งของตัวเร่งปฏิกิริยาสำหรับปฏิกิริยาดีไฮโดรจิเนชันของโพรเพนค่อนข้างคงที่ทำให้กลไกนี้น่าเชื่อถือมากขึ้น นอกจากนี้ตัวเร่งปฏิกิริยาแพลทินัมกระจายตัวสูงเหล่านี้ยังสามารถประยุกต์ใช้ในปฏิกิริยาดีไฮโดรจิเนชันของโพรเพนเนื่องจากผลเชิงบวกต่อความว่องไวและการเลือกเกิดเป็นโพรพิลีน เป็นที่น่าสนใจเมื่อกระจายแพลทินัมบนซีโอไลท์เคแอลทีแอล ซึ่งเป็นครั้งแรกที่นำเสนอตัวเร่งปฏิกิริยาแพลทินัมอะตอมเดี่ยวพร้อมด้วยโครงสร้างและตำแหน่งที่ชัดเจน สเปคตราของอินฟราเรดและการดูดซับรังสีเอกซ์และรูปภาพอิเล็กตรอนบ่งชี้ถึงโครงสร้างและตำแหน่งของสารประกอบแพลทินัมในรูพรุนของซีโอไลท์ซึ่งพิสูจน์ให้เห็นพันธะระหว่างแพลทินัมและตัวรองรับและความสัมพันธ์ระหว่างโครงสร้างกับศักยภาพการเร่งของตำแหน่งที่ว่องไว นอกจากนี้ตัวเร่งปฏิกิริยาแพลทินัมอะตอมเดี่ยวสามารถจัดว่าเป็นเป็นตำแหน่งเร่งปฏิกิริยาอุดมคติในปฏิกิริยาที่ไม่สัมพันธ์กับโครงสร้าง

ภาควิชา	วิศวกรรมเคมี	ลายมือชื่อนิสิต	_____
สาขาวิชา	วิศวกรรมเคมี	ลายมือชื่อ อ.ที่ปรึกษาหลัก	_____
ปีการศึกษา	2558	ลายมือชื่อ อ.ที่ปรึกษาร่วม	_____

5371827021 : MAJOR CHEMICAL ENGINEERING

KEYWORDS: SINGLE-SITE PLATINUM CATALYST, METAL-SUPPORT INTERACTION, O2 MOBILITY, CO OXIDATION, C3H8 DEHYDROGENATION

NUTCHAPON CHOTIGKRAI: HIGHLY DISPERSED AND A SINGLE-SITE PLATINUM CATALYSTS SUPPORTED ON SILICA-ALUMINA FOR CO OXIDATION AND PROPANE DEHYDROGENATION. ADVISOR: PROF. PIYASAN PRASERTHDAM, Dr.Ing., CO-ADVISOR: PROF. BRUCE C. GATES, Ph.D., 119 pp.

The characteristics of SiO_2-Al_2O_3 supports were tuned by three strategies in order to achieve highly dispersed, especially single-atom Pt sites using for CO oxidation or propane dehydrogenation (PDH). The strategies include incorporation of χ-Al_2O_3 and Si into γ-Al_2O_3 via solvothermal, variation of SiO_2 content of Si-doped γ-Al_2O_3 via dry impregnation, and use of KLTL zeolite as a highly crystalline support. The results showed that dispersity could be effectively enhanced by incorporating dopants (χ-Al_2O_3 and Si). Pt-support interaction was particularly strengthened on Si-doped Al_2O_3 at low SiO_2 loading, promoting highly dispersed Pt sites. The results from CO oxidation tests revealed a linear relationship between TOFs and amount of surface basicity of modified supports. It is suggested oxygen mobility plays a distinct role in controlling the surface reaction between CO^* and O^*, which were activated by different adjacent Pt sites. The proposed mechanism was strengthened by the TOFs of the modified catalysts in PDH remained unchanged. In addition, these highly dispersed Pt catalysts can also be applied in PDH due to the promotional effect on activity and selectivity to propylene. Interestingly, when dispersed Pt on KLTL zeolite, the first site-isolated mononuclear Pt catalyst with a well-defined structures and locations is presented. IR and X-ray absorption spectra and electron micrographs determine the structures and locations of the Pt complexes in the zeolite pores, demonstrate the platinum support bonding, and relationship between active site structures and catalytic performance. Furthermore, the single-atom Pt catalysts can be accounted as ideally catalytic sites in structure-insensitive reactions.

Department:	Chemical Engineering	Student's Signature	....
Field of Study:	Chemical Engineering	Advisor's Signature	....
Academic Year:	2015	Co-Advisor's Signature	....

ACKNOWLEDGEMENTS

CONTENTS

LIST OF TABLES

LIST OF FIGURES

จุฬาลงกรณ์มหาวิทยาลัย
CHULALONGKORN UNIVERSITY

CHAPTER 1
INTRODUCTION

1.1 Inspiration

Supported noble metal catalysts are essential for several important chemical reactions [1, 2]. In particular, supported platinum catalyst is one of the most practical solid catalysts because of its excellent activity and stability for a variety of industrial applications [3-5]. Platinum is expensive, which led to several attempts point out to improve atomic efficiency such as metal dispersity, atomic activity, stability in reaction conditions, etc. Of particular interest is the highly dispersed and even atomically dispersed metal catalysts that can be stabilized on a variety of supports, as discussed in recent reviews [6, 7]. Accordingly, the properties of metal function including dispersed-state, stability and catalytic activity are well-established to be sensitive to the characteristics of support such as composition, acid-base properties, hierarchical pore structures, metal-support interaction, redox potential and etc. [8, 9]. Consequently, modifications of inexpensive high-area porous supports have received very broad attention, in the hope that industrial relevant catalysts with great performance and low cost will be effectively developed [10].

γ-Al$_2$O$_3$ has been widely used as a commercial supporting material for Pt catalyst in many petroleum plants [11, 12]. Therefore, modifications of the Al$_2$O$_3$ support have been extremely interested in order to improve the catalytic properties. One interesting manner to improve the Al$_2$O$_3$ properties according to previous works of our group was to incorporate χ-phase Al$_2$O$_3$ into γ-Al$_2$O$_3$ support via solvothermal method. It has been reported that mixed χ and γ phase Al$_2$O$_3$ supported Pt and Co catalysts revealed higher activity in CO oxidation [13] and hydrogenation [14], respectively, corresponding to the promotion of higher metal dispersity. Furthermore, addition of other elements such as Ti, La, Ce, Sn and Si has also been widely studied [15-18], as dramatically enhanced catalytic properties in their cases. Si is one of great promoters that can enhance properties of Al$_2$O$_3$ support including thermal stability, acidity, sulfur tolerance and surface area [19-21]. Both χ-Al$_2$O$_3$ and Si incorporation

into γ-Al$_2$O$_3$ via solvothermal method could enhance Pt dispersion of Al$_2$O$_3$ supported catalysts which is expected to be main cause in CO oxidation activity, as generally used to investigate catalytic performance of supported metal catalysts owing to its well-defined mechanisms and practical significance for CO elimination [22-24]. Additionally, the oxygen mobility of the supports seems to be another important influence in oxidation reactions [25, 26]. Nevertheless, the effects of support modification by χ-phase Al$_2$O$_3$ and Si addition as well as SiO$_2$ loading on the oxygen mobility have rarely been investigated.

In addition, those modified supported Pt catalysts would have potential to be applied in other insensitive-structure reactions such as propane dehydrogenation [27], due to the positive effect of Pt dispersion. As propylene is such an important feedstock in chemical industry employing in the production of a widespread of chemicals such as polypropylene, propylene oxide, and acrylonitrile [28, 29]. Propane dehydrogenation is a commercial propylene production process that has gained wide attention in recent years owing to the rise of propylene prices [30]. Propane dehydrogenation is a highly endothermic process, requiring a raised reaction temperature (regularly above 500 ^{o}C) to achieve a satisfactory yield of propylene. The severe condition promotes coke formation and hydrocarbon cracking, resulting in low selectivity to propylene and catalyst in stability [31]. Pt/Al$_2$O$_3$ based catalyst is also one of commercial catalysts using in this reaction owing to its catalytically active, thermal stability and good selectivity to propylene in the given conditions [27]. However, the Pt/Al$_2$O$_3$ based catalysts are still suffering from coking, Pt sintering and low propylene yield, which are challenging for development. Therefore, the catalyst has been modified by various strategies in order to improve the catalytic performance and stability. Various methods have been adopted including changing support [32] or adding promoters such as Sn, Na, and K [18, 33-35]. PtSn alloy exhibited the excellent properties for propane dehydrogenation due to its neutralization of strong acid sites, reduction of Pt ensemble sites and promotion of coke spillover to support [18, 33]. This leads to attain high catalytic performance and stability. Na and K were doped in order to poison the strong acid sites of Al$_2$O$_3$ support, suppressing coke formation and side reaction selectivity [34, 35], and stabilizing dispersed state of Pt sites [10]. Ti and Ce were also studied for doping into Pt/Al$_2$O$_3$ based catalyst, taking

the promotional effect of metal-support interaction for propane dehydrogenation. Titanium was found to facilitate the migration of coke precursors from the metal surface to support affected by the increase of electron density of Pt [31], while Ce enhanced the reducibility and dispersity of Pt nanoparticles. The Ce-doped catalysts exhibited more activity and less coke deposition [17]. Silica-alumina system is well known as thermally stable support, it has been employed as support for Pt catalyst performing at mild to high temperature [36, 37]. Moreover, Pt dispersion was also promoted when supported on the silica-alumina system compared to pure silica or alumina [38]. These characteristics are expected to give advantage in the structure-insensitive reaction of propane dehydrogenation. Whereas amorphous silica-alumina or Si-doped Al_2O_3 (normally SiO_2 contents > 30 wt%) have been considered as highly acidic support [39, 40] which is noted to be inappropriate choice of supports for propane dehydrogenation because of promotion of coke formation and side reactions. Nevertheless, the effect of doping low amount of Si (SiO_2 contents < 15 wt%) into Pt/γ-Al_2O_3 catalyst has not often been studied [37] and to the best of our knowledge, using the doped catalysts for propane dehydrogenation has not been investigated.

Nowadays, single-site noble metals on metal oxide supports have gained wide attention because of the new opportunities they offer in catalysis including highest dispersed states, narrowest particles sizes distribution, highly structural uniformity of metal active species. All of these positive characteristics encourage a synthesis of highly selective catalyst and a way to approach fundamental understanding [6, 41, 42]. However, when the support surfaces are nonuniform, the structures of the catalytic species are also nonuniform and challenging to characterize. For example, site-isolated Pt atoms have been observed along with small platinum clusters in catalysts like those applied in industry at temperatures as high as about 510 $^{\circ}$C [43], and isolated Pt atoms on Al_2O_3 are stable at 260 $^{\circ}$C [8]. The metal atoms in some such catalysts have been imaged by aberration-corrected scanning transmission electron microscopy (STEM) [6, 8, 41-43]. In contrast, when the supports are crystalline, they present nearly uniform surface sites for bonding of catalytic species, allowing determination of their locations in the pores, for example, for mononuclear gold in zeolite NaY [44]. Therefore, KLTL zeolite was considered to be great candidate as highly crystalline support because it is applied industrially as a support for platinum,

present in clusters of only a few atoms each, in catalysts used for alkane dehydrocyclization [45].

1.2 Objectives

To investigate the effect of oxygen mobility for highly dispersed and single-site Pt catalysts supported on tuned-characteristic supports in probe reactions including CO oxidation and propane dehydrogenation as follows;

1. To compare the effects of χ phase- and Si-modified γ-Al_2O_3 supported Pt catalysts via solvothermal method in CO oxidation
2. To investigate the effect of SiO_2 content on Pt dispersed-states and oxygen mobility of Si-doped γ-Al_2O_3 supported Pt catalyst in CO oxidation
3. To determine the promotional effect of Si-doped γ-Al_2O_3 supported Pt catalyst for propane dehydrogenation
4. To define the structures and locations of single-site Pt catalysts supported on KLTL zeolite and establish the structure-activity correlation via combination of microscopic and spectroscopic methods.

1.3 Scope of work

1. Effects of χ phase- and Si-modified γ-Al_2O_3 supported Pt catalysts in CO oxidation.

   1.1 Synthesis of unmodified, χ phase- and Si-modified γ-Al_2O_3 via solvothermal method.

   1.2 Preparation of supported Pt catalysts with various Pt loadings (0.3, 0.5 and 1 wt. %).

   1.3 Characterization of the catalysts by XRD, N_2-physisorption, CO-pulse chemisorption, SEM-EDX and CO_2-TPD.

   1.4 Catalysis test in CO oxidation.

2. Effects of SiO_2 content on Pt dispersion and oxygen mobility in CO oxidation, and the promotional effect for propane dehydrogenation of Si-doped γ-Al_2O_3 supported Pt catalysts.

    2.1 Synthesis of Si-doped γ-Al_2O_3 with varying SiO_2 loadings (0.6, 1.2, 5.6 and 12.4 wt %) via dry impregnation method.

    2.2 Preparation of Si-doped γ-Al_2O_3 supported Pt catalysts.

    2.3 Characterization of the catalysts by XRD, N_2-physisorption, SEM-EDX, NH_3-TPD, CO_2-TPD, XPS, H_2-TPR, CO-pulse chemisorption, CO-TPD and TGA.

    2.4 Catalysis test in CO oxidation

    2.5 Catalysis test in C_3H_8 dehydrogenation.

3. Determination of structures and locations of single-site Pt CO oxidation catalyst in KLTL zeolite.

    3.1 Synthesis of single-site $[Pt(NH_3)_4]^{2+}$ and PtO_x complexes supported on KLTL zeolite.

    3.2 Characterization of the single-site Pt catalysts via combined characterization techniques including EXAFS, XANES, STEM and CO-adsorption FTIR.

    3.3 Catalysis test in CO oxidation.

1.4 Research methodology

```
                    ┌─────────────────────────────────┐
                    │  Tuning characteristics of supports │
                    └─────────────────────────────────┘
                           │                    │
          ┌────────────────────────────┐   ┌──────────────────────┐
          │  Modifications of transition │   │ Highly crystalline support │
          │ crystalline support (γ-Al₂O₃)│   └──────────────────────┘
          └────────────────────────────┘              │
             │                      │                  │
  ┌──────────────────┐  ┌──────────────────────────┐  ┌──────────────┐
  │ Solvothermal synthesis │ │ Incipient wetness impregnation │  │ KLTL zeolite │
  └──────────────────┘  └──────────────────────────┘  └──────────────┘
```

γ-Al$_2$O$_3$ (solvo.) • χ-phase-modified Al$_2$O$_3$ • Si-modified Al$_2$O$_3$ • γ-Al$_2$O$_3$ (comm.) • Ion-exchange of 1 wt% Pt

Vary Pt loadings (0.3, 0.5, 1 wt%)

Vary SiO$_2$ loadings (0.6, 1.2, 5.6, 12.4 wt%)

Calcination

$[Pt(NH_3)_4]^{2+}$/KL   PtO$_x$/KL

xSiAl

0.3 wt% Pt loading

Pt/solvo-modified Al$_2$O$_3$ Pt/xSiAl

Characterization by IR, XANES, EXAFS and STEM

Characterization by XRD, N$_2$-physisorption, SEM-EDX NH$_3$-TPD, CO$_2$-TPD, H$_2$-TPR, CO-pulse chemisorption, TGA

Reaction study in C$_3$H$_8$ dehydrogenation   Reaction study in CO oxidation

CHAPTER 2
THEORY

The aims of this chapter are to provide the fundamental knowledge used in this work of supported Pt catalysts including three parts of synthesis, characterization and CO oxidation test, respectively.

2.1 Metal oxide supports

2.1.1 Al_2O_3

Alumina is extensively used as catalyst, catalyst support, wear-resistance material, ceramic, abrasives, medicinal material, and adsorbent [46, 47] because of its distinctive chemical, mechanical and thermal properties. It has high surface area with fine particle size, good adsorbent, catalytic activity, and high melting point (above 2000 °C) which is also desirable for the support. Al_2O_3 was first used as support for Pt catalyst in 1949 in naphtha reforming process [4].

2.1.1.1 Formation and crystal structure of alumina

Alumina can exist in many metastable phases before transforming to the most stable α-alumina (corundum form). Chi (χ), kappa (κ), eta (η), theta (θ), delta (δ), and gamma (γ) are six primary metastable phases of alumina designated by the Greek letters. The temperature range and sequence of each phase transformation depends upon various factors of starting alumina precursor, for example, degree of crystallinity and amount of impurities [46]. Alumina precursor and calcination condition significantly influence the resulting powder properties. The sequences of phase transformation from alumina precursor to the thermodynamically stable α-alumina phase are irreversible, as depicted in the literatures are also approximates (**Figure 2.1**).
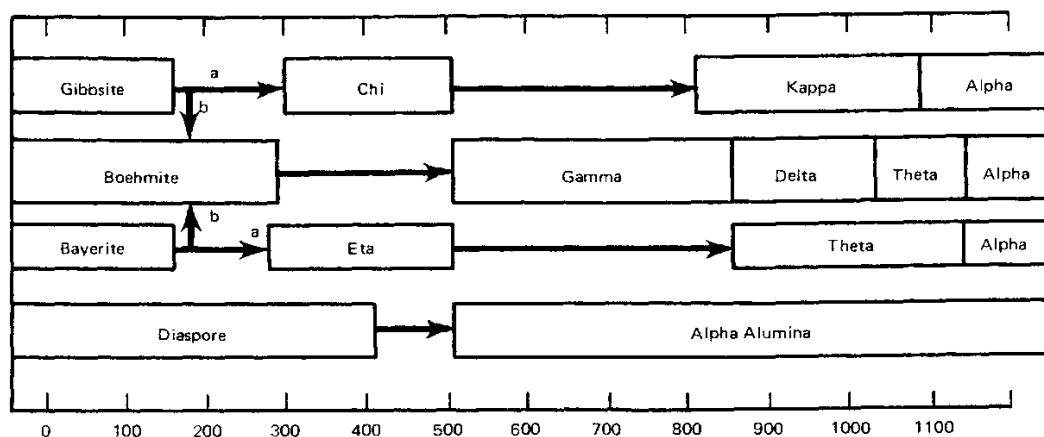
Figure 2.1 Transformation sequences of aluminum hydroxides [47].

Aluminum trihydroxide (Al(OH)$_3$) and aluminum oxide hydroxide (AlOOH) exhibit polymorphism and exist in many forms of structure. The framework of all aluminum hydroxides consists of double oxygen layers stacking with the aluminum ions located in octahedrally coordinated interstices. The symmetry of the overall structure for each hydroxide is determined by the distribution of hydrogen, whereas the packing of oxygen ions inside the layer can be either hexagonal or cubic. It has been suggested that the mechanism of dehydration for the particular hydroxide is controlled by the relative distance between hydroxyl groups, both within and between the layers.

The phase transformation sequence commonly begins with aluminum hydroxides (Al(OH)$_3$ and AlOOH) transforming to low-temperature phase of alumina (η and χ) at temperature around 150-500 ^{o}C, and afterward to high temperature phase (δ, θ, κ) at temperature around 650-1000°C. Finally, α-alumina, the thermodynamically stable phase, is formed at temperature around 1100-1200 ^{o}C.

2.1.2 Zeolites

Zeolites in nature have been known as aluminosilicate minerals for almost 250 years, for instance, faujasite, modernite and ferrierite [48]. Synthetic faujasites were introduced as industrial catalysts for fluid catalytic cracking in 1962. Zeolites are

useful in catalysis applications due to their unique properties including high surface area, uniform pore structure and high acidity [49, 50]. The elementary units of zeolites are tetrahedral oxides of Si and Al atoms. Tetrahedral units are linked with oxygen atom, resulting in three-dimensional framework, presenting in **Figure 2.2.** The framework consist of channels, intersections and cages with various dimensions (0.2 - 1.3 nm) depending on the type of framework. One negative charge at the oxygen bridge of SiO_2 and AlO_2^- unit needs cation to neutralize, in example, alkaline earths and hydronium ion.
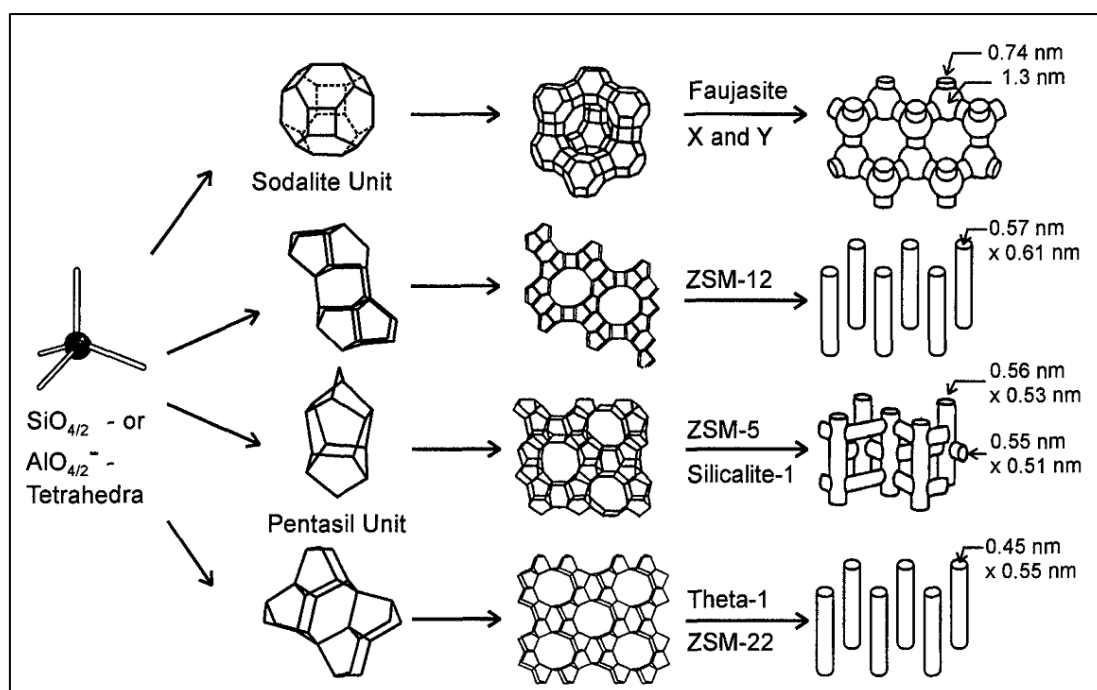
Figure 2.2 Structures of selected zeolites and their micropore systems and dimensions [48].

2.1.2.1 HY zeolite

Y zeolite in H^+ form is the most important as support and catalyst for hydrocarbon cracking [3]. Y zeolite is one sub type of faujasite framework and has chemical formula $[(Ca^{2+}, Mg^{2+}Na^+_2)_{29} (H_2O)_{240}][Al_{58}Si_{134} O_{384}]$. However,

dealumination of Y zeolite has been widely adapted to improve acidity. Three-dimensional model of faujasite framework is shown in **Figure 2.2 (top)**.

2.1.2.2 KLTL zeolite

LTL zeolite is a practical support for metal catalyst for alkane dehydrocyclization [45]. Mostly in form of K ion and has chemical formula $[K^+_6Na^+_3 (H_2O)_{21}][Al_9Si_{27} O_{72}]$. Three-dimensional model of LTL framework is shown in **Figure 2.3 (right)**.
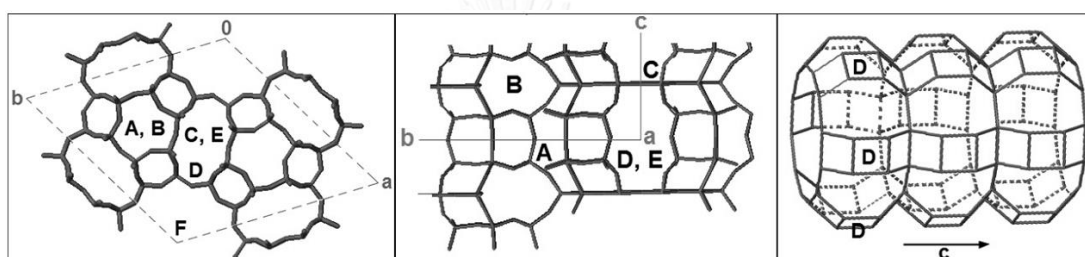
Figure 2.3 Unit cell and possible exchange-sites of zeolite LTL of view along: c-direction (left), a-direction (middle) and main channel (right) [51].

2.2 X-ray absorption spectroscopy

X-ray absorption spectroscopy (XAS) is the spectroscopic technique that provides electronic and structural information of catalysts, especially active metal sites in both reaction conditions and vacuum, as excellently explained by D. C. Koningsberger et al. [52]. The basic principles are that X-ray beam was applied passing through a sample. The intensity will be decreased by the absorption characteristics of the sample. When the energy of X-ray is higher than ionization energy (edge energy) of absorbing atom causes ejection of a core electron. The electron wave oscillates around absorbing atom, when they hit electron of neighboring atoms returning to absorbing atom. The oscillations depend on kind of neighboring atoms and distance between absorbing and neighboring atoms. The oscillation was interpreted to receive the structural information of active metal sites.

2.3 CO oxidation over supported Pt catalysts

CO oxidation is essential for automotive industry and is one of the most widely used in surface chemistry as a model reaction to investigate catalytic behavior of solid catalysts. Pt appears to be the least structure-sensitive for CO oxidation, it was confirmed by Cant [53] as well as Haneda et al. [54], who reported no Pt sizes effect with Pt dispersion 7 to 81% on SiO_2 and Al_2O_3, respectively. The three most popular mechanisms are discussed as follows:

2.3.1 Langmuir-Hinshelwood mechanism

It is widely accepted that CO oxidation over Al_2O_3 supported Pt catalysts occurred according to Langmuir-Hinshelwood mechanism. The CO and O_2 reactants are adsorbed on the same sites, as the elementary steps proposed by Engel and Ertl [22] as follows:

$$CO_{(g)} + Pt_{(s)} \rightarrow CO\text{-}Pt_{(s)}$$
$$O_{2(g)} + Pt_{(s)}\text{-}Pt_{(s)} \rightarrow 2\ O\text{-}Pt_{(s)}$$
$$CO\text{-}Pt_{(s)} + O\text{-}Pt_{(s)} \rightarrow CO_{2(g)} + Pt_{(s)}\text{-}Pt_{(s)}$$
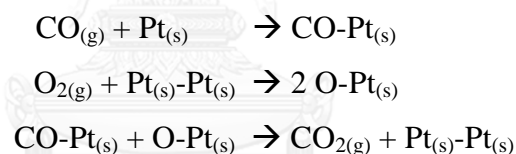
2.3.2 Eley-Rideal mechanism

The Eley-Rideal mechanism is another reaction mechanism proposed for catalytic CO oxidation [84]. In this mechanism a surface reaction does not concern two adsorbed surface species. There is a possibility that the collision between one gas phase-reactant and another adsorbed-reactant leads to reaction and that the product desorbs directly into the gas. Manual et al. [55] proposed this mechanism, which $CO_{(g)}$ directly react on a Rh^{x+} sites environed by oxygen species at vacancy sites.

2.3.3 Mars van Krevelen mechanism

In contrast to Al_2O_3 supported catalysts, it was found that when Ce is added to the support, the oxygen order decreases. This result was determined as the effect of dual-site mechanism. The reactants would be adsorbed on different sites: CO would be adsorbed on metal sites whereas O_2 adsorbed on neighboring ceria sites. The essential effect of ceria addition was reported in many works [56].

2.4 Propane dehydrogenation

The propane dehydrogenation is thermodynamically limited and highly endothermic reactions with heat of reaction equals 124.3 kJ mol^{-1}.

2.4.1 Role of Pt active sites

Propane dehydrogenation is believed to be insensitive to the structure of the platinum particles, which are independent of the particle size or crystallographic plane of platinum sites. Therefore, small particles are preferred owing to only the amount of active sites is relevant. However, undesired side reactions that occur during propane dehydrogenation such as hydrogenolysis, isomerization, and coke formation are sensitive to the structure of the platinum particles. For example, the inverse relationship between Pt particle size and the rate of ethylene hydrogenolysis was established, that such reaction being one of the main causes of coke deposition [57]. Moreover, DFT calculations have been utilized to fulfill the understanding of Pt active sites nature, by calculating the energy barrier of propane dehydrogenation on different crystal planes including flat (111) and stepped (211) Pt crystal planes by Yang et al. [57]. It was found that step sites are more reactive, as the energy barrier to form propylene is much lower on step sites (24 - 34 kJ mol^{-1}) than on the flat surface (63 - 72 kJ mol^{-1}).

2.4.2 Catalyst deactivation

According to the harsh conditions of propane dehydrogenation, which cause the deactivation of Pt-based catalysts by two main processes [27]. First, the high temperature of dehydrogenation and also regeneration result in the agglomeration or sintering of platinum particles. The loss in active sites as a result of sintering causes the drop of catalytic activity in propane dehydrogenation. A second very important factor is coke formation, the side reactions as well as deep dehydrogenation lead to the coverage of active sites by carbon deposition.

2.4.3 Role of acidity

Strong acidic sites are well known as highly active sites for cracking, isomerization and coke formation [32], which are accounted as undesired side reactions. Thus, the limited strong acidity of catalyst is needed to avoid side reactions, which lead to not only higher selectivity by decreasing of side reactions but also better stability by reducing carbon deposited on the active sites.
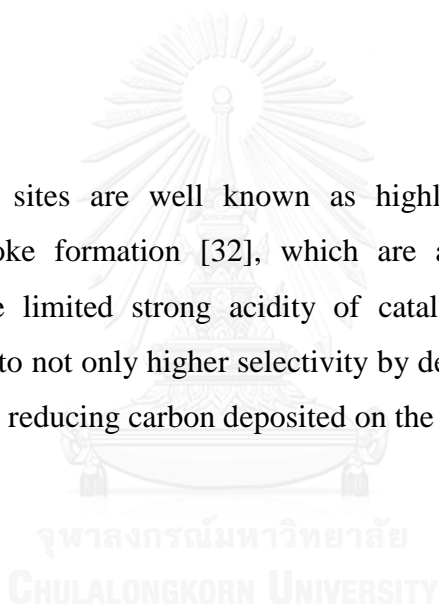
CHAPTER 3
LITERATURE REVIEWS

This chapter summaries previous studies relating to supported Pt catalysts and their applications.

3.1 Supported Pt catalysts

Petroleum refining and processes are such a high value and gigantic impact industry in the world [58, 59]. Many petroleum refining reactions such as alkane reforming, dehydrogenation and cracking are abundantly catalyzed by bi-functional Pt based catalysts [1, 2]. These oxides (Al_2O_3, HY and KL zeolite) are considered as outstanding supports in these reactions. It is well known that metal oxide supports play an important role in reaction with distinct functions; therefore, metal oxides have been used for different desirable purposes [3-5, 45]. For examples, high acidity of HY zeolite is excellent as support for catalyzing hydrocarbon cracking [3]. Acidity of Al_2O_3 is appropriately used for naphtha reforming as well as propane dehydrogenation [4, 5]. Moreover, basicity compared with other zeolites and uniform pore structure of KL zeolite led to selectively produce the desired products such as aromatization of n-hexane to benzene [45].

3.2 Support modifications

3.2.1 Modification of γ-Al_2O_3 by Si addition

The properties of Al_2O_3 support were improved by the addition of other elements such as La, Ti and Si [15, 16]. Si is one of the interesting promoters that can improve properties of Al_2O_3 support including thermal stability, acidity and surface area [19-21]. Solvothermal method gives opportunity to synthesize Si-modified Al_2O_3 in one pot. Moreover, it can be tuned the phase of Al_2O_3 by organic solvents used as

reported by Praserthdam et al. [21]. They investigated thermal stability of synthesized Si-doped Al_2O_3 in various organic solvents and found that 1-butanol resulted in wrinkled sheet particles (γ phase) while toluene resulted in spherical particles (χ phase). The results showed that 1-butanol gave γ-Al_2O_3 having the higher thermal stability than χ-Al_2O_3. For toluene solvent, at low Si content (5-20 at.%) increased thermal stabilities without phase collapse, while at 50 at.% of Si caused amorphous structures [60]. It can be seen that numerous works studied amorphous Si-modified Al_2O_3 synthesized by sol-gel, co-precipitation and grafting methods [61-63].

3.2.2 Modification of γ-Al_2O_3 by χ phase incorporation

From previous work of our group [64, 65], thermally stable χ-Al_2O_3 has been synthesized by solvothermal method in mineral oil and toluene solvents. Various conditions including temperature and holding time significantly affected physicochemical properties of resulting powder. Moreover, χ-Al_2O_3 was also used as a support for Co catalysts and showed good catalytic activity for CO hydrogenation [66]. For this reason, properties of Al_2O_3 support was tried to improve via incorporating of χ-phase Al_2O_3 into γ-Al_2O_3 support by solvothermal method. Meephoka et al. [13] reported that Pt supported on the mixed χ and γ phase Al_2O_3 gave higher CO oxidation activity due to higher Pt dispersion. Pansanga et al. [14] also found higher CO hydrogenation activity of χ-phase incorporated γ-Al_2O_3 supported Co catalysts which were corresponded to higher Co dispersion. The higher dispersion of Pt and Co catalysts may be explained by spherical χ-particle Al_2O_3 were more resistant to agglomeration than on wrinkled sheet γ-Al_2O_3 particles during calcination and CO hydrogenation (reduction atmosphere) [67]. The TEM images clearly showed that wrinkled sheet of γ-Al_2O_3 particles essentially sintered (Fig 3.1(h)) while spherical χ-particles were more stable during CO hydrogenation (Figure 3.1(c) and 3.1(f)).
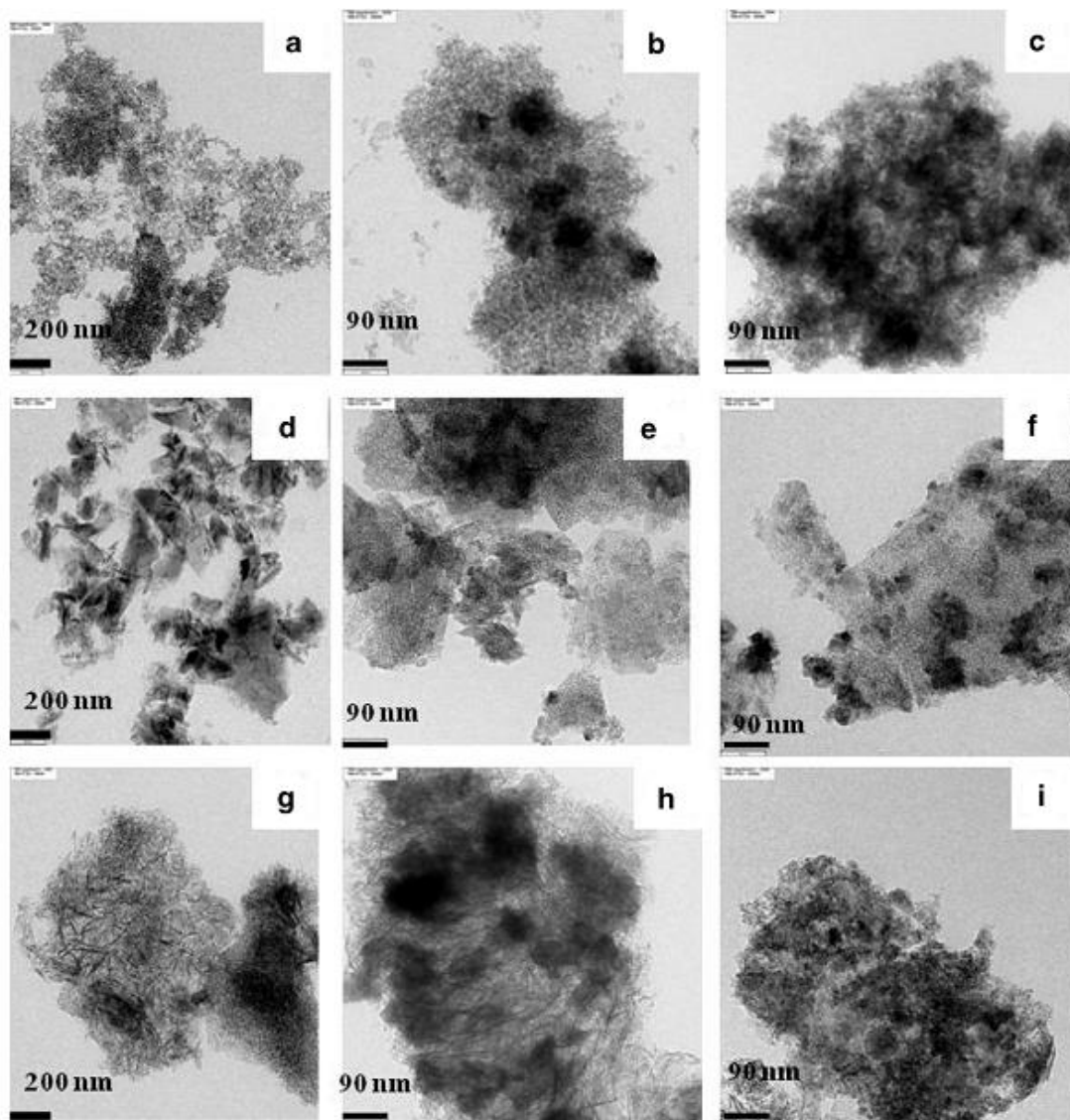
Figure 3.1 The TEM micrographs of χ-SV (a), Co/χ-SV (b), used Co/χ-SV (c), χ-GB (d), Co/χ-GB (e), used Co/χ-GB (f), γ-Al$_2$O$_3$ (g), Co/γ-Al$_2$O$_3$ (h), and used Co/γ-Al$_2$O$_3$ (i) [67].

3.3 Acid-base characteristics of silica-alumina system

It is well known that acid-base properties of materials are essential for catalysis [49, 50]. Aluminosilicates are widely used as catalyst and support for acid catalyzed reactions because they have high specific surface area, high thermal stability, and broad acidic properties [37, 39, 40]. Aluminosilicates can be divided into 2 main groups by their crystallinity comprising amorphous silica-alumina and crystalline zeolite. They are well established to catalyze dehydration, cracking, isomerization, etc., thanks to their great acidic properties. The concentration of total acid sites (Brønsted and Lewis sites) is crucial with distinct role depending on purpose of utilization. For example, the rate of isomerization and hydrocracking is proportional to the Brønsted acid sites [68], while these sites increase rate of side reactions in dehydrogenation such as hydrogenolysis and coking, resulting in low selectivity and rapid deactivation. The concentration of total acid sites (Brønsted and Lewis sites) can be adjusted by tuning Si/Al ratio and calcination temperature [37], as it has been reported that increasing Si/Al ratio (5 - 27 wt% SiO_2) of amorphous silica-alumina increases both the Brønsted and Lewis acid site concentrations. Furthermore, calcination at higher temperatures results in lower both Brønsted acid sites by removing hydroxyl groups in the form of water molecules and also Lewis acid sites by the transformation of unsaturated 5- coordinated Al (a strong Lewis acid) to higher concentrations of 6- and 4- coordinated. Whereas, zeolites are well established as Brønsted rather than Lewis acidic oxides, even both Brønsted and Lewis acid sites occur in nature [48], due to Brønsted acid sites are almost always generated by ion-exchange method as introducing ammonium ions followed by a heat treatment. The density of Brønsted acid sites in a zeolite is clearly correlated to the framework Al content. Moreover, temperature programmed desorption of base molecules such as ammonia and pyridine, and H-NMR characterizing that acid sites of zeolites are significantly stronger than amorphous silica-aluminas.

3.4 Atomically dispersed supported metal catalysts

Atomically dispersed supported metal catalysts have received wide interests due to their advantages including highest atom efficient, high selectivity and well characterization [6]. These highly influence both productive and fundamental understanding applications. Researchers have prepared samples that are structurally uniform and characterizable to address the relationship of their structure and catalytic properties. Because the support is a crucial part of catalytic species and crystalline supports provide nearly uniform surface sites for bonding of catalytic species. Zeolites, are such crystalline supports, are widely used as industrial catalysts and supports, for example, mononuclear iridium atoms supported in pore of zeolite HSSZ-53 [69]. The mononuclear Ir complexes bonded with zeolite HSSZ-53 was prepared by the reaction of $Ir(C_2H_4)_2(acac)$ with zeolite HSSZ-53. The STEM images show individual Ir atoms atomically dispersed inside the pore and undetectable iridium clusters (**Figure 3.2**).
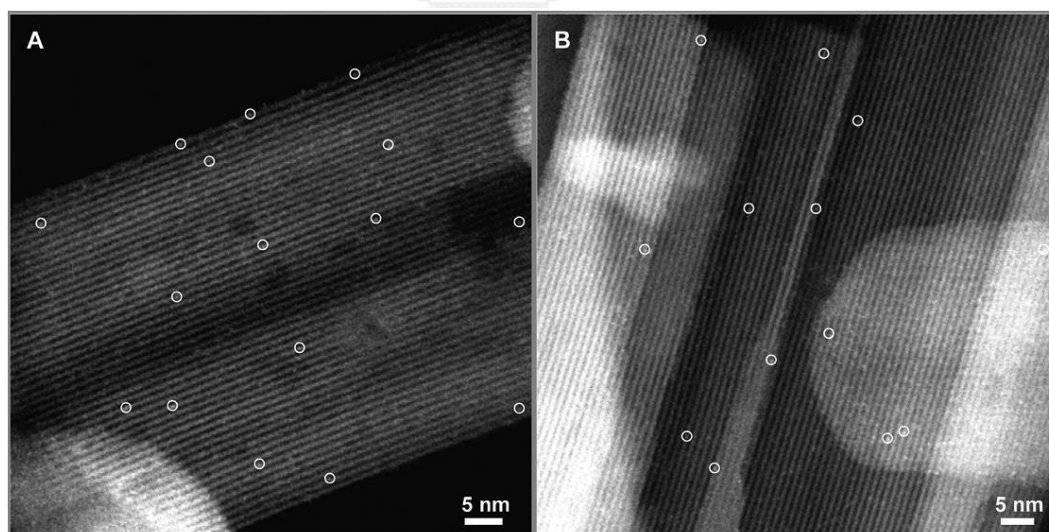
Figure 3.2 HAADF-STEM (Z-contrast) images characterizing the Ir catalyst supported in pore of zeolite HSSZ-53: (A) the initially prepared catalysts and (B) after ethylene hydrogenation [69].

Moreover, the structure of catalytic species supported in the pore was determined by combination of IR and EXAFS spectroscopies as the results are shown in **Table 3.1** and **Figure 3.3**, respectively
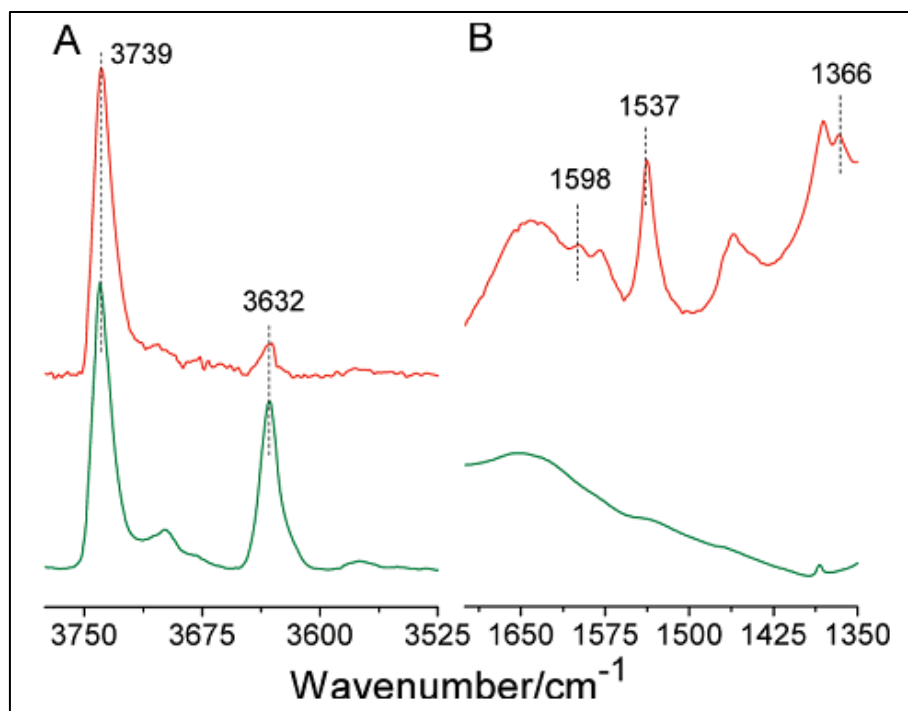
Figure 3.3 IR spectra in the ν_{OH} (A) and 1300-1700 cm^{-1} region (B) characterizing calcined zeolite HSSZ-53 (bottom) and sample after incorporated Ir(C$_2$H$_4$)$_2$(acac) (top) [69].

After the reaction of Ir(C$_2$H$_4$)$_2$(acac) with HSSZ-53, IR spectra in ν_{OH} and 1300-1700 cm^{-1} showed that intensity of 3632 cm^{-1} peak (assigned to acidic hydroxyl groups) significantly decreased while 3739 cm^{-1} peak remained, indicating that the Ir(C$_2$H$_4$)$_2$(acac) preferentially reacted with Al-O$^-$ sites. In the 1300-1700 cm^{-1} region (**Figure 3.3 B**), the spectra revealed the new bands after incorporated the Ir precursor at 1366, 1537, and 1598 cm^{-1}. These bands demonstrated the presence of organic ligands on the samples.

Table 3.1 EXAFS result of the sample formed by the reaction of $Ir(C_2H_4)_2(acac)$ with HSSZ-53 [69].

Coordination shell	N	R (Å)	$10^3 \times \Delta\sigma^2$ ($Å^2$)	ΔE_0 (eV)
Ir-O$_{zeolite}$	2.1	2.10	2.4	-4.1
Ir-C	3.9	2.01	7.1	0.38
Ir-Al	1.0	2.89	9.6	-0.5

Fit details: Range of data used in fitting: $0.5 < R < 3.2$ Å, $3.84 < k < 12.06$ Å^{-1}. Error in EXAFS function: 0.0006. Notation: N, coordination number; R, distance between absorber and backscatterer atoms; $\Delta\sigma^2$, disorder term relative to the reference; ΔE_0, inner potential correction relative to the reference. Error bounds (accuracies) of the structural parameters are estimated to be as follows: N, ±20%; R, ±0.02 Å; $\Delta\sigma^2$, ±20%; and ΔE_0, ±20%.

The structural Ir complexes were further confirmed by EXAFS, reporting in **Table 3.1**. The result indicated that coordination numbers of Ir-O$_{zeolite}$, Ir-C, and Ir-Al shells nearly 2, 4 and 1, respectively. The lack of a detectable Ir-Ir shell indicated the single-atom Ir complexes, consistent with STEM images. From the EXAFS results, the structural model of catalytic Ir complexes is shown in **Figure 3.4**.
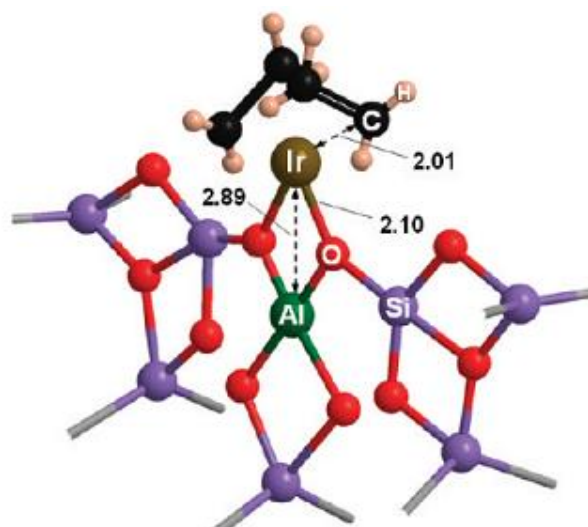
Figure 3.4 Structural model of $Ir(C_2H_4)_2$ complexes bonded at Al site of zeolite HSSZ-53 [69].

3.5 Metal-support interaction

Metal-support interaction is considered as one significant factor for controlling the catalytic activity and stability of dispersed metal in reaction condition [70]. Degree of this interaction is roughly determined by reducibility of dispersed metal (H_2-TPR) as high and low reduction temperature represented the strong and weak metal-support interactions, respectively. With powerful of modern transmission electron microscopy, it allows imaging the structure of materials at atomic level, which can provide the insight information of Pt atoms and clusters bonding to support [8, 71]. This permits fundamental studies of the metal catalytic species and their behavior as a result of elevated temperature treatments. S. A. Bradley et al. [8] demonstrated development of clusters and nanoparticles of Pt on Al_2O_3, SiO_2 and TiO_2 during reduction treatments of highly dispersed states. It was found that these supports stabilized Pt with different extent as mobility of reduced Pt atoms as follows: $TiO_2 < Al_2O_3 < SiO_2$, consistent with metal-support interaction of supports [72] where TiO_2 and SiO_2 had the strongest and weakest metal-support interaction for oxides studied in their work. Moreover, distinct coordinations of Al cations in Al_2O_3

framework also influence metal-support interaction as J. H. Kwak et al. [68] demonstrated that coordinatively unsaturated Al^{3+} centers (pentacoordinate Al^{3+}) on the γ-Al_2O_3 surface are the anchoring sites for strong Pt-support interaction PtO. DFT was also used to fulfill explanation for the experimental results for the possibility of the formation of 2D PtO rafts interacting with Al^{3+}_{penta} surface sites on the γ-Al_2O_3 support surface.
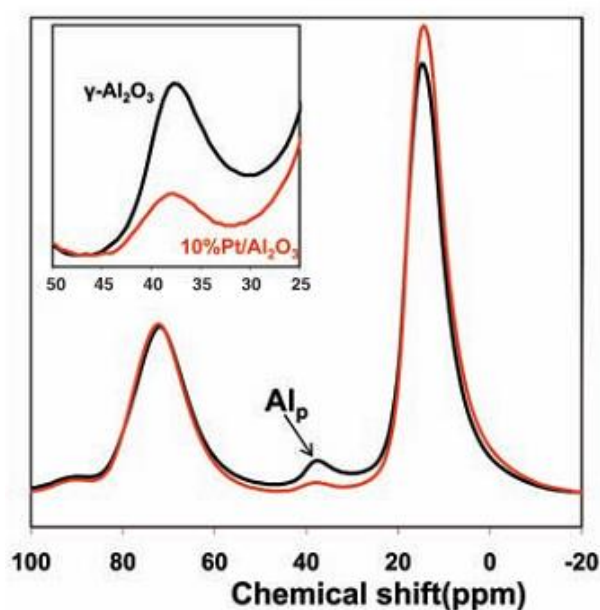
Figure 3.5 The ^{27}Al MAS-NMR spectra of γ-Al_2O_3 (black) and 10 wt %Pt/γ-Al_2O_3 (red) (both samples were calcined at 573 K before NMR measurement) [12].

The results showed a significant decrease in the amount of Al^{3+}_{penta} sites after depositing Pt on to the γ-Al_2O_3 support and calcining the catalyst material at 573 K, as indicated by the large drop in the intensity of the 35-ppm NMR peak (**Figure 3.5**). Coincidently, the intensity of the 13-ppm NMR peak increases with the loading of Pt onto γ-Al_2O_3. These results strongly suggest that Pt atoms bind to the Al^{3+}_{penta} sites on the γ-Al_2O_3 surface through oxygen bridges, thereby coordinatively saturating these sites (Al^{3+}_{penta} to Al^{3+}_{octa}). All of these results suggest that Pt is selectively anchored to the pentacoordinate aluminum ions present on the surface of mildly calcined γ-Al_2O_3. Furthermore, they also confirmed the role of Al^{3+}_{penta} as binding sites for strong metal-

support interaction of Pt/Al_2O_3 catalyst, according to a representative TEM image (**Figure 3.6**) shows the formation of very large 3D Pt particles (10 to 15 nm) on the α-Al_2O_3 support, even after the relatively low-temperature calcination (300 ^oC). The Pt particles can readily migrate on the α-Al_2O_3 even at this relatively low calcination temperature indicated a very weak interaction between PtO and the support owing to the α-Al_2O_3 surface does not possess any Al^{3+}_{penta} sites [73].
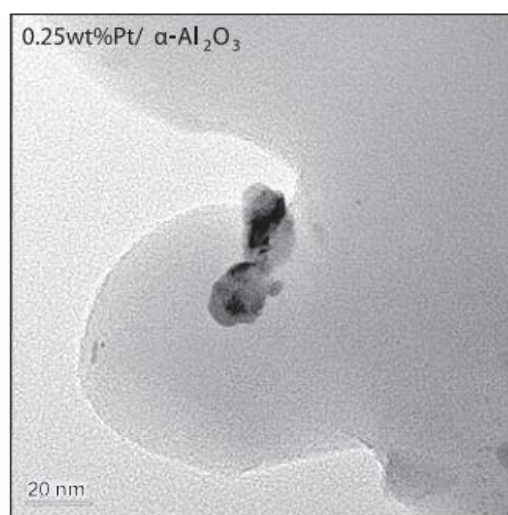
Figure 3.6 TEM image of a 0.25 wt % Pt/α-Al_2O_3 sample obtained after calcination at 573 K [12].

3.6 Oxygen mobility

According to the surface mobility of reactant species plays a crucial role in catalysis, which has been considered as elementary step of reaction mechanisms [26, 74-77]. This led many researchers tends to establish the surface mobility phenomena. For example, H_2 mobility as called "H_2 spillover" has been vastly studied due to H_2 is essential in several reactions including hydrogenation, isomerization, and etc, as discussed in many reviews [74, 75], while O_2 spillover seemed to be the less popular topic. However, O_2 mobility has also been extensively studied by D. Martin and D. Duprez using temperature-programmed isotopic exchange of $^{18}O_2$ with ^{16}O [76]. They reported the rate of oxygen diffusion over several oxides and pointed out the

correlation between oxygen surface mobility and metal-oxygen bonds strength as shown in **Figure 3.7**. Weak bonding strength results in high rate of oxygen diffusion on the surface.
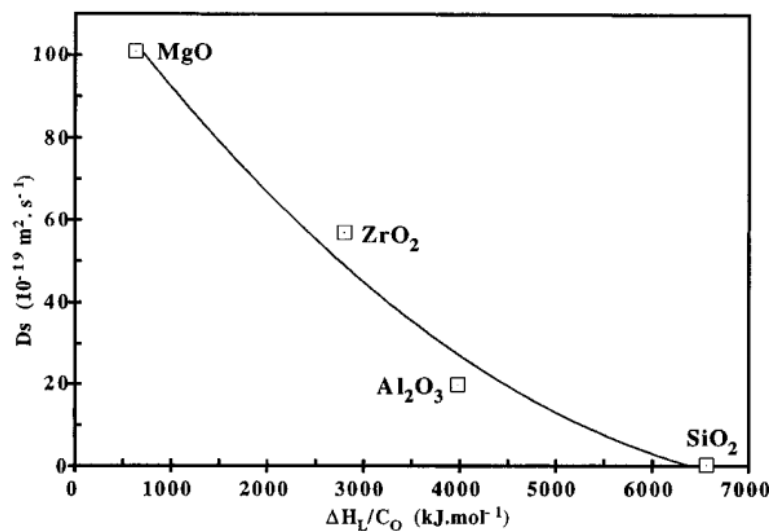
Figure 3.7 Correlation between the oxygen surface mobility and the strength of metal-oxygen bonds [76].

Furthermore, they also revealed that oxygen mobility can be practically link to surface basicity of oxides, as rate of oxygen diffusion increased with amount of surface basicity (**Figure 3.8**). This study was consistent with recent work of V. Dimitrov and T. Komatsu [78]; they established the relation of optical basicity and single bond strength of simple oxides as a function of electronegativity as depicted in **Figure 3.9**. It was found that simple oxide which has low electronegativity causes weak strength of metal-oxygen bonds and high optical basicity.
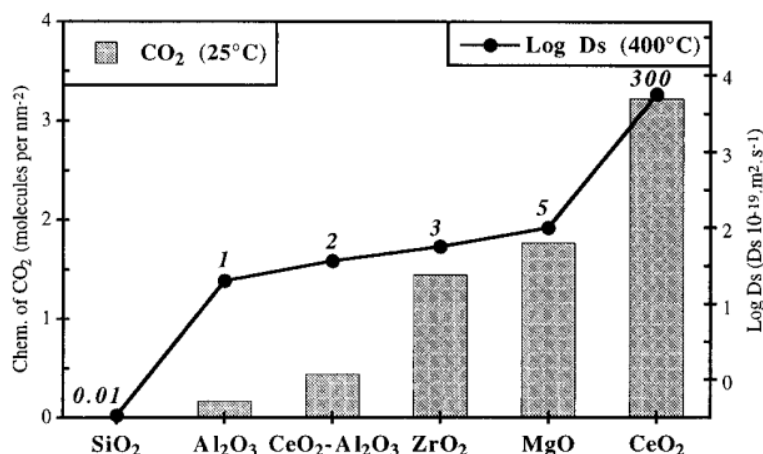
Figure 3.8 Correlation between oxygen surface mobility and oxide surface basicity [76].
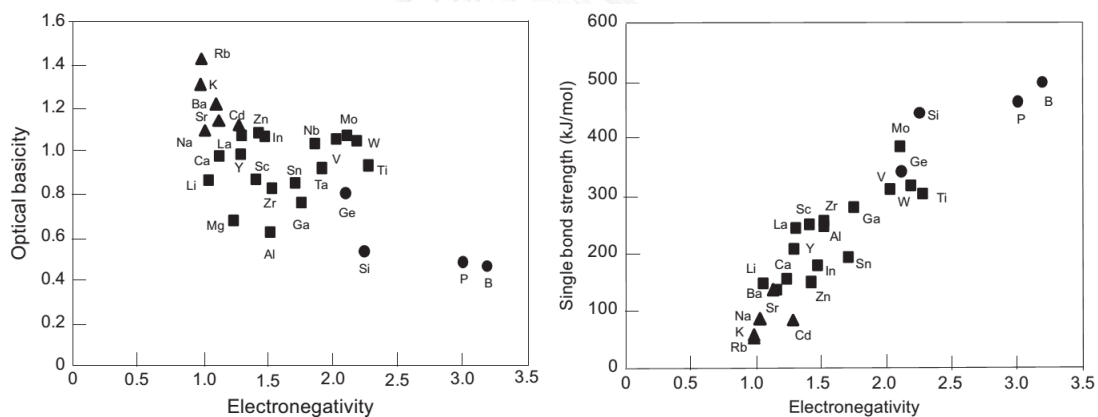
Figure 3.9 Optical basicity (left) and single bond strength (right) of simple oxides as a function of element electronegativity [78].

Oxygen mobility has been reported to influencing combustion temperature of coke generated in propane dehydrogenation on various oxides supported Pt catalysts [26]. It was found that the coke combustion temperatures increased following the reverse order of oxygen mobility of the supports, suggesting that the oxygen transfer over supports was a rate-determining step in the coke combustion process.

3.7 Reaction

3.7.1 CO oxidation

Due to the simplest reaction mechanism and essential in toxic elimination of CO oxidation, it has vastly been investigated by several types of catalysts as the mechanisms have been well established. This leads the CO oxidation become one of the most practical model reactions in catalysis research for both environmental and fundamental understanding [56, 79]. For the purpose of CO removal, the catalysts have been studied and developed in order to effectively oxidize CO to CO_2 at low temperature, which can be conducted by gold and cobalt based catalysts [80, 81]. For fundamental understanding, CO oxidation has typically been utilized as a model reaction to probe the catalytic activity of the well-defined catalysts and their behavior in oxidized model reaction. For example, Qiao et al. [42] reported single-atom platinum catalyst supported on FeO_x as well as Gates et al. [80] demonstrated the gold complexes anchored to La_2O_3 as highly active catalysts for in CO oxidation. Moreover, Alayon et al. [82] demonstrated the role of partially oxidized platinum species in generating a high-activity state in the oxidation of carbon monoxide over Pt/Al_2O_3, Pt/TiO_2 and Pt/SiO_2. The change between the two regimes called "ignition" and "extinction" is identified; there was ignition when going from low to high activity (metallic to partially oxidic Pt), and extinction from high to low activity (partially oxidic to metallic Pt).

3.7.2 Propane Dehydrogenation

Because of the important of propylene as a feedstock employed in the production of polymer, oxygenates and intermediate chemicals such as polypropylene, propylene oxide and propionaldehyde, respectively [28]. The demand of propylene increased over the last years. Moreover, the price of propylene has risen sharply because of a shift from oil-based naphtha to shale-based ethane for producing olefins but shale has a negligible amount of produced propylene, resulting in the

supply of propylene has dropped [29]. This creates the opportunities for propane dehydrogenation that has gained wide attention in recent years. Propane dehydrogenation is a highly endothermic reaction, which requires an elevated temperature to produce propylene commercially. Such a high temperature, it promotes side reactions which reduced yield of propylene and also coke formation which caused the catalyst deactivation [31]. The typical catalysts used in propane dehydrogenation can be separated into Pt-based and Cr-based catalysts. Although Pt/Al_2O_3 based catalyst is catalytically active, great thermal stability and good selectivity to propylene in the given conditions [27] but they still need development in order to increase catalytic performance and stability. The catalyst has been improved mostly by addition of promoters such as Sn, Na, and K [18, 33-35]. Sn is likely the essential requirement because PtSn alloy exhibited excellent characteristics for propane dehydrogenation as a result of neutralization of strong acid sites, reduction of Pt ensemble size and promotion of coke spillover to support [18, 33]. Reduction of ensemble size and neutralization of strong acid sites not only increase selectivity to propylene but also decrease coke formation while spillover of coke to support is also significant to maintaining the catalytic activity. Na and K were also doped in order to poison the strong acid sites of Al_2O_3 support [34, 35], and also stabilizing the highly dispersed state of Pt active centers [10]. Ti and Ce have been of interest for doping into Pt/Al_2O_3 catalyst, having a promotional effect of metal-support interaction for propane dehydrogenation. Titanium was found to facilitate the migration of coke precursors from the metal surface to support caused by the increase of electron density of Pt [31], while Ce-doped catalysts exhibited more active and less coke deposition [17] as a result of enhancement of reducibility and dispersion of Pt nanoparticles.

CHAPTER 4
EXPERIMENTAL

This chapter provides the detail of catalyst preparation, characterization and catalytic test in atmosphere and air exclusion.

4.1 Catalyst preparation

Synthesis and modification methods of γ-Al_2O_3 supports were separated into two parts including incorporating γ-Al_2O_3 support with χ-Al_2O_3 and Si via solvothermal method and coating γ-Al_2O_3 support with Si via dry impregnation. First part, unmodified and modified γ-Al_2O_3 supports were synthesized by a solvothermal method. For the unmodified γ-Al_2O_3, approximately 25 g of aluminum isopropoxide was dissolved in 1-butanol, 100 cm^3 in the test tube and 30 cm^3 in the gap between the test tube and the autoclave wall, respectively. 50:50 v/v of toluene/1-butanol solvents and 1:8 w/w of tetraethylorthosilicate/AIP precursors were used for the modified γ-Al_2O_3 by χ phase and Si dopant, respectively. The autoclave was then purged with N_2 to remove air before heating up to 300 ^{o}C and held for 2 h with a heating rate of 2.5 ^{o}C/min. After spontaneously cooling to room temperature, the as-prepared powder was repeatedly washed with methanol before drying in an oven at 110 ^{o}C overnight. Finally, dried powder was calcined in air at 600 ^{o}C and held for 6 h. Second part, bare γ-Al_2O_3 support was obtained by calcination of aluminium oxide hydroxide (Pural SB grade) in air at 600 ^{o}C for 4h. Then, a series of Si-doped γ-Al_2O_3 supports were prepared via dry impregnation with solution of tetraethylorthosilicate (TEOS) in ethanol yielding different desired SiO_2 loading. Consequently, as-prepared samples were dried at ambient temperature for 2h before in an oven at 110 ^{o}C overnight. The dried powders were calcined in air at 500 ^{o}C for 3h.

The Pt catalysts supported on various Al_2O_3 supports were synthesized by the incipient wetness impregnation method using aqueous hexachloroplatinic acid hexahydrate ($H_2PtCl_6\cdot6H_2O$) as Pt precursor to result in a series of desired wt% of Pt

on a dry basis. Subsequently, impregnated-samples were dried at ambient temperature for 2h before in an oven at 110 ^{o}C overnight, and calcined in air at 500 ^{o}C for 3 h.

The samples were denoted as xSiAl and Pt/xSiAl (x is referred to the wt% of SiO_2 loading) for the supports and the catalysts, respectively. In the case of undoped samples, "Al" and "Pt/Al" were referred to the γ-Al_2O_3 support and the γ-Al_2O_3 supported Pt catalyst, respectively.

4.2 Catalyst characterization

The bulk phase of synthesized-support was examined by using XRD technique (Bruker D8 Advance). The scanning was carried out by using CuK_{α} radiation with Ni filter during the 2θ range of 20–80° with resolution of 0.02. The specific surface area of samples, the pore volume and the average pore diameter were determined by the Brunauer–Emmett–Teller (BET) method on a Micromeritics ASAP 2020 instrument. The measurements were performed with nitrogen as adsorbate at liquid nitrogen temperature following the sample pretreatment at 200 ^{o}C under nitrogen flow for 12 h. The pore size distribution was determined using the BJH method. The elemental distribution on a surface of the catalysts was investigated with SEM-EDX using Link Isis series 300 program SEM (JEOL model JSM-5800LV). The NH_3-TPD, CO_2-TPD, H_2-TPR, CO-pulse chemisorption, and CO-TPD techniques were performed using Chemisorb 2750 (Micromeretics) with different procedures as follows; the acidity and basicity of the supports were examined by NH_3- and CO_2-TPD, respectively. Catalyst powder (50 mg) was treated in He at 510 ^{o}C for 1h prior to cooling down to 30 ^{o}C. After that, 25 ml/min of 15% NH_3/He or 20 ml/min of pure CO_2 was applied through sample for 30 and 20 min, respectively. Then, the sample was purged with He until the baseline was stable. The desorption profile (30-500 ^{o}C) was recorded by a TCD with a heating rate 10 ^{o}C/min.

The concentration of surface Si species of the catalysts were investigated by X-ray Photoelectron Spectra (AMICUS, Kratos) using the Mg K_{α} X-ray source. XPS elemental spectra were acquired with 0.1 eV energy steps at a pass energy of 75 kV. Binding Energy (BE) values were calibrated to the Al 2p peak at 74.4 eV. The raw data were smoothed using the fast Fourier transform method. The reducibility of

catalysts was investigated by H_2-TPR. The 50 mg of catalyst was treated in 25 ml/min of N_2 at 400 ^{o}C for 1 h, then cooled down to 30 ^{o}C. The baseline was stabilized in 10% H_2/Ar for 30 min prior to heating to 800 ^{o}C with a ramp of 10 ^{o}C/min. The H_2 consumption was monitored by a TCD. The Pt active sites and Pt-CO interaction were determined via CO-pulse chemisorption and CO-TPD, respectively. Approximately, 50 mg of catalyst was reduced in H_2 at 500 ^{o}C for 1h. After reduction, the catalyst was flushed with He at 510 ^{o}C for 20 min before cooling down to 30 ^{o}C. Then, portions of CO (20 μl) were pulsed until the catalyst was saturated. Finally, the catalyst was heated to 500 ^{o}C with a heating rate of 10 ^{o}C/min and desorbed-CO profile was recorded by TCD. Active site of the Pt catalysts was calculated with assumption of CO/Pt molar ratio is unity.

The carbon deposition and their oxidation profiles of spent catalysts were investigated by thermogravimetric analyzer (SDT Q600). The spent catalysts were pretreated in N_2 at 100 ^{o}C for 30 min prior to switching to air. Then the sample was heated to 800 ^{o}C with a heating rate of 10 ^{o}C/min.

4.3 Reaction tests

4.3.1 CO oxidation

Approximately 50 mg of catalyst was packed in a quartz reactor (i.d. 5 mm) to test the CO oxidation performance. The catalysts were in-situ reduced in H_2 (50 ml/min) at 500 °C for 1h before purging in He for 20 min and cooling down to 30 °C, subsequently. The feed gas containing 1% CO and 2% O_2 in He with a total flow rate of 50 ml/min was allowed to pass through the reactor. After that, the reactor was heated with a heating rate 2 ^{o}C/min until achieving 100% CO conversion. The CO conversion profile was monitored by an on-line GC-8ATP (Shimadzu) gas chromatograph equiped with a TCD detector and a Molecular Sieve 5A column. The conversion of CO was defined as the number of moles of CO converted per the total number of CO in feed stream. The TOFs of a series of Pt/xSiAl catalysts at 150 ^{o}C

were calculated based on Pt dispersion measured by CO chemisorption and at CO conversion < 15%.

4.3.2 C_3H_8 dehydrogenation

For a series of solvothermal-synthesized catalysts, 50 mg of catalysts were reduced in H_2 at 500 ^{o}C for 1 h before switching to He and holding for 10 min. After that, the reactor was cooled to reaction temperature at 450 ^{o}C. The feed composes C_3H_8, H_2, and He (3:1:6) with a total flow rate of 50 ml/min was fed to the reactor. For a series of Si-doped γ-Al_2O_3, propane dehydrogenation test was performed with a similar manner except 100 mg of catalyst and 600 ^{o}C of reaction temperature were used instead. The products were analyzed by a GC-14B (Shimadzu) gas chromatograph equipped with a FID detector and a VZ-10 column.

The conversion of propane was determined from eq 1, and the selectivity to propylene was determined from eq 2:

$$C_3H_8 \text{ conversion } (\%) = \frac{C_3H_{8in} - C_3H_{8out}}{C_3H_{8in}} \times 100\% \qquad (1)$$

$$C_3H_6 \text{ selectivity } (\%) = \frac{C_3H_{6out}}{C_3H_{8in} - C_3H_{8out}} \times 100\% \qquad (2)$$

where C_3H_{8in}, C_3H_{8out} are the propane content in feed and exit gases and C_3H_{6out} is propylene content in exit gas.

The deactivation constant (k_d) was used to compare the catalyst stability, calculating from eq 3 [83]:

$$k_d \ (h^{-1}) = \frac{\ln\left(\frac{1-x_{180}}{x_{180}}\right) - \ln\left(\frac{1-x_5}{x_5}\right)}{t} \qquad (3)$$

where X_5 and X_{180} represent the conversions at the 5 min and 180 min of time on stream (t), respectively. High number of k_d indicated rapid deactivation.

4.4 Moisture and air exclusion experiments

4.4.1 Sample Synthesis and Handling

KLTL zeolite-supported platinum amine complexes were prepared and handled with standard Schlenk line, argon-filled glove box and glove bag techniques to exclude moisture and air. He (Airgas, 99.999%), H_2 (Praxair, 99.999%), O_2 (Airgas 10% by volume balanced in He) and CO (Airgas, 10% by volume balanced in He) were purified by passage through traps containing supported copper and zeolite 5A to remove traces of O_2 and moisture (MBraun, with H_2O concentrations <0.5 ppm and O_2 concentrations <1 ppm), respectively.

The KLTL zeolite (with one-dimensional channel system and 12-membered ring pores) was provided by UOP; it was calcined in flowing dry 10% O_2 in He as the temperature was increased at 3 ^{o}C/min from room temperature to 300 ^{o}C and held at that value for 4 h followed by evacuation for 12 h. A 1.0 wt% Pt zeolite sample was prepared by ion exchange with $Pt(NH_3)_4(NO_3)_2$ and calcined KLTL zeolite in deoxygenated deionized water, with stirring at room temperature for 24 h. The water was subsequently removed by evacuation for 24 h at room temperature.

The as-prepared sample, $Pt(NH_3)_4^{2+}$/KLTL zeolite, was oxidized in the presence of flowing 10% O_2 in He in a once-through glass tubular flow reactor. The powder sample (0.50 g) in the glove box (MBraun, with H_2O concentrations <0.5 ppm and O_2 concentrations <1 ppm) was loaded into a reactor with a frit. The reactor was sealed on both ends with O-ring compression fittings. The reaction took place in an electrically heated tube furnace. The temperature in the reactor was measured with a K-type thermocouple. A stream of 10% O_2 in He flowed through the reactor at a rate of 50 mL (NTP)/min as the temperature was ramped to 633 K at a rate of 3 ^{o}C/min. The temperature of the reactor was held at 360 ^{o}C for 4 h, and then it was cooled to room temperature with continuous O_2 flow. The effluent gases from the reactor were analyzed with an online mass spectrometer (Pfeiffer Vacuum Omnistar QME 200). All experiments were conducted with no exposure of the sample to air.

4.4.2 IR spectroscopy

IR spectra of the supported species were recorded with a Bruker IFS 66v/S spectrometer with a spectral resolution of 2 cm^{-1}. Approximately 40 mg of each solid sample in a glove box was pressed into a thin wafer and loaded into a cell that served

as a flow reactor (In-situ Research Institute, South Bend, IN, USA). The flow reactor/cell was sealed and connected to a flow system that allowed recording of transmission spectra of the solid sample while the reactant gases flowed through the cell and around and through the sample at a set temperature. Each reported spectrum is the average of 64 scans.

4.4.3 EXAFS spectroscopy

X-ray absorption spectra were recorded at X-ray beamline 4-1 at the Stanford Synchrotron Radiation Lightsource (SSRL). The storage ring current was 300 mA. A Si (220) monochromator was detuned to 75–80% of the maximum intensity at the Pt L_{III} edge to reduce the interference of higher harmonics in the X-ray beam. In an argon-filled glove box (MBraun, with H_2O concentrations <0.5 ppm and O_2 concentrations <1 ppm) at SSRL, each powder sample was pressed into a wafer, mounted in a cell [84], and maintained under vacuum (10^{-5} kPa) at liquid-nitrogen temperature during the data collection. The mass of each sample (approximately 0.25 g) was chosen to give an absorbance of 2.5 calculated at 50 eV above the absorption edge (11564 eV). Spectra were collected in transmission mode by use of ion chambers mounted on each end of the sample cell. For L_{III} calibration purposes, measurement of the absorption of a platinum foil, placed downbeam of the sample, was carried out simultaneously.

4.4.4 EXAFS data analysis

Analysis of the EXAFS data was carried out with ATHENA of the software package IFEFFIT8 and with the software XDAP developed by Vaarkamp et al. [85] Each spectrum subjected to analysis was the average of 2-4 consecutively recorded spectra. ATHENA was used for edge calibration, deglitching, and data normalization. XDAP was used for background removal, normalization, and conversion of the data into an EXAFS (χ) file. The data were normalized by dividing the absorption intensity by the height of the absorption edge. A "difference file" technique was applied with

XDAP for determination of optimized fit parameters [52]. Each spectrum was processed by fitting a second-order polynomial to the data in the pre-edge region and subtracting this from the entire spectrum. The functional that was minimized and the function used to model the data are presented elsewhere [86]. The background was subtracted by using cubic spline routines. Reference backscattering phase shifts were calculated from crystallographic data determined with the software FEFF7 [87]. The number of parameters used in the fitting was always less than the statistically justified number, computed with the Nyquist theorem: $n = (2\Delta k\Delta r/\pi) + 2$ (where Δk and Δr, respectively, are the k (wave vector) and r (distance) ranges used in the fitting) [52]. In the development of best-fit models of each of the EXAFS data sets, various combinations of plausible absorber–backscatterer contributions were fitted initially, which led to a list of candidate models narrowed on the basis of the goodness of fit and the overall fit in both k space and R space. Then, the difference-file technique [52] was applied to the candidate models, whereby the calculated EXAFS contribution from each individual shell was compared with the calculated data in R space (calculated by subtracting all the other contributions from the total experimental data). This iterative fitting was continued in R space for both the overall data sets and the individual contributions with the Fourier-transformed EXAFS (χ) data until the best-fit model was obtained—which is the one providing optimum agreement between the calculated k^0-, k^1-, k^2-, and k^3-weighted EXAFS data and the model. Other models considered for the data fitting are presented below in **Table F.1** and **F.2**.

The fit quality of each candidate model was evaluated by the value of $(\Delta\chi)^2$, the goodness of fit, as defined by the International XAFS Society. This parameter takes into account the number of fitted parameters and statistically independent data points, thus allowing comparisons of candidate models containing various numbers of contributions and fit ranges. By using $(\Delta\chi)^2$ we were able to determine whether the addition of each new contribution to a candidate model improved the fit. To calculate the $(\Delta\chi)^2$ parameter for each of the fits, an estimate of the error (or noise) in the EXAFS data was calculated by Fourier filtering the data up to an R value of 5 Å.

4.4.5 CO oxidation catalysis

Data characterizing catalytic activity of the samples for CO oxidation were obtained with a conventional laboratory once-through glass tubular plug-flow reactor that was held at near isothermal conditions. The catalyst powder (25 mg), mixed with 5 g of inert, nonporous α-Al_2O_3 powder, was loaded into the reactor in an argon-filled glove box without exposure to air. In the catalytic reaction experiments, the feed was 1% CO and 5% O_2 in He with a total flow rate of 25 mL/min; the pressure was atmospheric. The temperature was $150 \pm 1\ ^oC$ measured with a K-type thermocouple. Effluent gas products were analyzed periodically by online gas chromatography with an HP-5890 gas chromatograph equipped with a 50 m $\times$ 0.53 mm Porapak Q column and a thermal conductivity detector.

4.4.6 Sample handling for electron microscopy

Samples for STEM were prepared by dipping a 200-mesh lacey-carbon-coated copper grid (Ted-Pella) into as-prepared or oxidized catalyst powders in the glove box. Sealed samples were transported from the glove box (MBraun, with H_2O concentrations <0.5 ppm and O_2 concentrations <1 ppm) to the microscope, where the sample was mounted onto a sample holder in an argon-filled glove bag, which was purged five times with argon before use. The sample holder was transferred from the glove bag to the microscope, with the air exposure lasting < 3 s. The samples were imaged with high-angle annular dark-field (HAADF) STEM. The microscope was an aberration-corrected FEI Titan 80/300 operating at 300KeV; the convergence angle was 35.6 mrad, and the HAADF collection inner angle was ~75 mrad. To minimize artifacts in the images caused by beam damage, the microscope was aligned for one region of the sample, and then the beam was shifted to a neighboring region for quick image acquisition: 4 μs for a 1024 $\times$ 1024 pixel size. This method minimized the exposure of the imaged area to the electron beam.

CHAPTER 5
RESULTS AND DISCUSSION

This chapter provides the results and discussion in three main sections as follows: **Section 5.1** Comparison of the effects of χ phase- and Si- modified γ-Al$_2$O$_3$ supported Pt catalysts in CO oxidation, **Section 5.2** Promotional effects of Si-doped γ-Al$_2$O$_3$ supported Pt catalysts for CO oxidation and propane dehydrogenation and **Section 5.3** Microscopic and spectroscopic determination of the locations of the single-site Pt in KLTL zeolite as a CO oxidation catalyst.

5.1 Comparison of the effects of χ phase- and Si- modified γ-Al$_2$O$_3$ supported Pt catalysts in CO oxidation

5.1.1 Effect of support modification on the physical and chemical properties of Pt/Al$_2$O$_3$ catalysts

XRD patterns from 2θ = 20° to 80° of the Al$_2$O$_3$ supports are shown in **Figure 5.1**. The unmodified γ-Al$_2$O$_3$ showed the expected main peaks at 38°, 46° and 67° corresponding to the (311), (400) and (440) planes, respectively [88]. The χ phase-modified support showed additional peak at 43° due to the characteristic peak of χ-Al$_2$O$_3$ [89]. Moreover, the modification of γ-Al$_2$O$_3$ by χ-phase significantly increased the diffraction intensity, demonstrating higher crystallinity and an increased average crystallite size of Al$_2$O$_3$ (Table 5.1). In contrast, the Si-modified support exhibited only the peaks corresponding to γ-Al$_2$O$_3$ but the diffraction intensities were lower due probably to the dilution effect [20].
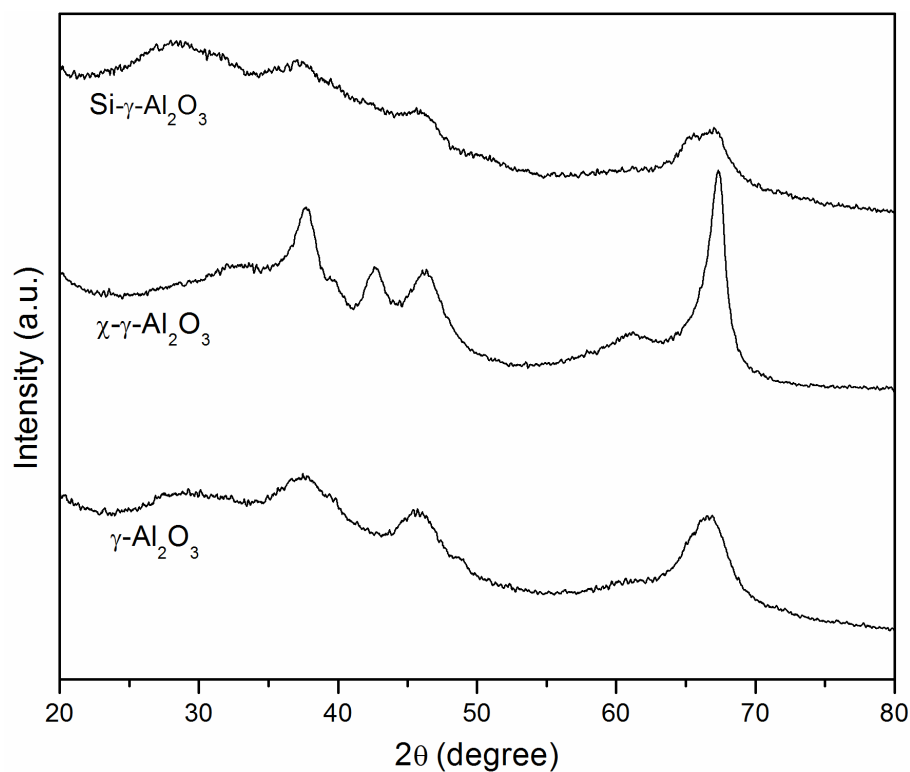
Figure 5.1 XRD patterns of various Al_2O_3 bare supports.

The N_2 physisorption results and pore size distribution of the supports are displayed in **Table 5.1** and **Figure 5.2**, respectively. The BET surface area, pore volume, and average pore diameter of χ phase-modified support were lower compared to the unmodified γ-Al_2O_3 support, in agreement with our previous works [13, 89]. The results were consistent with a slight shift of pore size distribution to smaller pore size due to higher density of spherical χ-Al_2O_3 particles [14]. In contrast, the BET surface area, pore volume, and average pore diameter of the Si-modified ones were slightly higher. The presence of Si in Al_2O_3 framework may extend the pore size distribution to larger pore size [38]. The Si content in the Si-modified Al_2O_3 sample in term of Si/Al ratio was determined by 0.9 as reported in Table 5.1.

Table 5.1 Physicochemical properties and TOFs of 1 wt% Pt supported on Al_2O_3 supports.

Sample	BET surface area $(m^2/g)^a$	Pore volume $(cm^3/g)^a$	Average Pore Diameter $(nm)^a$	Al_2O_3 crystallite size $(nm)^b$	Si/Al molar ratio^c	CO_2 desorption (μmole/g)	TOF $\times 10^2$ $(s^{-1})^d$
1Pt/γ-Al$_2$O$_3$	210 (215)	0.48 (0.64)	6.34 (8.77)	2.5	0.01	0.6	3.0
1Pt/χ-γ-Al$_2$O$_3$	170 (176)	0.43 (0.52)	6.68 (7.75)	5.8	0.01	0.47	2.0
1Pt/Si-γ-Al$_2$O$_3$	209 (229)	0.82 (0.94)	10.78 (12.03)	2.3	0.09	0.26	0.6

[a] The number in parenthesis indicate the surface area, pore volume and average pore diameter of the bare supports.

[b] Al_2O_3 crystallite size calculated from the XRD result based on the Scherrer equation

[c] Si/Al ratio calculated from the SEM-EDX result

[d] TOF at 150 °C was calculated at CO conversion <20%
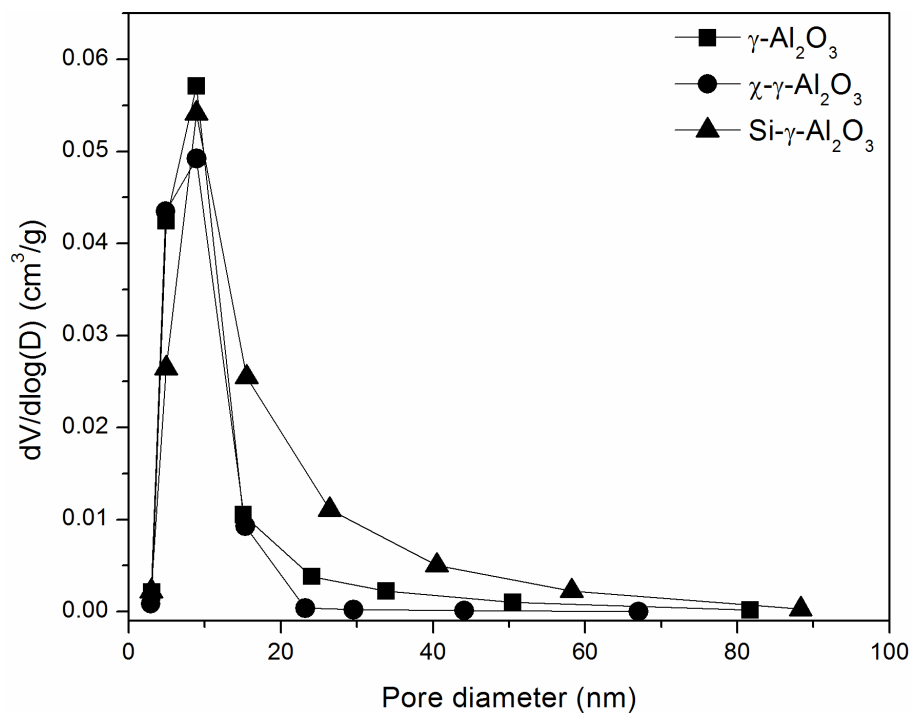
Figure 5.2 Pore size distribution of Al_2O_3 supports.

The CO_2-TPD profiles of 1 wt% supported Pt catalysts are shown in **Figure 5.3**. It is demonstrated that support modification did not significantly alter the base strength of catalysts. However, the amount of basic sites of χ phase-modified support was slightly lower than that of the unmodified γ-Al_2O_3 whereas the modified γ-Al_2O_3 by Si incorporation resulted in substantially decreased of the basic sites [90].
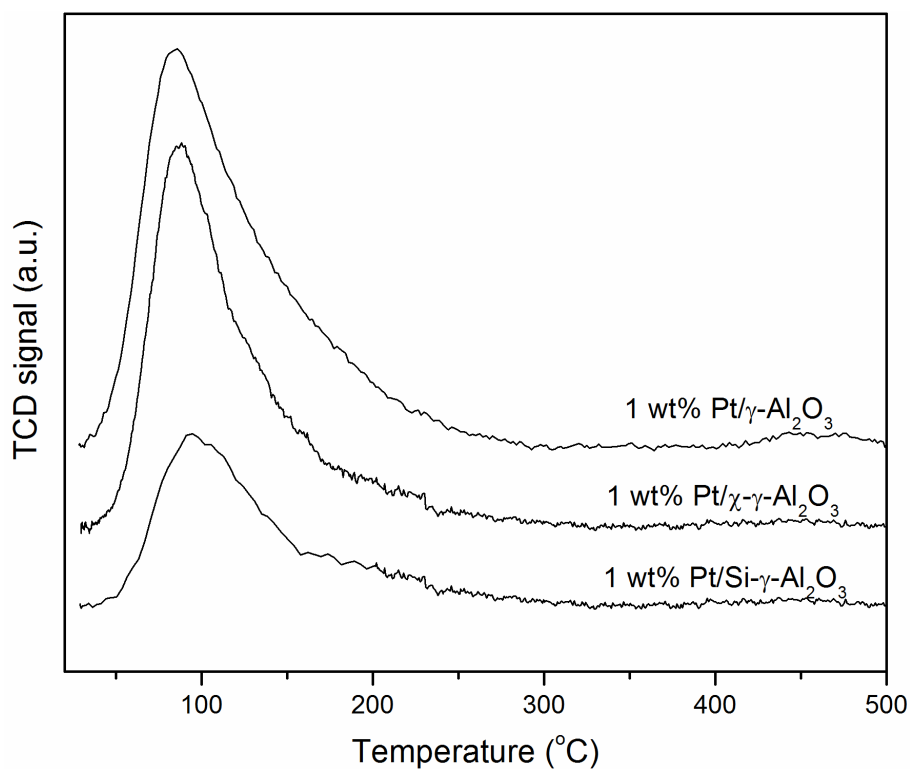
Figure 5.3 CO_2-TPD patterns of Al_2O_3 supported 1 wt% Pt catalysts.

After Pt loading, the XRD peaks corresponding to Pt metal were not detected due probably to the very small particles size and that Pt was well dispersed especially for 0.3-1 wt. % loading range. Comparison of the XRD and N_2-physisorption results between the bare Al_2O_3 supports and the supported Pt catalysts indicates that impregnation, drying, and calcination steps did not essentially affect the surface area and crystalline structure of the Al_2O_3.

5.1.2 Effect of support modification on the amount of Pt active sites
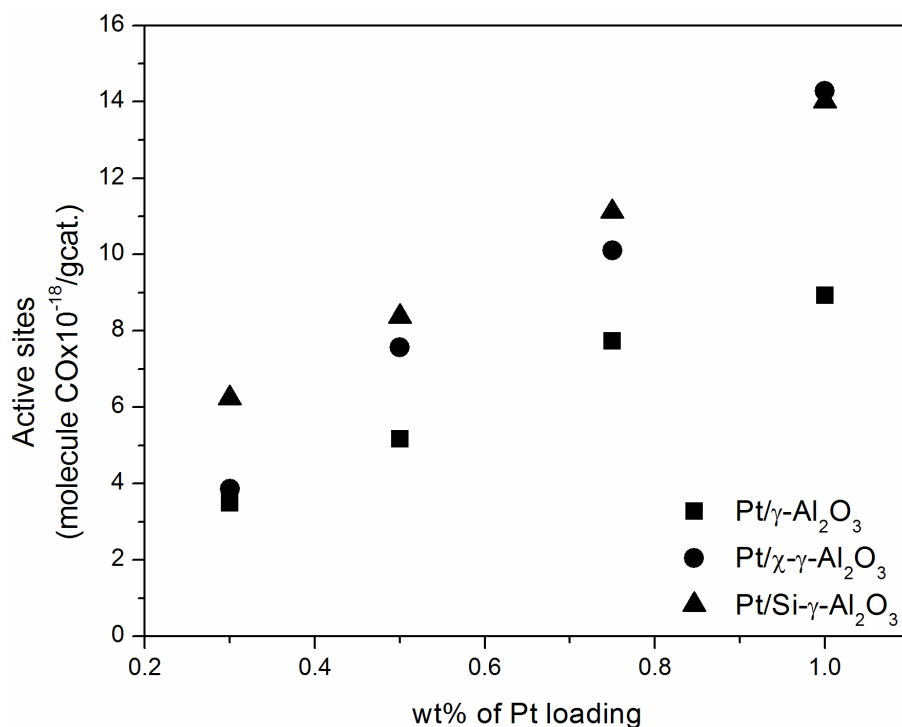
Figure 5.4 The relationship of Pt active sites and wt% of Pt loadings.

The Pt/Al$_2$O$_3$ catalysts with various loadings ranging from 0.3, 0.5, 0.75 and 1 wt% were dispersed on the modified γ-Al$_2$O$_3$ supports and compared to the unmodified γ-Al$_2$O$_3$ support. The relationship between the Pt active sites measured by CO pulse chemisorption and wt% loading of all the catalysts are presented in **Figure 5.4**. Different responses of Pt active sites with increasing of wt% loading can be observed. It can be seen that introduction of χ-Al$_2$O$_3$ and Si into γ-Al$_2$O$_3$ supports significantly enhanced the number of Pt active sites, except at 0.3 wt% Pt loading where the addition of χ-Al$_2$O$_3$ slightly increased the Pt active sites from 3.49 to 3.86 molecules CO ×10^{-18}/gcat. Also, the modified γ-Al$_2$O$_3$ support revealed greater response to Pt loading compared to the unmodified γ-Al$_2$O$_3$ support. The dispersion of Pt metal on various supports was influenced by many factors such as surface area, thermal stability, and metal-support interaction. Sintering of Pt metal may occur during oxidation-reduction treatment due to their differences of thermal stability

under O_2 and H_2 environment [91, 92]. Previous study showed that Co catalysts supported on spherical χ-particle Al_2O_3 were more resistant to agglomeration than on wrinkled sheet γ-Al_2O_3 particles during calcination and CO hydrogenation [14, 67]. Moreover, Si incorporated in Al_2O_3 also improved the thermal stability and retarded Pt sintering [93].

5.1.3 Catalytic performance in CO oxidation
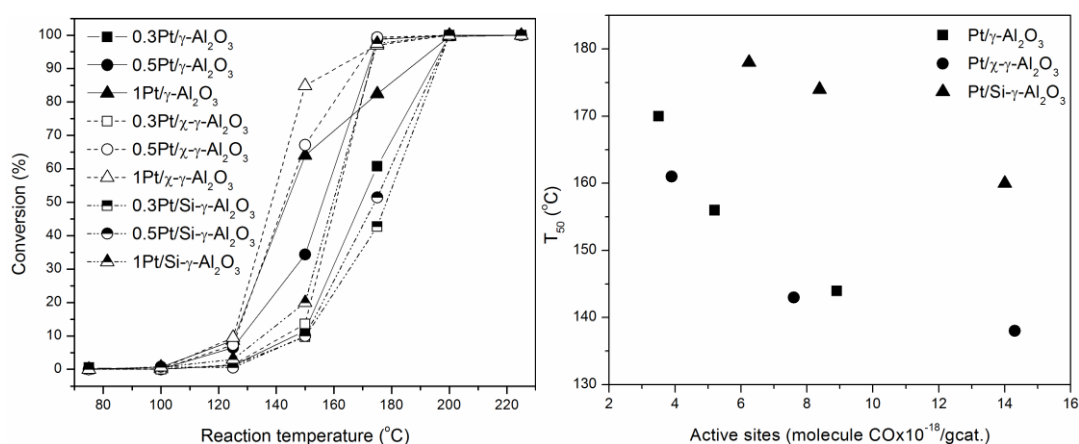
Figure 5.5 The CO oxidation results: (left) CO conversion profiles of the catalysts, (right) temperature at 50% conversion of CO oxidation against active sites (reaction condition: CO 1; O_2 2; He 97 ml/min).

The results of reaction tests in CO oxidation are shown in **Figure 5.5** (left). The catalytic activity in CO oxidation increased as the Pt loading increased. The light-off temperature of CO conversion (T_{50}) was typically used as representative of CO oxidation activity. Correlations between T_{50} and the number of Pt active sites of all the catalysts are presented in **Figure 5.5** (right). For all the catalysts, T_{50} decreased with increasing number of active sites [54]. For the Si-modified supported Pt catalysts, T_{50} decreased from 178 to 160 ^{o}C with linearly increasing of active sites from 6.24 to 14 molecules $CO\times10^{-18}$/gcat. For pure Al_2O_3 supported catalysts (χ phase-modified and unmodified γ-Al_2O_3), T_{50} sharply decreased from 168 to 143 ^{o}C and slowly decreased from 143 to 138 ^{o}C with increasing of active sites from 6.24 to

7.6 and from 7.6 to 14 molecules $CO \times 10^{-18}$/gcat., respectively. Such relationship clearly confirmed the structure insensitive characteristic of CO oxidation reaction. It should be noted that increasing of Pt active sites can lower T_{50} until it reaches the temperature that CO molecules cover the Pt active surface without desorption [22]. This regime could be observed for the pure Al_2O_3 support. Consequently, no Pt active surface was available for activating the O_2 from gas phase to $O_{surface}$ according to the Langmuir-Hinshelwood model [94].

5.1.4 Effect of support modification on the oxygen mobility

Apparently, the modified γ-Al_2O_3 via Si incorporation significantly reduced the CO oxidation activity even though the number of Pt active sites increased. The lower CO oxidation activity of Si-modified supported Pt catalysts compared to the bare Al_2O_3 supported ones could be explained by the effect of oxygen mobility of different metal oxide supports. According to Vu et al. [26], combustion temperature of coke covered on different supports depended on the different oxygen mobility property. The higher oxygen mobility resulted in lower temperature of coke combustion. The mobility of surface oxygen has also been investigated extensively by Martin and Duprez [25]. The rates of oxygen isotopic exchange at surface of bare- and supported-Rh catalysts of various metal oxides including Al_2O_3 and SiO_2 were determined. In particular, they demonstrated that the rate of oxygen surface diffusion was practically linked to the amount of basic sites. Consistent with our CO_2-TPD results, the Si-modified γ-Al_2O_3 had much lower amount of basic sites and the catalysts exhibited lower activity in CO oxidation. Nevertheless, in the case of χ-Al_2O_3 incorporation, the CO oxidation activity was improved for the catalysts containing similar amount of Pt loading due to higher Pt dispersion although the amount of basic sites was slightly lower. In other words, their conformity in the performance and active sites plots clearly indicated that modified γ-Al_2O_3 by χ-Al_2O_3 did not essentially affect the oxygen mobility properties (placed in the same curve with the unmodified γ-Al_2O_3).

Compared Pt loading at 1 wt% Pt on both modified γ-Al_2O_3 supports, the active sites of these supports were very close while the amount of basic sites were

much different. Therefore, it is suggested that the oxygen mobility could be the predominant influence on the CO oxidation performance of the modified γ-Al_2O_3 supported Pt catalysts. The distinction of T_{50} as well as the calculated TOFs (Table 5.1) were in good relation with the amounts of desorbed-CO_2, pointing out that mobile oxygen on the support importantly participated in the CO oxidation elementary steps. This implies that CO oxidation mechanism not only includes the reaction of $O_{surface}$ and $CO_{surface}$ species activated and reacted by the same Pt cluster but also the reaction of $O_{surface}$ activated by one Pt cluster before transferring on the support to react with $CO_{surface}$ activated by the nearby Pt clusters and form CO_2 before desorption as the product.
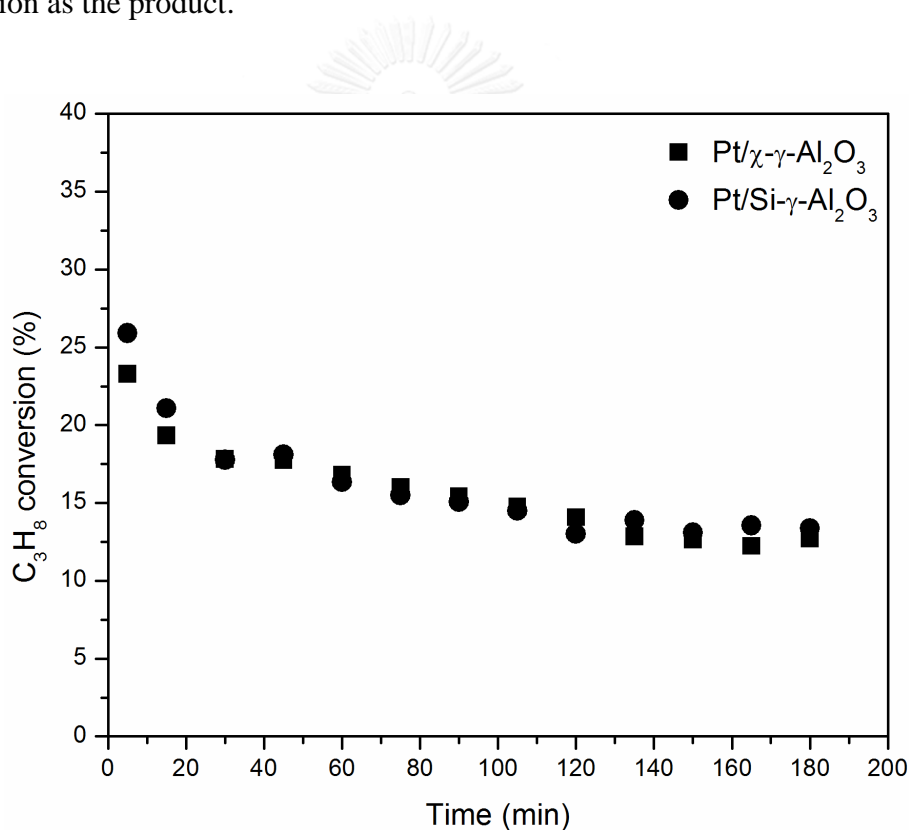
Figure 5.6 The catalytic activity of supported 1 wt% Pt catalysts in C_3H_8 dehydrogenation (reaction condition: C_3H_8 15; H_2 5; He 30 ml/min at 450 $^{\circ}$C).

To strengthen the effect of oxygen mobility, χ phase- and Si-modified γ-Al_2O_3 supported 1 wt% Pt catalysts were tested in propane dehydrogenation as a non-oxidative structure-insensitive probe reaction [27] owing to Pt active sites of these

catalysts are nearly similar. The catalytic activity of the catalysts is shown in **Figure 5.6**. Although, propane conversion of Si-modified γ-Al_2O_3 supported 1 wt% Pt catalysts was slightly higher than the other one. But the result strongly indicated that initial dehydrogenation activity is still in a good agreement with Pt active sites unlikely to the substantial distinct in CO oxidation. This comparison between the catalytic behavior in CO oxidation and C_3H_8 dehydrogenation could confirm and highlight the effect of oxygen mobility in oxidative reaction of supported Pt catalysts.

5.2 Promotional effects of Si-doped γ-Al$_2$O$_3$ supported Pt catalysts for CO oxidation and propane dehydrogenation

5.2.1 The physical properties of xSiAl supports

The SiO$_2$ content on each sample was probed by EDX from 4 individual SEM images as reported in **Table 5.2**. The results show that the undoped γ-Al$_2$O$_3$ contained approximately 0.6 wt% SiO$_2$ before impregnation with TEOS. For the series of SiO$_2$-doped γ-Al$_2$O$_3$ samples, the SiO$_2$ contents nearly corresponded to the sum of SiO$_2$ addition and SiO$_2$ in the undoped γ-Al$_2$O$_3$.
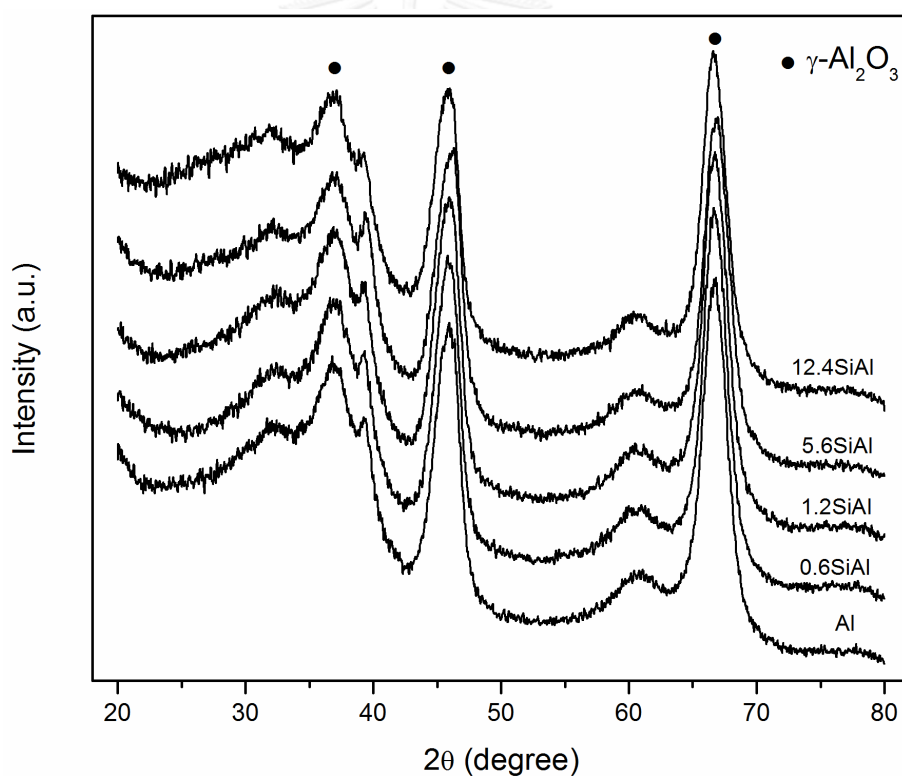
Figure 5.7 XRD patterns of a series of xSiAl supports.

The XRD patterns from $2\theta = 20^\circ$ to 80° of the bare supports are shown in **Figure 5.7**. The undoped γ-Al$_2$O$_3$ revealed the expected peaks at 38°, 46° and 67°, indicating the γ-phase Al$_2$O$_3$ [95]. The XRD results show that addition of 0.6 - 12.4

wt% SiO_2 did not change the crystallinity of the γ-Al_2O_3 support. However, the main peak at 67° slightly decreased for 5.6 and 12.4SiAl samples. This may be due to dilution effect when increasing amount of amorphous silica [20]. The N_2 physisorption results and pore size distribution are shown in **Table 5.2** and **Figure 5.8**, respectively. As expected, the BET surface area, pore volume, and average pore diameter were slightly decreased with increasing of SiO_2 content. For the 5.6 wt% SiO_2 addition, the BET surface area, pore volume, and average pore diameter decreased from 203 to 193 m^2/g, 0.53 to 0.48 cm^3/g, and 6.6 to 6.1 nm, respectively. They were further decreased down to 169 m^2/g, 0.41 cm^3/g, and 5.8 nm with increasing of SiO_2 content up to 12.4 wt%. A shift of pore size distribution towards smaller pore and the decline of the N_2 physisorption were due probably to the accumulation of SiO_2 and pore blockages after impregnation with TEOS solution [16], especially considerable influence at high SiO_2 loading.
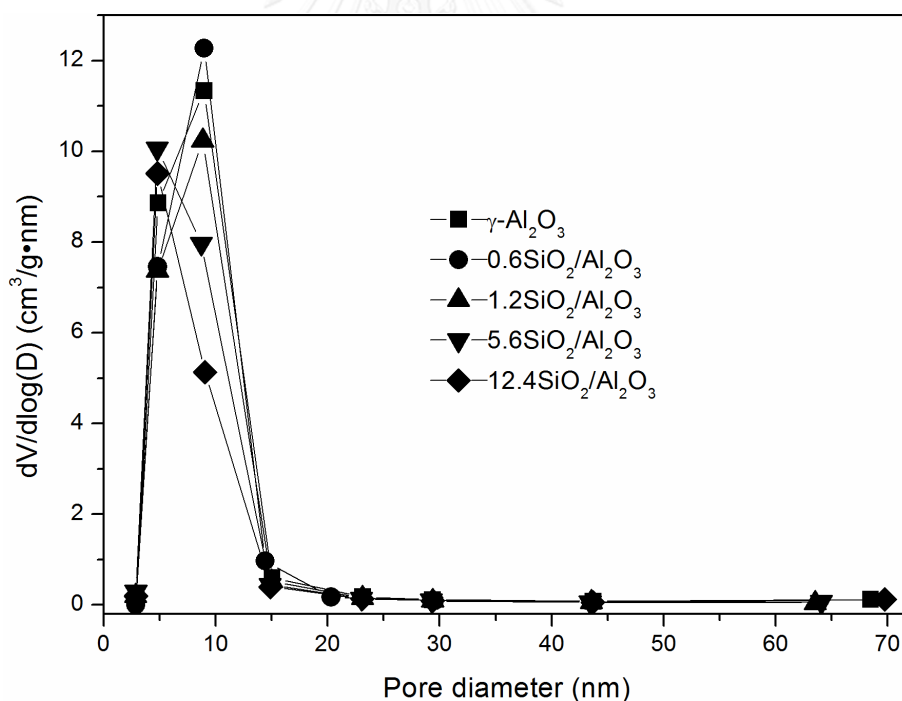
Figure 5.8 Pore size distribution of xSiAl supports.

Table 5.2 Physical properties of xSiAl supports.

Sample	SiO$_2$ loading (wt %)	SiO$_2$ content (wt %)[a]	Si/Al molar ratio[b]	BET surface area (m^2/g)	Pore volume (cm^3/g)	Average Pore diameter (nm)
Al	0	0.6	n.d.	203	0.53	6.6
0.6SiAl	0.6	1.1	n.d.	187	0.49	6.7
1.2SiAl	1.2	1.7	n.d.	183	0.49	6.6
5.6SiAl	5.6	6.9	0.091	193	0.48	6.1
12.4Si/Al	12.4	11.5	0.24	169	0.41	5.8

[a] SiO$_2$ wt% composition calculated from the SEM-EDX result

[b] Si/Al molar ratio of catalysts calculated from the XPS results

n. d. refers to not detect

5.2.2 The acid-base characteristics of xSiAl supports.
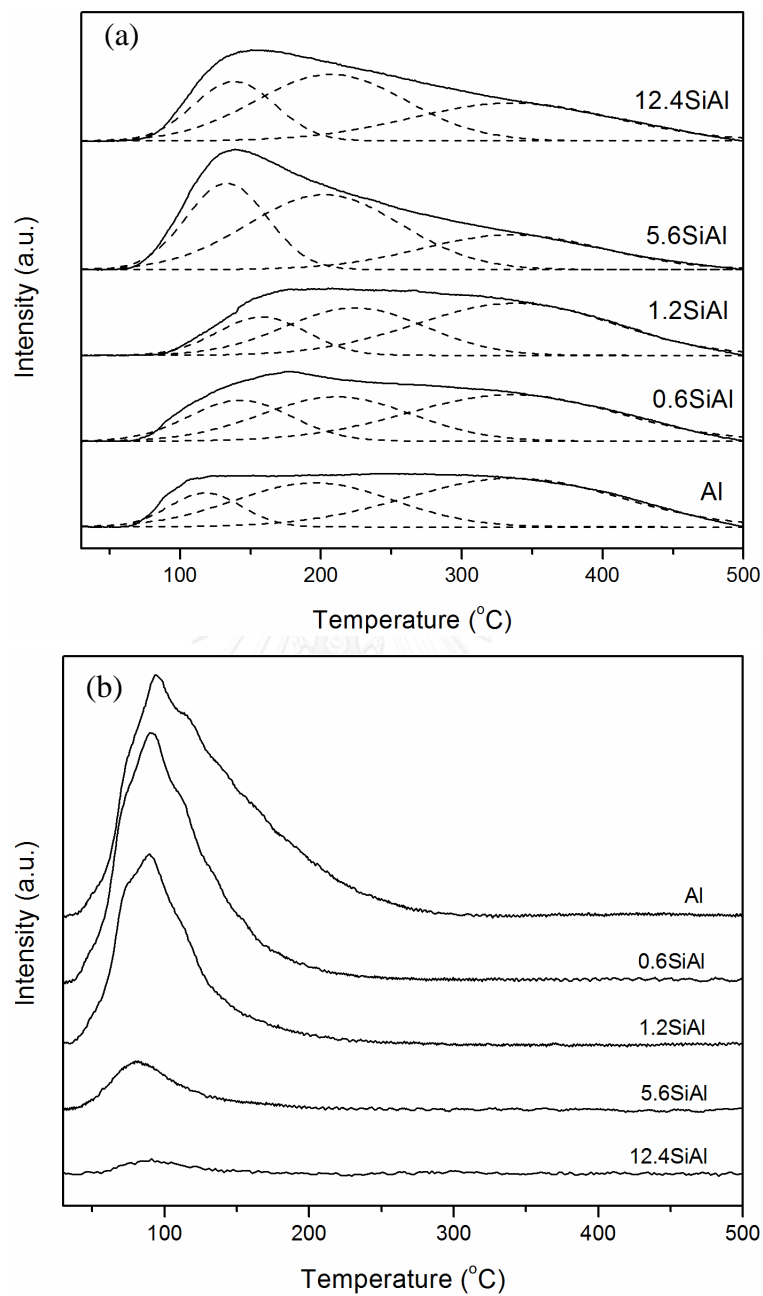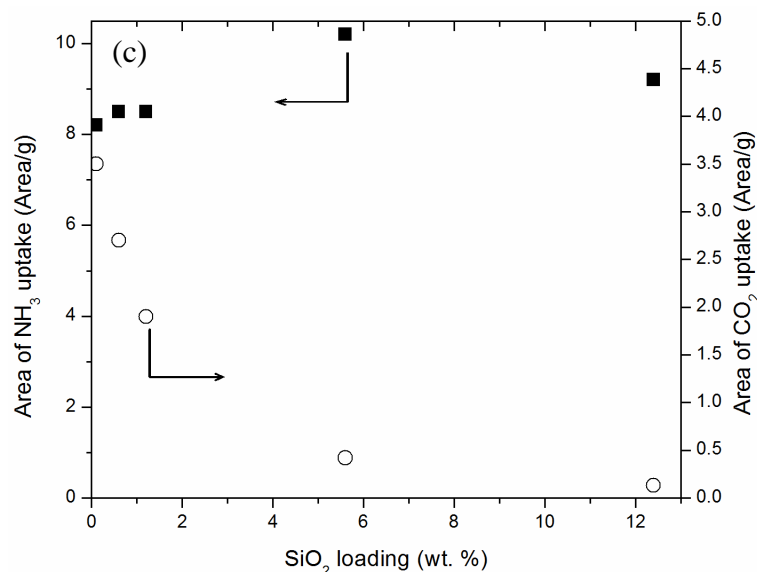
Figure 5.9 NH$_3$-TPD profiles (a), CO$_2$-TPD profiles (b), and NH$_3$- and CO$_2$-uptake (c) as a function of SiO$_2$ loading of xSiAl supports.

The NH$_3$-TPD and CO$_2$-TPD profiles for a series of xSiAl supports are displayed in **Figure 5.9 (a)** and **(b).** The area of those TPD profiles represented the NH$_3$ and CO$_2$ uptake as a function of SiO$_2$ loading is presented in **Figure 5.9 (c)**. The results showed that NH$_3$ uptake increased to a minimal extent as SiO$_2$ loading increased, whereas CO$_2$ uptake decreased dramatically with insignificant alternate of the basicity strength. It is likely that the Brønsted acid and basic sites of Al-OH decrease from a reaction of SiO$_2$ precursor and hydroxyl sites of Al$_2$O$_3$ [96, 97], while silanol and bridge hydroxyl groups are formed instead. The silanol and bridge hydroxyl groups are preferably accounted as acid sites [98], explaining an increase of acidity and decrease of basicity with SiO$_2$ loading. A trend of our results was consistent with the previous report for the SiO$_2$-Al$_2$O$_3$ synthesized by sol-gel method (0 to 5.4 wt% SiO$_2$) [61]. However, the strength of acid sites was significantly altered upon Si loading in our case. Therefore, a Gaussian function was adopted to deconvolute the desorption profiles of NH$_3$ into three peaks assigning to weak, medium and strong acid sites [99], in order to obtain semi-quantitative results of the distribution of acidic strength. **Table 5.3** represents the fitted results of NH$_3$-TPD experiments, the maximal temperatures (T$_M$) of weak and medium acidic sites varied

around 118-158 and 197-224 ^{o}C, respectively, depending on the SiO_2 loading, whereas the T_M of strong acidic sites of all samples remained unchanged around 336 ^{o}C for the range of SiO_2 loading in this study. The amount of weak acid sites increased and T_M shifted to higher temperature with SiO_2 loading, whereas medium strength acidic sites were very slightly decreased, from 3.0 to 2.8 area/g at low SiO_2 loading (0.6 and 1.2 wt%) and substantially increased when further increasing of SiO_2 loading to 5.6 and 12.4 wt%. However, the strong acidic sites were little changed for 0.6SiAl and 1.2SiAl samples and significantly decreased to 2.6 and 3.2 area/g for 5.6SiAl and 12.4SiAl samples, respectively. The neutralization of strong acid sites with increasing of SiO_2 loading was not observed in the case of amorphous silica-aluminas, which were simultaneously synthesized by one-pot method [37]. It might be described by the Si-coated on the Al_2O_3 surface of our Si-doped Al_2O_3, preferably forming silanol group (Si-OH) rather than bridge hydroxyl group (Si-OH-Al) [97], whereas, one-pot method synthesized newly textural architecture with more the bridged hydroxyl group which is reported as stronger Brønsted acid sites [39].

Table 5.3 Fitted results of NH_3-TPD measurement of xSiAl supports.

Catalyst	T_M (^{o}C)			Peak area (area/g)				Adj. R^2
	I	II	III	Total	I	II	III	
Al	118	197	338	8.2	1.0	3.0	4.2	0.99
0.6SiAl	143	211	336	8.5	1.7	2.8	4.0	0.99
1.2SiAl	158	224	338	8.5	1.4	2.8	4.3	0.99
5.6SiAl	133	202	336	10.2	2.9	4.7	2.6	0.99
12.4SiAl	138	207	336	9.3	2.0	4.1	3.2	0.99

5.2.3 The characteristics of Pt/Al and Pt/xSiAl catalysts.
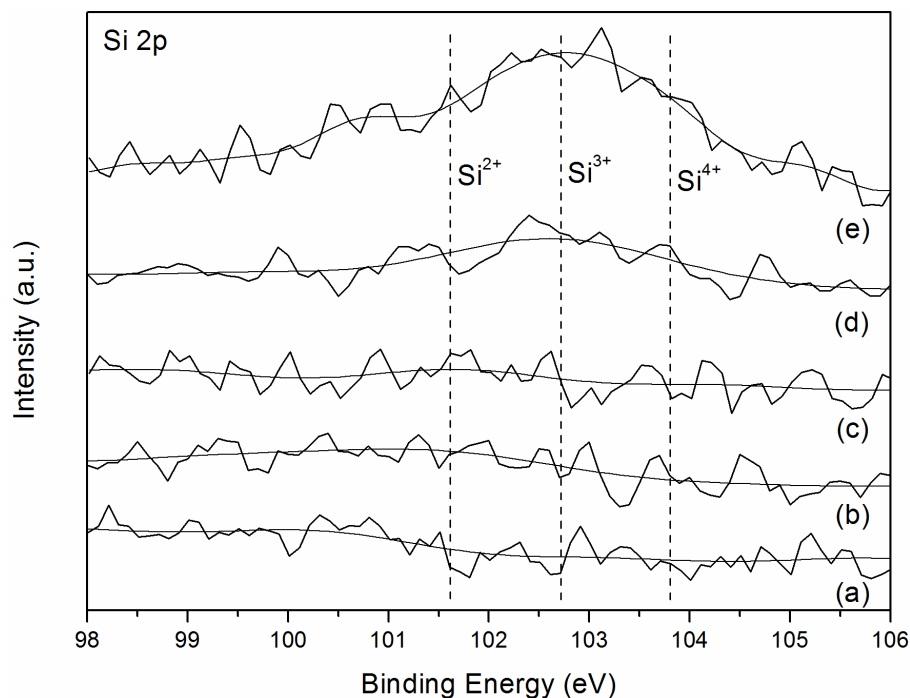
Figure 5.10 XPS spectra for Si 2p of Pt/xSiO$_2$/Al$_2$O$_3$ catalysts (a) 0, (b) 0.6, (c) 1.2, (d) 5.6 and (e) 12.4 wt% SiO$_2$

The XPS spectra for Si 2p and Si concentration analyzed by those spectra of the catalysts are displayed in **Figure 5.10** and **Table 5.2**, respectively. It is interesting to observe the appearance of a broad peaks centered around 103 eV for Pt/5.6SiAl and 12.4SiAl catalysts, which is indicative of the presence of sub oxides characters such as 101.6 eV for Si^{2+}, 102.7 for Si^{3+} and 103.8 for Si^{4+} [100]. This suggested the formation of SiO$_x$ big particles or films, whereas for those containing lower SiO$_2$ contents (0, 0.6 and 1.2 wt%), the Si sub oxides were not clearly observed, suggesting that the Si species were well dispersed and more isolated. The concentration of surface Si analyzed by XPS is presented in **Table 5.2**. The concentration of the surface Si of the catalysts (in term of Si/Al molar ratio) was 0.091 and 0.24 for Pt/5.6SiAl and 12.4SiAl catalysts, while the concentration of the others could not interpreted by XPS. However, the EDX maps for Si of all the catalysts (**Figure C.3**)

showed the degree of Si coverage, as more isolated for samples contained low SiO_2 content and more congested with increasing of SiO_2 loading.
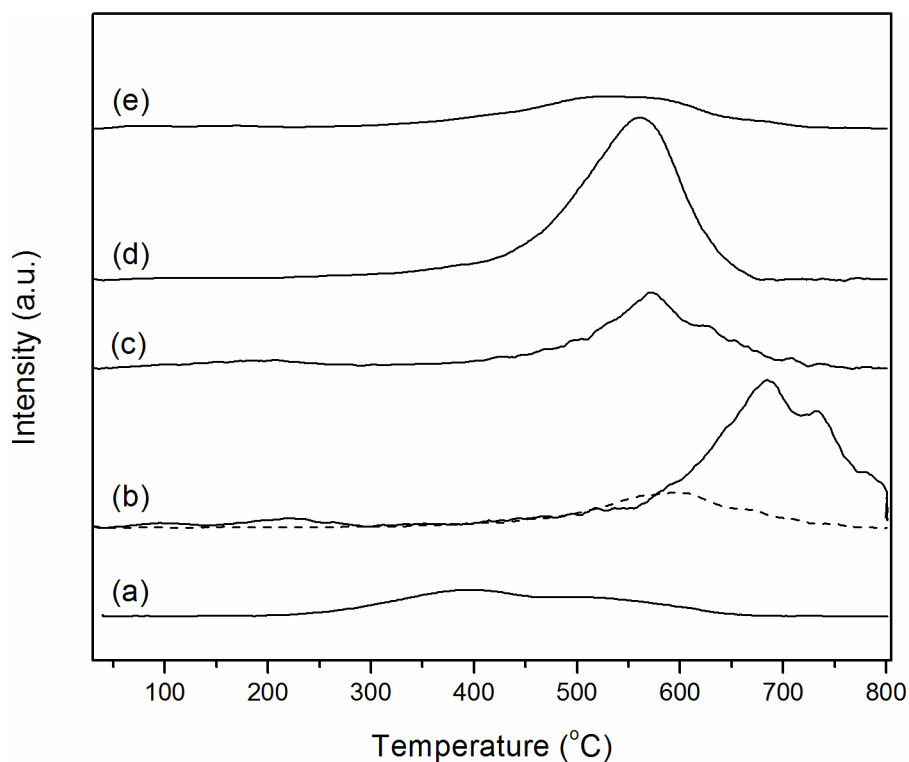
Figure 5.11 H_2-TPR profiles of Pt/xSiAl catalysts: (a) 0, (b) 0.6, (c) 1.2, (d) 5.6, and (e) 12.4 wt% SiO_2.

The reducibility of the catalysts was investigated by H_2-TPR, which is displayed in **Figure 5.11.** The H_2-TPR results showed that Pt/Al catalyst exhibited two reduction peaks, around 386 and 536 ^{o}C, respectively, in line with previous studies of Pt/Al_2O_3 catalyst [17, 101]. The former peak corresponded to the PtO_x clusters on the surface and the latter was most likely attributed to the reduction of isolated Pt species in stronger interaction with the Al_2O_3 support [102]. For a series of Pt/xSiAl catalysts, the reduction peaks greatly shifted to higher temperatures about 680 ^{o}C for Pt/0.6SiAl and declined to 570, 560 and 550 ^{o}C for Pt/1.2SiAl, Pt/5.6SiAl and Pt/12.4SiAl, respectively. The dashed line along with profile (b) represents the reduction profile of 0.6SiAl bare support. It exhibited a small peak at about 590 ^{o}C, confirming that the peak at high temperature of Pt/0.6SiAl can be accounted for the

reduction of Pt species not the reduction peak of support. The shift of reduction peaks to higher temperature demonstrated that Si significantly promoted more isolated Pt nanoparticles at low SiO_2 loading, strengthening the interaction of Pt with support. With further increased SiO_2 loading, the reduction peak shifted to lower temperature even near the undoped sample, suggesting the decrease of interaction as increasing of SiO_2 loading. However, the peak area represents H_2 consumption may not quantitatively reflect the number of Pt active sites due to isolated Pt nanoparticles had higher O coordination than agglomerated Pt clusters [103], consuming probably more H_2 to draw O atoms.

Table 5.4 CO-pulse chemisorption results of Pt/xSiAl catalysts.

Catalyst	CO uptake (µmol/g)	Dispersion (%)
Pt/Al	8.0	52
Pt/0.6SiAl	14.5	95
Pt/1.2SiAl	11.5	75
Pt/5.6SiAl	8.3	54
Pt/12.4SiAl	6.9	45

The amounts of Pt active sites measured by CO-pulse chemisorption of all the catalysts are presented in **Table 5.4**. The results reveal that SiO_2 addition significantly increased the amount of Pt active sites from 8.0 to 14.5 and 11.5 µmol/g cat. for 0.6SiAl and 1.2SiAl, respectively. These trace amount Si-doped Al_2O_3 are among the highest dispersed Pt states on aluminosilicate supports, as shown by the comparison with the literature data in **Table D.1**. However, further increasing of the SiO_2 content to 5.6 and 12.4 wt%, led to a decline in the amount of Pt active sites were slightly declined to 8.3 and to 6.9 µmol/g, respectively. According to the H_2-TPR results, the strong interaction between Pt and support appeared on Si-doped Al_2O_3 support, especially at low amount of SiO_2 loading (Pt/0.6SiAl and Pt/1.2SiAl). However, the decrease of interaction was consistent with the decline of Pt dispersion of Pt/xSiAl catalysts when increasing of SiO_2 loading. This behavior may be attributed to that increasing of SiO_2 content may result in partial coverage of the Al_2O_3 surface by SiO_2

in line with the decline of N_2 physisorption results and significant loss of basicity. In addition, Pt particles could be more sintered under reduction environment when bonded with the SiO_2-covered surface due to the lower metal-support interaction compared to γ-Al_2O_3 [8]. While Pt dispersion was greatly increased by 82 % and 45% for 0.6 and 1.2 wt% SiO_2-doped Al_2O_3, respectively with trace amount of Si addition. The effect of low amount of SiO_2 loading would be different from high SiO_2 loading or the creation of PtSi alloy, corresponding to the significant shift of H_2-TPR peak to higher temperature than 600 $^\circ$C [104, 105]. The presence of low amount of SiO_2 may retard aggregation of PtO_x species by strong interaction between Pt-support or Pt-Si of PtSi alloy system [104] under the severe conditions of reduction treatment.
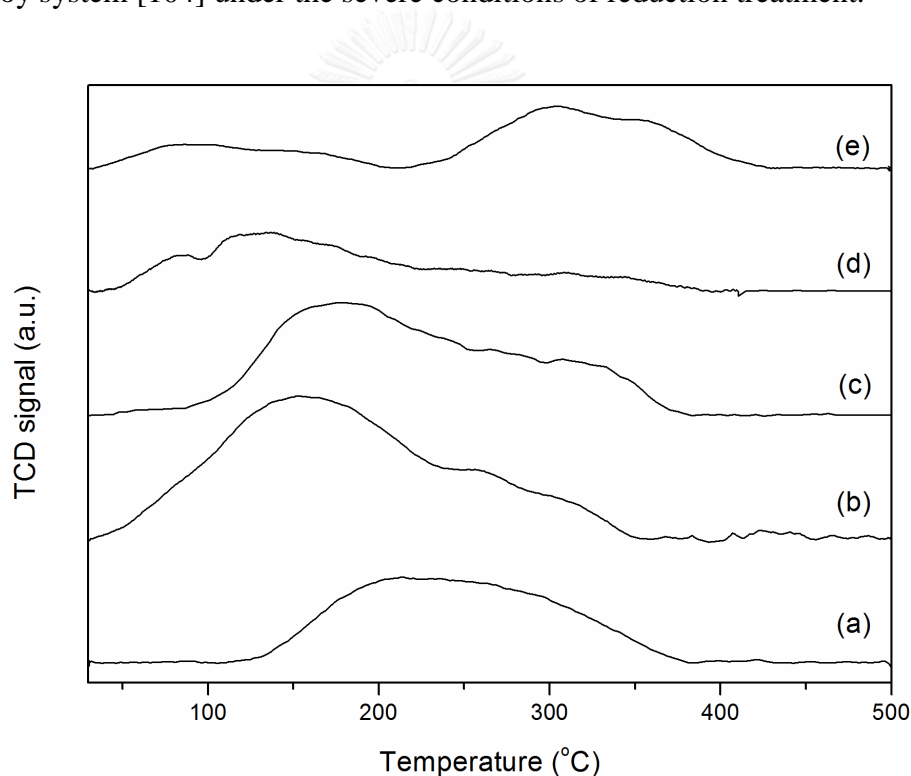
Figure 5.12 CO-TPD profiles of xSiAl supported Pt catalysts (a) 0, (b) 0.6, (c) 1.2, (d) 5.6 and (e) 12.4 wt% SiO_2.

The interaction of Pt-CO was examined by CO-TPD and the results are shown in **Figure 5.12**. The peak areas of the CO-TPD profiles represented both CO and CO_2 even it were in accordance with the area obtained from pulse-CO chemisorption. The plausible mechanisms of CO_2 formation have been proposed including water gas shift

with hydroxyl group, Boudouard reaction, and CO oxidation with O_2 at ppm level contained in carrier gas [106]. However, regardless of the mechanism, CO_2 could be produced and desorbed after or at least simultaneously with CO desorption as observed in literature [106-108], implying that our CO-TPD results could still be used to investigate the interaction between Pt and chemisorbed-CO. The Pt/Al exhibited broad peak with maxima around 230 ^{o}C and complete desorption at nearly 390 ^{o}C, corresponded to CO adsorbed on small Pt particles on alumina [107, 109]. For the 0.6, 1.2 and 5.6SiAl supported Pt catalysts, the adsorbed CO species at lower temperature were increased resulting in a shift of the main peaks to lower temperatures at 153, 175 and 133 ^{o}C, respectively. However, in the case of Pt/12.4SiAl, the CO-TPD was split into two main peaks at temperatures of nearly 80 and 304 ^{o}C, respectively. It can be seen that weakly bonded CO species increased by SiO_2 addition in the range of 0.6-12.4 wt% with inverse of SiO_2 content. It is demonstrated that SiO_2 altered the interaction of Pt-CO into weaker and stronger interaction. The weaker CO species may cause by the PtSi alloy [104] and these species decreased as the SiO_2 content increased. The appearance of Pt-SiO_2 analogous catalyst occurred at higher SiO_2 loading, matching with the desorption peak of stronger CO species at around 300 ^{o}C [110].

5.2.4 Catalyst activity in CO oxidation

The CO conversion profiles as a function of reaction temperature are shown in **Figure 5.13**. The Pt/0.6SiAl showed superior activity in CO oxidation with the lowest temperatures at 175 and 190 ^{o}C for 50 and 100 % conversion, respectively. With increasing SiO_2 content from 1.2 to 5.6 and 12.4 wt%, T_{50} increased from 175 to 186, 220 and 232 ^{o}C, respectively. Such results can be clearly observed in a plot of T_{50} against Pt active sites (**Figure 5.14**).
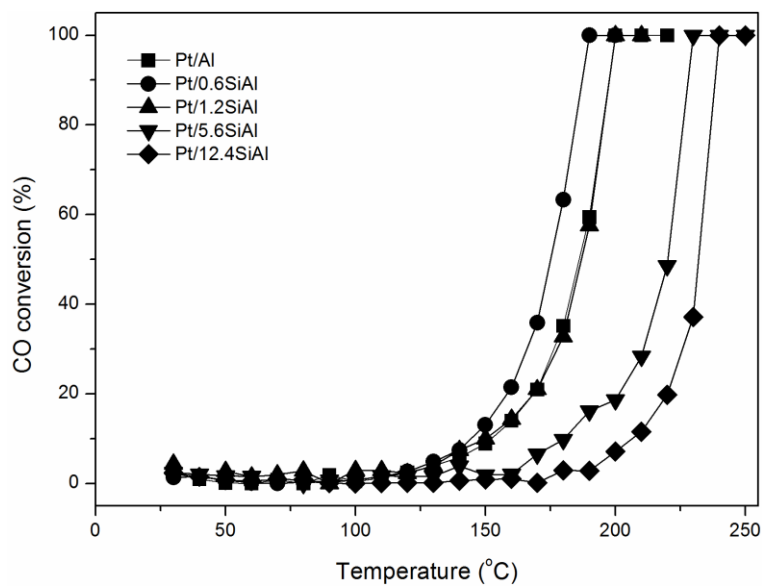
Figure 5.13 The CO conversion profiles of Pt/xSiAl catalysts (reaction condition: CO 0.5; O_2 1; He 48.5 ml/min).
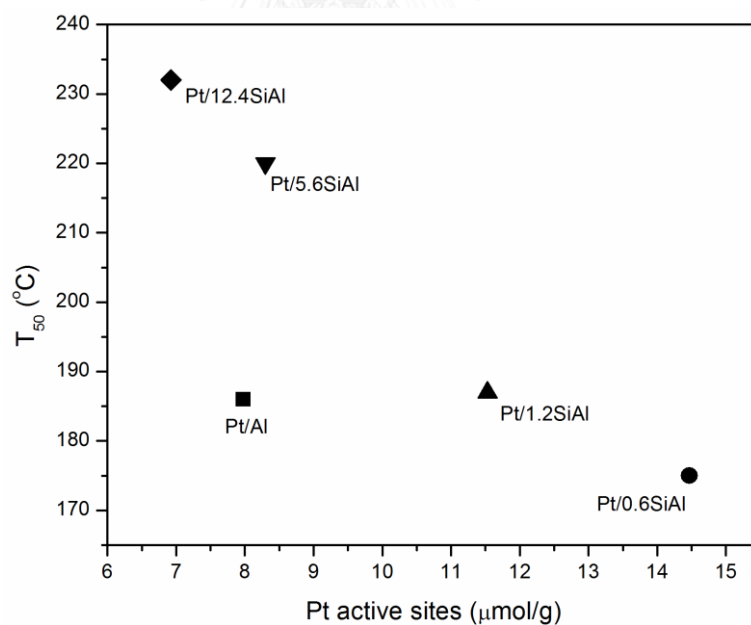
Figure 5.14 Relationship of T_{50} and Pt active sites of Pt/xSiAl catalysts (Pt active sites were measured by CO-chemisorption).

The undoped Pt/Al exhibited T_{50} at 185 $^{\circ}$C close to the Pt/1.2SiAl sample with lower Pt dispersion. For the 5.6 and 12.4SiAl samples, T_{50} were much higher than the undoped γ-Al$_2$O$_3$. Obviously, the catalytic activity of the Pt/xSiAl catalysts increased with increasing of Pt active sites (decreasing of the SiO$_2$ content). However, the catalytic activities of a series of Si-doped catalysts were relatively low compared with the Pt/Al catalyst, and so we should consider another effect in addition to Pt active sites in order to fulfill the explanation. It is interesting to note that the Pt-CO interaction was expected to be another factor influencing the CO oxidation activity besides Pt dispersion. As reported by many authors, lower desorbed temperature resulted in higher CO oxidation activity [111] because O$_2$ could start to adsorb on available Pt sites after covered-CO desorbed. However, the CO-TPD of the Pt/1.2SiAl and Pt/5.6SiAl samples revealed higher amounts of weakly bound CO species than the undoped one, as a consequence these samples would have more available Pt sites at similar temperature but they exhibited lower CO oxidation activity. Thus, the reaction results could not be obviously explained by this sole hypothesis.

5.2.5 Effect of oxygen mobility on catalytic activity

From the CO chemisorption and the CO-TPD results, it is suggested that CO activation was not the only significant factor influencing CO oxidation activity. Regarding O$_2$ activation, different phenomena should be considered including adsorption, mobility, and storage. It is well known that Al$_2$O$_3$ support could not activate O$_2$ itself without metal [112, 113] and has essentially no capacity to store O$_2$ in the lattice framework [114]. Moreover, on Pt/Al$_2$O$_3$ catalyst, O$_2$ adsorption is usually inhibited by covered-CO in CO oxidation. Thus, the lower desorption temperature of CO would render more available Pt sites to adsorb O$_2$. The effect of oxygen mobility on the combustion of coke covered on different oxide- supported Pt catalysts was studied by Vu et al. [26]. The higher oxygen mobility of the support was found to result in lower temperature of coke combustion. Therefore, oxygen mobility may play a distinct role in activation steps for supported Pt catalysts in oxidation reaction. According to Martin and Duprez [25], the rate of oxygen surface diffusion was practically linked to the amount of basic sites in which the higher basic sites

exhibited higher oxygen mobility. Because metal-oxygen bond strength decreases as basicity increases [78], the O_2 movement on the surface is easier.
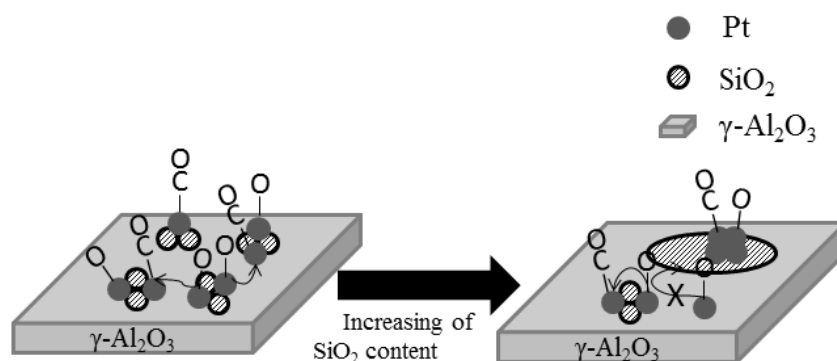
Figure 5.15 Proposed structural model of Pt/xSiAl catalysts and possible mechanism of CO oxidation over the catalysts.

The proposed structural model of Pt/xSiAl catalysts and possible mechanism of CO oxidation over these catalysts are shown in **Figure 5.15**. It is suggested by the XPS spectra for Si 2p and EDX maps that at low SiO_2 content, SiO_2 species were more isolated on the surface of γ-Al_2O_3 while at high SiO_2 content, clusters or films of SiO_2 could be formed. As the surface of γ-Al_2O_3 was greatly covered with SiO_2, occurrence of Si sub oxides and substantial reduction of basicity was observed. The isolated SiO_2 sites could maintain highly dispersed Pt states while SiO_2 clusters or films could not, leading to lower Pt dispersion at high SiO_2 content. Moreover, these SiO_2 species retarded oxygen movement on the surface, resulting in the decrease of reaction rate per sites. Such results suggest that the surface reaction between CO and O activated by differently adjacent Pt clusters is included in the CO oxidation mechanism.
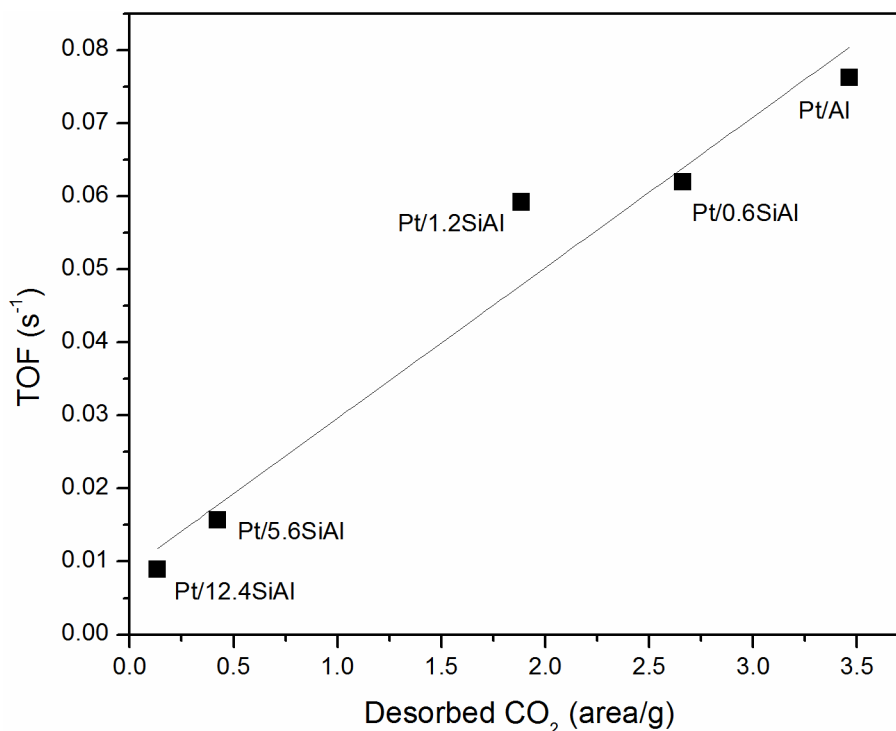
Figure 5.16 Relationship between TOF and basicity of the series of Pt/xSiAl catalysts.

In order to emphasize the effect of oxygen mobility on CO oxidation in addition to the major influence of Pt active sites, the reaction rate per active site (TOF) concept is considered to be used for comparison as a function of desorbed CO_2 because it is generally insensitive to the Pt particle size [54, 115]. The relationship of TOFs and desorbed CO_2 is shown in **Figure 5.16**. It can be seen that the TOFs increased as the amount of desorbed CO_2 increased (decreasing SiO_2 content). A linear relationship with R^2 of nearly 0.96 highlighted the effect of oxygen mobility relating to support basicity in oxidation reaction [116, 117] and confirms that not only Pt dispersion but also oxygen mobility play important roles in the CO oxidation activity of supported Pt catalysts.
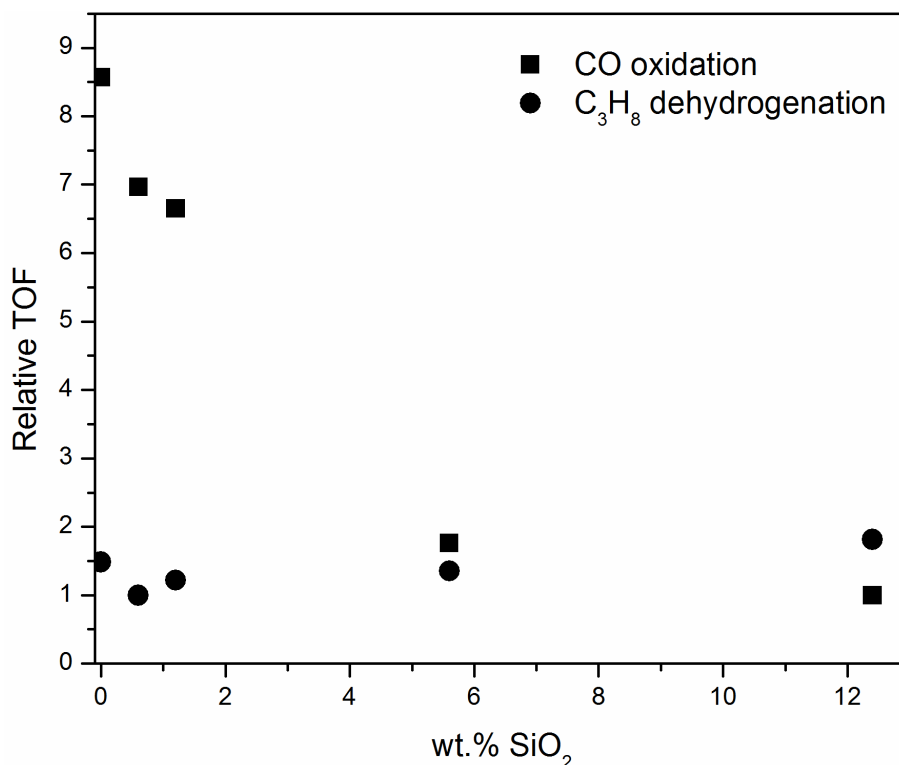
Figure 5.17 Comparison of relative TOFs of Pt/xSiAl catalysts in CO oxidation and C_3H_8 dehydrogenation.

In order to strengthen the proposed model, a series of Pt/xSiAl catalysts were tested in the dehydrogenation of C_3H_8 as a non-oxidative structure-insensitive reaction [27]. A comparison of the relative TOFs of Pt/xSiAl catalysts in CO oxidation and C_3H_8 dehydrogenation (the TOFs were divided by the lowest value of each reaction) are shown in **Figure 5.17**. It can be clearly seen that the relative TOFs of CO oxidation monotonically decreased about 8.6 times as the SiO_2 content increased whereas the relative TOFs of C_3H_8 dehydrogenation were almost unchanged, confirming the structure-insensitive characteristic. In other words, the catalytic activity depends only on the number of Pt active sites when tested with a probe reaction without oxygen as a reactant. It is confirmed that oxygen mobility plays an important role in CO oxidation mechanism and can be tuned with SiO_2 loading.

5.2.5 Catalyst performance in propane dehydrogenation

The catalytic performance of the Pt/xSi-Al catalysts is depicted in **Figure 5.18**, showing the conversion **(a)** and selectivity **(b)** as a function of time on stream. The initial propane conversion of Pt/Al, Pt/0.6SiAl, Pt/1.2SiAl, Pt/5.6SiAl, and Pt/12.4SiAl were 26.4, 32.3, 31.1, 25.0, and 27.9%, respectively. After 3 h of time on stream, the conversion decreased to 9.2, 11.0, 9.9, 8.5, and 9.4% with the calculated deactivation constants (k_d) of 0.43, 0.46, 0.48, 0.44, and 0.45 h^{-1}, respectively. It can be seen that Si addition significantly promoted the propane conversion upon SiO_2 loading. The propane conversion of the catalysts was well correlated with Pt dispersion, indicating the lack of structure-sensitivity of propane dehydrogenation [27]. The highest activity was obtained on Pt/0.6SiAl catalyst owing to the highest Pt dispersion. However, stability of the catalysts was not promoted by the Si addition as the deactivation constants of all the catalysts were nearly similar.
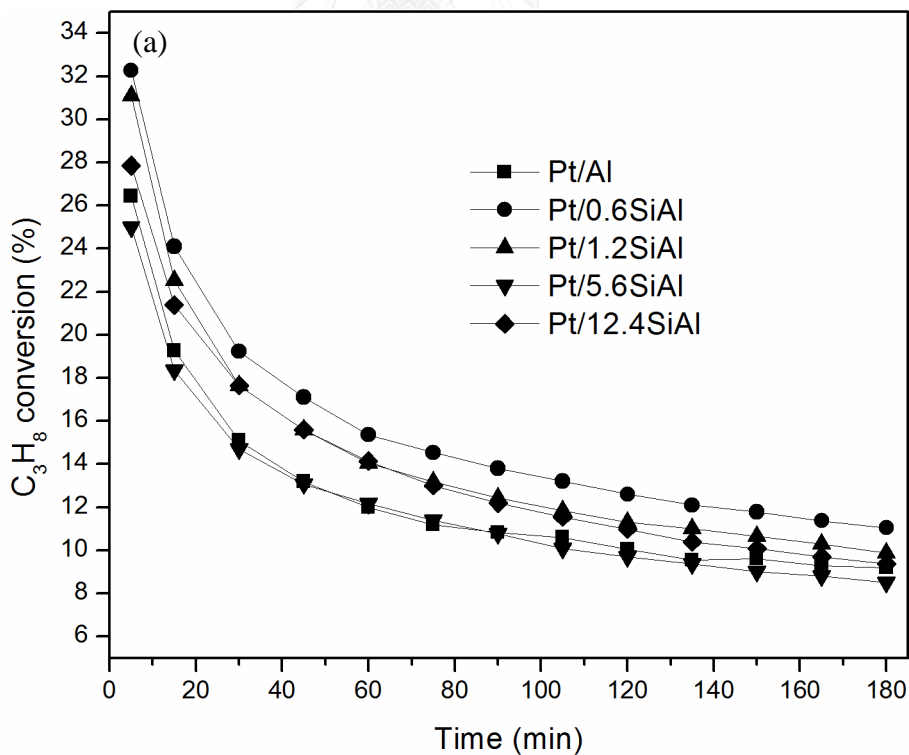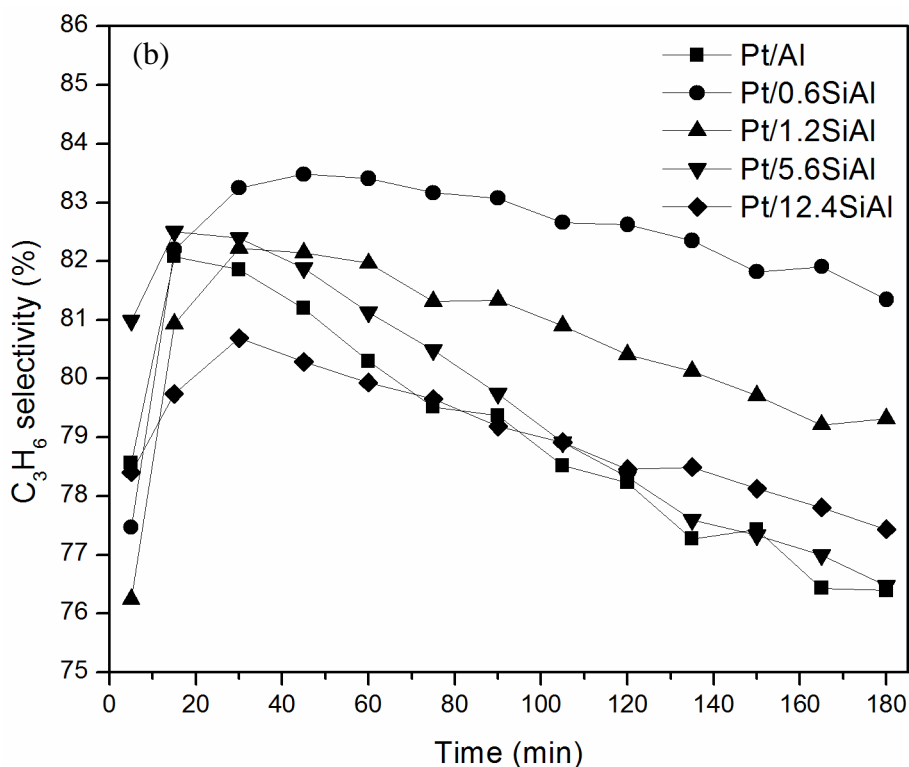
Figure 5.18 Catalytic performance of Pt/xSiAl catalysts in propane dehydrogenation: (a) propane conversion and (b) propylene selectivity; other observed products were CH_4, C_2H_4, and C_2H_6 (reaction condition: C_3H_8 15; H_2 5; He 30 ml/min at 600 ^oC).

The initial selectivity of the catalysts followed the order of 5.6 > 0 > 12.4 > 0.6 > 1.2SiAl supported Pt catalyst, respectively. After that, the selectivity sharply increased to maximum and slowly declined upon time on stream. The low selectivity of all catalysts at the beginning can be explained by the higher amount of low coordination Pt sites (steps, corners and edges) of the fresh catalyst, which are believe to respond for the hydrogenolysis reaction [118, 119] and it were selectively deactivated by coking shortly as the selectivity increased [120]. As isomerization, hydrogenolysis, and the formation of coke precursors has been suggested that they can all be diminished by decreasing the size of Pt nanoparticles [27], as well as previous studies demonstrated that side reactions were also catalyzed by the strong acid sites. Thus, the Pt particles sites and strong acid sites are expected to mainly influence the selectivity. After 3 h on stream, the propylene selectivity for 0, 0.6, 1.2, 5.6, 12.4SiAl supported Pt catalysts were 76.4, 81.3, 79.3, 76.5, and 77.4,

respectively. The results showed that addition of Si had a positive effect, enhancing propylene selectivity. The higher propylene selectivity of Pt/0.6SiAl and Pt/1.2SiAl with nearly amount of strong acid sites highlighted the size effect of Pt nanoparticles. However, the Pt/5.6SiAl and Pt/12.4SiAl catalysts which revealed substantially lower strong acid sites only showed better propylene selectivity at the beginning of reaction and declined promptly. This suggested that metal-support interaction plays a crucial role in enhancing and sustaining propylene selectivity beside the acid characteristics. The highest propylene selectivity after initial period is obtained on Pt/0.6SiAl catalyst, which may be attributed to the maintaining of smaller Pt sites by the strongest interaction of Pt and support, corresponding to the H_2-TPR results.

5.2.6 Carbon deposition of spent catalysts

Table 5.5 Summary of TPO experiments of spent Pt/xSiAl catalysts.

| Spent catalyst | T_M (^oC) | | Total carbon | Carbon content (wt. %) | | k_d |
	I	II	(wt. %)	I	II	(h^{-1})
Pt/Al	448	618	7.0	5.5	1.5	0.43
Pt/0.6SiAl	470	560	7.8	7.0	0.8	0.46
Pt/1.2SiAl	470	580	6.9	5.9	1.0	0.48
Pt/5.6SiAl	527	568	5.1	4.6	0.5	0.44
Pt/12.4SiAl	529	605	6.6	5.9	0.7	0.45

The amount of carbon deposition of the spent catalysts was quantitatively determined by thermogravity analyzer and is summarized in **Table 5.5**. It was found that addition of Si increased amount of carbon deposition from 7.0 to 7.8 wt.% on spent Pt/0.6SiAl and declined afterwards when further increased SiO_2 loading as 6.9, 5.1 and 6.6 wt.% carbon for Pt/1.2SiAl, Pt/5.6SiAl and Pt/12.4SiAl, respectively. The higher amount of carbon deposition on spent Pt/0.6SiAl catalyst might be explained by the much higher Pt active sites with close acid characteristics, while spent Pt/5.6SiAl and Pt/12.4SiAl catalysts revealed lower amount of coke especially only

5.1 wt% carbon for Pt/5.6SiAl. It can be addressed to the less Pt active sites and considerably lower of strong acid sites which is assigned to be the main reason for coke formation [121].
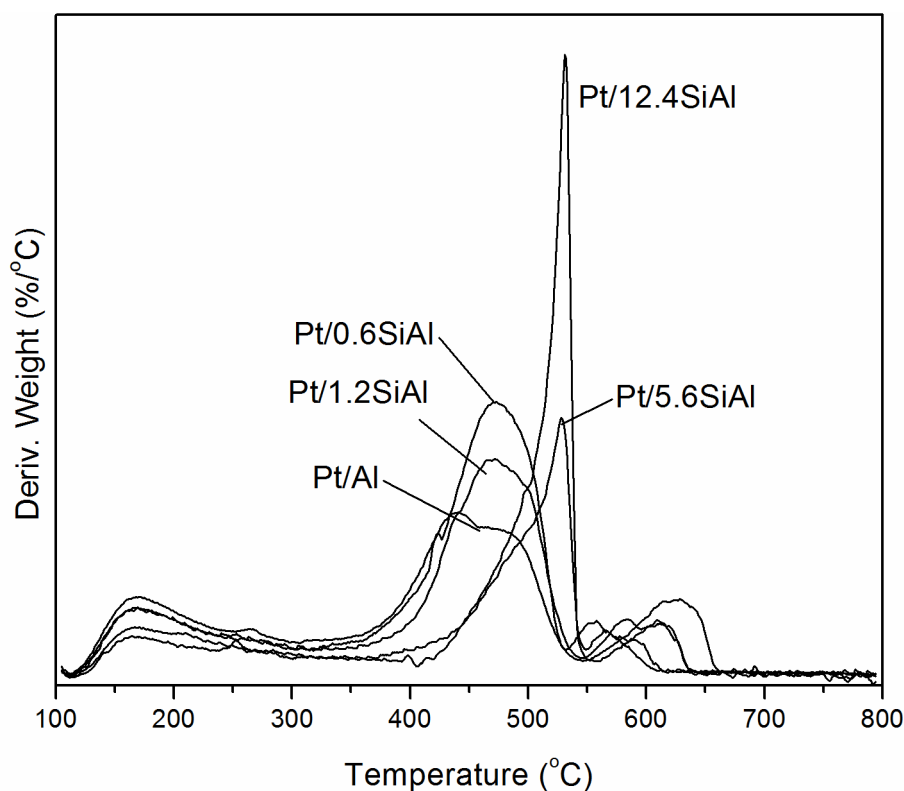
Figure 5.19 TPO profiles of spent Pt/xSiAl catalysts.

The TPO profiles of the catalysts are shown in **Figure 5.19** and the deconvoluted results of various coke species are summarized in **Table 5.5**. For all catalysts, coke species could be separated into 2 species by the combustion temperatures. First and second peaks can be assigned to coke deposited on metal and support, consequently [33]. It can be seen that coke on the Pt sites (first peak) were 5.5, 7.0, 5.9, 4.6, and 5.9 wt% for 0.6, 1.2, 5.6, and 12.4SiAl supported Pt catalysts, respectively. The amount of coke deposited on Pt active sites correlated to the initial conversion, suggesting that Si addition did not considerably facilitate the transfer of coke from metal to support. However, coke on the support (second peak) was significantly reduced from 1.5 to various 0.5 - 1.0 wt% depending on SiO_2 loading, in

a good agreement with the fitted results of strong acid sites, indicating that Si addition could importantly suppress coking on the support. The shift to higher combustion temperatures of coke species I for Pt/5.6SiAl and Pt/12.4SiAl were probably due to the lower oxygen mobility of Si-doped Al_2O_3, demonstrating by the substantial reduction of surface basicity [25, 26].

5.3 Microscopic and spectroscopic determination of the locations of the single-site Pt in KLTL zeolite as a CO oxidation catalyst

Supports used in the previous sections were less-crystalline, providing random bonding sites for Pt catalyst. Nevertheless, the approaching of fundamental understanding is still challenging owing to the essential of combined various advanced characterization techniques. Therefore, in this Section 5.3, we showed how highly crystalline support give an opportunity to understanding of LTL zeolite supported single-site Pt CO oxidation catalysts as industrial relevant catalyst. The catalysts were characterized with combination of spectroscopies (IR, XANES and EXAFS) and microscopy (STEM), defining locations of single-atom Pt species (the highest Pt dispersion) and relating structure with catalytic performance.

5.3.1 Characterization of single-site Pt complexes

IR spectra (**Appendix H**) of the calcined zeolite and the samples made from it indicate that after calcination it contained little water or acidic OH groups, consistent with the initial K/Al atomic ratio of essentially unity, determined by elemental analysis (**Appendix E**). N–H deformation bands in the IR spectra (1350 and 1390 cm^{-1}) show that $[Pt(NH_3)_4]^{2+}$ complexes were present in the zeolite, as expected [122]. The bands in the v_{OH} region representing hydroxyls in the zeolite framework decreased upon incorporation and oxidation of the platinum complexes. After oxidation, the band at 3743 cm^{-1}, assigned to zeolite silanol groups [123], was the only band remaining, consistent with the expectation that the platinum complexes had preferentially undergone ion exchange with K$^+$ ions located near zeolite Al atoms rather than Si atoms [51, 124].

Pt L$_{III}$ edge EXAFS spectra of this catalyst (**Table 5.6**, fitting details in **Appendix G**) are in accord with the IR data, indicating a Pt–N shell with a coordination number of nearly 4. The Pt–O$_{support}$ coordination number of nearly 2 indicates that each Pt atom was bonded, on average, to two zeolite surface oxygen atoms. The absence of a detectable Pt–Pt shell indicates that the platinum species

were mononuclear. The Pt–Al coordination number of nearly 1 confirms that the platinum was present in cation exchange sites.

XANES spectra of the as-prepared sample and that oxidized in 10% O_2 in He at 360 ^{o}C indicate Pt L_{III} edge energies of 11567.2 and 11566.8 eV, respectively. The former value is greater than that characterizing bulk platinum (11564 eV) and similar to those characterizing Pt(II) complexes [125], including those supported on Al_2O_3 [126]. The white line intensity and XANES features of the as-prepared sample at approximately 11580 eV nearly match those of Pt(II) tetraamine complexes [126]. The white line intensity increased during oxidation (**Figure H.3**), indicating an increase in the number of oxygen donor atoms without a change in the platinum oxidation state [127, 128], corresponding to the unchanged edge energy [129] and the increase from 2 to 3 of the Pt–O coordination number representing oxygen atoms bonded to Pt after the oxidation (**Table 5.6**).

When the supported $[Pt(NH_3)_4]^{2+}$ complexes were oxidized in flowing 10% O_2 in He as the temperature was ramped from 25 to 360 ^{o}C at 3 ^{o}C min^{-1}, most of the NH_3 ligands were oxidized. IR band intensities show that ~15% of these ligands remained unoxidized after 4 h at 360 ^{o}C (**Figure H.1**). We stopped short of further oxidation because our goal was to investigate mononuclear platinum species, and reported results [130] show that the fully deaminated platinum complex in zeolite NaX underwent autoreduction. As the sample was oxidized, mass spectra of the effluent gases showed that water evolution started at ~50 ^{o}C and N_2 and NO evolution at 193 ^{o}C, confirming the oxidation of the ligands (**Figure H.5**) [130].

EXAFS data characterizing the oxidized sample PtO$_x$/KLTL zeolite (**Table 5.6**) indicate average Pt–N and Pt–O coordination numbers of 0.6 and nearly 3, respectively, and thus a mixture of oxidized and unoxidized platinum complexes, consistent with the remaining NH_3 deformation bands in the IR spectra and the Pt–O$_{long}$ and Pt–Al coordination numbers of approximately 6 and 1 at distances of 2.6 and 3.2 Å, respectively. A precise determination of the nuclearity of the platinum species is provided by STEM images (**Figure 5.20**), which confirm the absence of platinum clusters and show exclusively site-isolated single Pt atom species both before and after oxidation.

Table 5.6 EXAFS parameters[a] characterizing platinum complexes in KLTL zeolite before and after oxidation.[b]

Sample	Coordination shell	N	R (Å)	$10^3 \times \Delta\sigma^2$ (Å^2)	ΔE_0 (eV)
Pt(NH$_3$)$_4$$^{2+}$/ KLTL zeolite (as-prepared)	Pt–N	4.0	2.00	4.2	-7.3
	Pt–O$_{short}$	2.0	2.05	2.3	8.0
	Pt–O$_{long}$	6.0	2.68	7.0	3.7
	Pt–Al	1.0	3.00	6.5	-11.0
PtO$_x$/ KLTL zeolite (oxidized)	Pt–N	0.6	2.00	1.2	-1.8
	Pt–O$_{short}$	2.8	2.01	8.9	-3.8
	Pt–O$_{long}$	5.9	2.64	10.5	8.0
	Pt–Al	1.1	3.19	2.6	11.3

[a] Sample before oxidation (Δk = 4.0–10.6 Å^{-1}, ΔR = 0.8–3.3 Å). Sample after oxidation (Δk = 4.1–11.6 Å^{-1}, ΔR = 0.5–3.0 Å). [b] Notation: N, coordination number; R, distance between absorber and backscatterer atoms; $\Delta\sigma^2$, disorder term; ΔE_0, inner potential correction. Estimated error bounds (accuracies): N, ±20%; R, ±0.02 Å; $\Delta\sigma^2$, ±20%; ΔE_0, ±20%, but these values do not pertain to the Pt–Al contributions, for which the errors are greater.

Figure 5.20 STEM images showing site-isolated Pt atoms in KLTL zeolite in the (a) oxidized and (b) as-prepared samples.

White features in dashed blue circles indicate Pt atoms. Magnified views (c–e) of the highlighted regions in (b), containing one Pt atom each at A/B sites in (c), at C/E sites in (d), and at D sites in (e) (notation stated in **Figure 5.21** caption). Simulations (f–g) of the LTL zeolite in the [110] direction superimposed on the magnified views in (c–e), showing Pt atoms (green) at A/B sites in (f), at C/E sites in (g) (purple), and at D sites in (h) (red). Pt atoms are located right at the edge of the 12-membered rings of site D; between the two 12-membered rings of sites C/E; and in the center of three 12-membered rings of sites A/B.

5.3.2 Locations determination by STEM

Figure 5.21 Schematic models of zeolite LTL with (a) pore nomenclature as referred to in **Figure 5.20**, (b) $[Pt(NH_3)_4]^{2+}$ and (c) PtO_x located in the 8-membered ring at the C site.

The 5 unique bonding locations (A-E) of the Pt atoms are described elsewhere [51, 124]. Pt–O bond distances determined by EXAFS spectroscopy were used to determine the Pt atom locations. Color scheme: O (red), T-site Si/Al (purple), Pt (green), nitrogen (blue), H not shown for simplicity. Models depicting the platinum complexes in other pore locations are shown in **Appendix F**.

In contrast to images of site-isolated Pt atoms reported previously [6, 42], ours determine the precise locations within the pore structure of the support. The $[Pt(NH_3)_4]^{2+}$ complexes present initially were located primarily in D sites in the largest pores (66%) (**Figures 5.20 and 5.21**). The remainder were in smaller pores, 23% in A/B sites and 11% in C/E sites (notation in caption, Figure 2). Some Pt atoms moved as a result of the oxidation, with the approximate population present in the largest pores decreasing to 56%, that in the medium-sized A/B pores remaining almost unchanged at 24%, and that in the smallest C/E pores increasing to 20%. Details of the STEM calculations are in **Appendix F**. The result confirms previous reports that platinum complexes located in the D sites readily migrate to the E sites upon oxidation [51, 124].

The EXAFS data show that the surroundings of the Pt atoms, on average, also changed as a result of the oxidation, in agreement with the STEM images. Because the average Pt–O coordination number at the bonding distance of nearly 2.0 Å increased from 2 to nearly 3 (**Table 5.6**), we postulate that the oxidation led to the formation of platinum oxo species [131], with approximately one oxo O atom per Pt atom, corresponding to the increase in the Pt–O coordination number. These oxo ligands could be stabilized by the lack of significant electron accepting ligands (recall that the zeolite acts as a ligand). Similar results were obtained by EXAFS spectroscopy for a sample made from [Pt(NH$_3$)$_4$$^{2+}$] in zeolite NaY oxidized at 360 ^{o}C [132].

5.3.3 CO oxidation catalysis

The platinum sites in the zeolite were probed with a catalytic test reaction, CO oxidation. The zeolite alone lacked measurable catalytic activity at temperatures up to 150 ^{o}C, but the platinum-containing zeolite was active both before and after oxidation under conditions described below. The data determine the rate of reaction in each catalyst, measured as turnover frequency (TOF), found by extrapolation of low-conversion data to zero on-stream time. The initial TOF characterizing the as-prepared sample was 0.0038 s^{-1} at 150 ^{o}C with a feed of 1% CO and 5% O$_2$ in He; that characterizing the oxidized sample was 0.012 s^{-1}; our catalysts are among the most active for CO oxidation under our conditions, as shown by the comparison with literature data in **Appendix I**. As expected, the activity of the former catalyst in O$_2$ increased with time on stream in the flow reactor, as oxo ligands presumably formed and facilitated CO oxidation [131]. Furthermore, IR spectra of the catalyst before CO oxidation and recorded after exposure to just CO (**Figure H.4**) gave no evidence of CO adsorption on the coordinatively saturated Pt(NH$_3$)$_4$$^{2+}$ species at 25 ^{o}C, but the oxidized sample was characterized by a strong, broad CO absorption centered at 2100 cm^{-1}, indicating bonding of CO to the oxidized, catalytically active platinum sites [131, 133, 134].

5.3.4 Highlight the effect of oxygen mobility on CO oxidation by isolated single-site Pt catalysts

The single-site Pt catalysts in channels of KL zeolite are isolated which the transfer of reactant species were not observed [103], suggesting that the oxygen mobility could not occur on the catalyst. Thus, the isolated Pt sites catalyst could be used as a model to emphasize the effect of oxygen mobility by comparison of turnover frequency of Pt catalyst supported on negligible-mobile oxygen species support (Pt/12.4SiAl) to the isolated single-site Pt catalytic sites. It was found that the TOF of Pt/12.4SiAl (0.0088 s^{-1}) was in similar order of magnitude to the isolated single-site Pt oxo species (0.012 s^{-1}).

CHAPTER 6
CONCLUSIONS AND RECOMMENDATIONS

This chapter brings the scientific conclusion from the results studied in this work. Moreover, the results which are interesting and still need more detailed to address are also recommended to further investigate in the future works.

6.1 Conclusions

Dispersity of Pt active sites on γ-Al_2O_3 could be effectively enhanced by incorporating χ-Al_2O_3 and Si via solvothermal method, impregnating Si with appropriate amount. The H_2-TPR results exhibited that Si addition strengthened the metal support interaction especially at 0.6 wt% of SiO_2 loading and declined with increasing of SiO_2. The strong metal-support interaction promoted highly dispersed Pt sites, as Pt dispersion was greatly improved by 82 and 45 % on 0.6 and 1.2 wt% SiO_2-doped Al_2O_3 support and declined afterward. The amount of basic sites (desorbed CO_2) as representative of oxygen mobility was slightly decreased when modifying with χ-Al_2O_3. However, regardless of whether solvothermal or impregnation, Si addition decreased the amount of basic sites and further decreased as increasing of SiO_2 content. A relationship between TOFs of CO oxidation and desorbed CO_2 indicated that oxygen mobility is another important factor determining CO oxidation activity. It is suggested plausible mechanism of the surface reaction between CO^* and O^* surface species, which were activated by different adjacent Pt clusters. The mechanism was strengthened by the TOFs of the modified catalysts in propane dehydrogenation (without oxygen as a reactant) remained unchanged. The superior CO oxidation catalyst can be obtained by incorporating χ phase and impregnating 0.6 wt% of SiO_2 into γ-Al_2O_3 because it optimized between enhancement of Pt dispersion and diminution of the oxygen mobility. In addition, the highly dispersed Pt catalysts on modified γ-Al_2O_3 can be applied in propane dehydrogenation as the results demonstrated the promotional effect on catalytic performance for propane dehydrogenation over Pt supported on χ phase- and Si-modified γ-Al_2O_3. Moreover,

addition of Si via impregnation also partly neutralized strong acid sites, which increasing propylene selectivity and decreasing coke formation but this effect was emphasized at high SiO_2 loading (5.6 and 12.4 wt%). The superior propane dehydrogenation catalyst was obtained at 0.6 wt% of SiO_2 loading, which had strongest metal-support interaction, resulting in highest conversion and selectivity. Furthermore, fundamental understanding could be approached when using highly crystalline support (KLTL zeolite) instead of transition-crystalline γ-Al_2O_3. KLTL zeolite provides nearly uniform binding site for Pt active species, presenting the first site-isolated Pt catalyst with locations of Pt atoms defined. The catalytic activity also related to chemical environment of Pt active species. The single-site Pt catalyst highlights the effect of oxygen mobility on CO oxidation as the TOF of Pt catalyst supported on negligible-mobile oxygen species support (12.4 wt% SiO_2 loading of Si-doped Al_2O_3) was in similar order of magnitude to the isolated single-site Pt catalyst. The results indicated that the oxygen mobility significantly influences the turnover frequency of the catalysts in oxidative structure-insensitive reactions whereas negligibly influences in non-oxidative structure-insensitive reactions. The results of this work also demonstrated a strong advantage of tuning the support characteristics (dopants, SiO_2 content and crystallinity) for not only applications in catalysis research by improving catalytic performance but also fundamental understanding of supported catalysts and opportunities for tailoring stable single-site catalysts; they pointed the way to distinguishing atomically dispersed metal catalysts from metal clusters and describing structure-activity relationship.

6.2 Recommendations

- To address the better explanation of high Pt dispersion on Si-doped γ-Al_2O_3 at low loading by characterizing with STEM, XPS, and in-situ XANES during H_2-reduction.
- To clarify how the strong platinum-support interaction occurred over low amount Si-doped Al_2O_3
- To characterize via the isotope exchange to clarify more detail of O_2 mobility related to surface basicity and their role in reaction mechanism.

- To synthesize single-atom Pt catalyst via more practical method and stable in harsh-atmosphere reactions.

REFERENCES

[1]   Mazzieri, V.A., Pieck, C.L., Vera, C.R., Yori, J.C., and Grau, J.M. Effect of Ge content on the metal and acid properties of Pt-Re-Ge/Al_2O_3-Cl catalysts for naphtha reforming. Applied Catalysis A: General 353 (2009): 93-100.

[2]   Santikunaporn, M., et al. Ring opening of decalin and tetralin on HY and Pt/HY zeolite catalysts. Journal of Catalysis 228 (2004): 100-113.

[3]   Kuznetsov, P.N. Study of n-octane hydrocracking and hydroisomerization over Pt/HY zeolites using the reactors of different configurations. Journal of Catalysis 218 (2003): 12-23.

[4]   Haensel, V. Alumina-platinum-halogen catalyst and preparation thereof. 2479109, 1949.

[5]   Yu, C.L., Ge, Q.J., Xu, H.Y., and Li, W.Z. Effects of Ce addition on the Pt-Sn/gamma-Al_2O_3 catalyst for propane dehydrogenation to propylene. Applied Catalysis A: General 315 (2006): 58-67.

[6]   Flytzani-Stephanopoulos, M., and Gates, B.C. Atomically Dispersed Supported Metal Catalysts. Annual Review of Chemical and Biomolecular Engineering, Vol 3 3 (2012): 545-574.

[7]   Thomas, J.M. The concept, reality and utility of single-site heterogeneous catalysts (SSHCs). Physical Chemistry Chemical Physics 16 (2014): 7647-7661.

[8]   Bradley, S.A., et al. Behavior of Pt Atoms on Oxide Supports During Reduction Treatments at Elevated Temperatures, Characterized by Aberration Corrected Stem Imaging. Catalysis Letters 142 (2012): 176-182.

[9]   Nilius, N., and Freund, H.-J. Activating Nonreducible Oxides via Doping. Accounts of Chemical Research 48 (2015): 1532-1539.

[10]   Yang, M., et al. A Common Single-Site Pt(II)–O(OH)x– Species Stabilized by Sodium on "Active" and "Inert" Supports Catalyzes the Water-Gas Shift Reaction. Journal of the American Chemical Society 137 (2015): 3470-3473.

[11]   Gates, B.C. Supported Metal-Clusters - Synthesis, Structure, and Catalysis. Chemical Reviews 95 (1995): 511-522.

[12]   Kwak, J.H., et al. Coordinatively Unsaturated Al^{3+} Centers as Binding Sites for Active Catalyst Phases of Platinum on γ-Al_2O_3. Science 325 (2009): 1670-1673.

[13]   Meephoka, C., Chaisuk, C., Samparnpiboon, P., and Praserthdam, P. Effect of phase composition between nano γ- and χ-Al₂O₃ on Pt/Al₂O₃ catalyst in CO oxidation. Catalysis Communications 9 (2008): 546-550.

[14]   Pansanga, K., et al. Effect of mixed γ- and χ-crystalline phases in nanocrystalline Al₂O₃ on the dispersion of cobalt on Al₂O₃. Catalysis Communications 9 (2008): 207-212.

[15]   Sun, G.X., et al. Rare earth metal modified CuO/γ-Al₂O₃ catalysts in the CO oxidation. Catalysis Communications 12 (2011): 349-352.

[16]   Jagtap, N., Umbarkar, S.B., Miquel, P., Granger, P., and Dongare, M.K. Support modification to improve the sulphur tolerance of Ag/Al2O3 for SCR of NOx with propene under lean-burn conditions. Applied Catalysis B-Environmental 90 (2009): 416-425.

[17]   Ma, Z.H., et al. Propane dehydrogenation over Al₂O₃ supported Pt nanoparticles: Effect of cerium addition. Fuel Processing Technology 128 (2014): 283-288.

[18]   Verbeek, H., and Sachtler, W.M.H. The study of the alloys of platinum and tin by chemisorption. Journal of Catalysis 42 (1976): 257-267.

[19]   Vilcocq, L., Cabiac, A., Especel, C., Lacombe, S., and Duprez, D. Study of the stability of Pt/SiO₂-Al₂O₃ catalysts in aqueous medium: Application for sorbitol transformation. Catalysis Communications 15 (2011): 18-22.

[20]   Narula, C.K., Rokosz, M., Allard, L.F., Kudla, R.J., and Chattha, M.S. Sol-gel processed silica-alumina materials for diesel engine emission reduction catalysts. Langmuir 16 (2000): 3818-3822.

[21]   Praserthdam, P., Inoue, M., Mekasuvandumrong, O., Thanakulrangsan, W., and Phatanasri, S. Effect of organic solvents on the thermal stability of porous silica-modified alumina powders prepared via one pot solvothermal synthesis. Inorganic Chemistry Communications 3 (2000): 671-676.

[22]   Engel, T., and Ertl, G., Elementary Steps in the Catalytic Oxidation of Carbon Monoxide on Platinum Metals. In *Advances in Catalysis*, D.D. Eley, H. P.; Paul, B. W., Eds. Academic Press: 1979; Vol. Volume 28, pp 1-78.

[23]   Bourane, A., and Bianchi, D. Oxidation of CO on a Pt/Al$_2$O$_3$ Catalyst: From the Surface Elementary Steps to Light-Off Tests: I. Kinetic Study of the Oxidation of the Linear CO Species. Journal of Catalysis 202 (2001): 34-44.

[24]   Guzman, J., and Gates, B.C. Catalysis by Supported Gold: Correlation between Catalytic Activity for CO Oxidation and Oxidation States of Gold. Journal of the American Chemical Society 126 (2004): 2672-2673.

[25]   Martin, D., and Duprez, D. Mobility of surface species on oxides .1. Isotopic exchange O-18(2) with O-16 of SiO2, Al2O3, ZrO2, MgO, CeO2, and CeO2-Al2O3. Activation by noble metals. Correlation with oxide basicity. Journal of Physical Chemistry 100 (1996): 9429-9438.

[26]   Vu, B.K., and Shin, E.W. Influence of Oxygen Mobility over Supported Pt Catalysts on Combustion Temperature of Coke Generated in Propane Dehydrogenation. Catalysis Letters 141 (2011): 699-704.

[27]   Sattler, J.J.H.B., Ruiz-Martinez, J., Santillan-Jimenez, E., and Weckhuysen, B.M. Catalytic Dehydrogenation of Light Alkanes on Metals and Metal Oxides. Chemical Reviews 114 (2014): 10613-10653.

[28]   Ren, Y.J., Zhang, F., Hua, W.M., Yue, Y.H., and Gao, Z. ZnO supported on high silica HZSM-5 as new catalysts for dehydrogenation of propane to propene in the presence of CO$_2$. Catalysis Today 148 (2009): 316-322.

[29]   Azzam, K.G., Jacobs, G., Shafer, W.D., and Davis, B.H. Dehydrogenation of propane over Pt/KL catalyst Investigating the role of L-zeolite structure on catalyst performance using isotope labeling. Applied Catalysis a-General 390 (2010): 264-270.

[30]   Kumar, M.S., et al. The nature of active chromium species in Cr-catalysts for dehydrogenation of propane: New insights by a comprehensive spectroscopic study. Journal of Catalysis 261 (2009): 116-128.

[31]   Jiang, F., et al. Propane Dehydrogenation over Pt/TiO$_2$–Al$_2$O$_3$ Catalysts. ACS Catalysis 5 (2015): 438-447.

[32]   Zhang, Y., et al. Comparative study of bimetallic Pt-Sn catalysts supported on different supports for propane dehydrogenation. Journal of Molecular Catalysis A: Chemical 381 (2014): 138-147.

[33]   Vu, B.K., et al. Location and structure of coke generated over Pt-Sn/Al$_2$O$_3$ in propane dehydrogenation. Journal of Industrial and Engineering Chemistry 17 (2011): 71-76.

[34]   Bocanegra, S.A., Castro, A.A., Guerrero-Ruíz, A., Scelza, O.A., and de Miguel, S.R. Characteristics of the metallic phase of Pt/Al$_2$O$_3$ and Na-doped Pt/Al$_2$O$_3$ catalysts for light paraffins dehydrogenation. Chemical Engineering Journal 118 (2006): 161-166.

[35]   Tasbihi, M., Feyzi, F., Amlashi, M.A., Abdullah, A.Z., and Mohamed, A.R. Effect of the addition of potassium and lithium in Pt–Sn/Al$_2$O$_3$ catalysts for the dehydrogenation of isobutane. Fuel Processing Technology 88 (2007): 883-889.

[36]   Horiuchi, T., et al. A novel alumina catalyst support with high thermal stability derived from silica-modified alumina aerogel. Catalysis Letters 58 (1999): 89-92.

[37]   Mardkhe, M.K., et al. Acid site properties of thermally stable, silica-doped alumina as a function of silica/alumina ratio and calcination temperature. Applied Catalysis a-General 482 (2014): 16-23.

[38]   Zhong, F.L., Zhong, Y.J., Xiao, Y.H., Cai, G.H., and Wei, K.M. Effect of Si-Doping on Thermal Stability and Diesel Oxidation Activity of Pt Supported Porous γ-Al$_2$O$_3$ Monolithic Catalyst. Catalysis Letters 141 (2011): 1828-1837.

[39]   Leydier, F., et al. Bronsted acidity of amorphous silica-alumina: The molecular rules of proton transfer. Journal of Catalysis 284 (2011): 215-229.

[40]   Valla, M., et al. Atomic Description of the Interface between Silica and Alumina in Aluminosilicates through Dynamic Nuclear Polarization Surface-Enhanced NMR Spectroscopy and First-Principles Calculations. Journal of the American Chemical Society 137 (2015): 10710-10719.

[41]   Zhang, C., et al. Alkali-Metal-Promoted Pt/TiO$_2$ Opens a More Efficient Pathway to Formaldehyde Oxidation at Ambient Temperatures. Angewandte Chemie International Edition 51 (2012): 9628-9632.

[42]   Qiao, B.T., et al. Single-atom catalysis of CO oxidation using Pt-1/FeO$_x$. Nature Chemistry 3 (2011): 634-641.

[43]   Treacy, M.M.J. Pt agglomeration and entombment in single channel zeolites: Pt/LTL. Microporous and Mesoporous Materials 28 (1999): 271-292.

[44]   Lu, J., Aydin, C., Browning, N.D., and Gates, B.C. Imaging Isolated Gold Atom Catalytic Sites in Zeolite NaY. Angewandte Chemie-International Edition 51 (2012): 5842-5846.

[45]   Azzam, K.G., Jacobs, G., Shafer, W.D., and Davis, B.H. Aromatization of hexane over Pt/KL catalyst: Role of intracrystalline diffusion on catalyst performance using isotope labeling. Journal of Catalysis 270 (2010): 242-248.

[46]   Lippens, B.C., and De Boer, J.H. Study of phase transformations during calcination of aluminum hydroxides by selected area electron diffraction. Acta Crystallographica 17 (1964): 1312-1321.

[47]   Levin, I., and Brandon, D. Metastable Alumina Polymorphs: Crystal Structures and Transition Sequences. Journal of the American Ceramic Society 81 (1998): 1995-2012.

[48]   Weitkamp, J. Zeolites and catalysis. Solid State Ionics 131 (2000): 175-188.

[49]   Corma, A. Inorganic Solid Acids and Their Use in Acid-Catalyzed Hydrocarbon Reactions. Chemical Reviews 95 (1995): 559-614.

[50]   Busca, G. Acid Catalysts in Industrial Hydrocarbon Chemistry. Chemical Reviews 107 (2007): 5366-5410.

[51]   Bartolomeu, R., et al. Particular characteristics of silver species on Ag-exchanged LTL zeolite in K and H form. Microporous and Mesoporous Materials 169 (2013): 137-147.

[52]   Koningsberger, D.C., Mojet, B.L., van Dorssen, G.E., and Ramaker, D.E. XAFS spectroscopy; fundamental principles and data analysis. Topics in Catalysis 10 (2000): 143-155.

[53]   Cant, N.W., and Angove, D.E. The origin of apparent deactivation during the oxidation of carbon monoxide over silica-supported platinum at moderate temperatures. Journal of Catalysis 97 (1986): 36-42.

[54]   Haneda, M., Watanabe, T., Kamiuchi, N., and Ozawa, M. Effect of platinum dispersion on the catalytic activity of Pt/Al_2O_3 for the oxidation of carbon monoxide and propene. Applied Catalysis B: Environmental 142 (2013): 8-14.

[55]   Manuel, I., et al. Simulation of the transient CO oxidation over Rh^0/SiO_2 and $Rh_x^+/Ce_{0.68}Zr_{0.32}O_2$ catalysts. Journal of Catalysis 224 (2004): 269-277.

[56]   Royer, S., and Duprez, D. Catalytic Oxidation of Carbon Monoxide over Transition Metal Oxides. Chemcatchem 3 (2011): 24-65.

[57]   Yang, M.-L., et al. DFT study of propane dehydrogenation on Pt catalyst: effects of step sites. Physical Chemistry Chemical Physics 13 (2011): 3257-3267.

[58]   Stijepovic, V., et al. Toward enhanced hydrogen production in a catalytic naphtha reforming process. International Journal of Hydrogen Energy 37 (2012): 11772-11784.

[59]   Vicerich, M.A., Oportus, M., Benitez, V.M., Reyes, P., and Pieck, C.L. Influence of Time and Temperature on the Regeneration of $PtReIn/Al_2O_3$ Naphtha Reforming Catalysts. Catalysis Letters 144 (2014): 1178-1187.

[60]   Mekasuwandumrong, O., Tantichuwet, P., Chaisuk, C., and Praserthdam, P. Impact of concentration and Si doping on the properties and phase transformation behavior of nanocrystalline alumina prepared via solvothermal synthesis. Materials Chemistry and Physics 107 (2008): 208-214.

[61]   Uchisawa, J., et al. Effects of the Extent of Silica Doping and the Mesopore Size of an Alumina Support on Activity as a Diesel Oxidation Catalyst. Industrial & Engineering Chemistry Research 53 (2014): 7992-7998.

[62]   Zhao, X.Y., et al. Rhodium Supported on Silica-Stabilized Alumina for Catalytic Decomposition of N_2O. Catalysis Letters 141 (2011): 128-135.

[63]   Caillot, M., et al. Synthesis of amorphous aluminosilicates by grafting: Tuning the building and final structure of the deposit by selecting the appropriate synthesis conditions. Microporous and Mesoporous Materials 185 (2014): 179-189.

[64]   Mekasuwandumrong, O., et al. Synthesis of thermally stable micro spherical chi-alumina by thermal decomposition of aluminum isopropoxide in mineral oil. Inorganic Chemistry Communications 6 (2003): 930-934.

[65]   Mekasuwandumrong, O., Kominami, H., Praserthdam, P., and Inoue, M. Synthesis of thermally stable χ-alumina by thermal decomposition of aluminum isopropoxide in toluene. Journal of the American Ceramic Society 87 (2004): 1543-1549.

[66]   Pansanga, K., Mekasuwandumrong, O., Panpranot, J., and Praserthdam, P. Synthesis of nanocrystalline alumina by thermal decomposition of aluminum

isopropoxide in 1-butanol and their applications as cobalt catalyst support. <u>Korean Journal of Chemical Engineering</u> 24 (2007): 397-402.

[67]   Chaitree, W., et al. Effect of nanocrystalline χ-Al$_2$O$_3$ structure on the catalytic behavior of Co/Al$_2$O$_3$ in CO hydrogenation. <u>Catalysis Today</u> 164 (2011): 302-307.

[68]   Abbot, J., and Guerzoni, F.N. Roles of Brønsted and Lewis sites during cracking of n-octane on H-mordenite. <u>Applied Catalysis A: General</u> 85 (1992): 173-188.

[69]   Lu, J., et al. Site-Isolated Molecular Iridium Complex Catalyst Supported in the 1-Dimensional Channels of Zeolite HSSZ-53: Characterization by Spectroscopy and Aberration-Corrected Scanning Transmission Electron Microscopy. <u>ACS Catalysis</u> 2 (2012): 1002-1012.

[70]   Nagai, Y., et al. Sintering inhibition mechanism of platinum supported on ceria-based oxide and Pt-oxide–support interaction. <u>Journal of Catalysis</u> 242 (2006): 103-109.

[71]   Ortalan, V., Uzun, A., Gates, B.C., and Browning, N.D. Direct imaging of single metal atoms and clusters in the pores of dealuminated HY zeolite. <u>Nat Nano</u> 5 (2010): 506-510.

[72]   Tauster, S.J., and Fung, S.C. Strong metal-support interactions: Occurrence among the binary oxides of groups IIA–VB. <u>Journal of Catalysis</u> 55 (1978): 29-35.

[73]   Fitzgerald, J.J., Piedra, G., Dec, S.F., Seger, M., and Maciel, G.E. Dehydration Studies of a High-Surface-Area Alumina (Pseudo-boehmite) Using Solid-State 1H and 27Al NMR. <u>Journal of the American Chemical Society</u> 119 (1997): 7832-7842.

[74]   Teichner, S.J. Recent studies in hydrogen and oxygen spillover and their impact on catalysis. <u>Applied Catalysis</u> 62 (1990): 1-10.

[75]   Prins, R. Hydrogen Spillover. Facts and Fiction. <u>Chemical Reviews</u> 112 (2012): 2714-2738.

[76]   Martin, D., and Duprez, D. Mobility of surface species on oxides .1. Isotopic exchange ^{18}O$_2$ with ^{16}O of SiO$_2$, Al$_2$O$_3$, ZrO$_2$, MgO, CeO$_2$, and CeO$_2$-Al$_2$O$_3$. Activation by noble metals. Correlation with oxide basicity. <u>Journal of Physical Chemistry</u> 100 (1996): 9429-9438.

[77]   Beaumont, S.K., Alayoglu, S., Specht, C., Kruse, N., and Somorjai, G.A. A Nanoscale Demonstration of Hydrogen Atom Spillover and Surface Diffusion Across

Silica Using the Kinetics of CO2 Methanation Catalyzed on Spatially Separate Pt and Co Nanoparticles. Nano Letters 14 (2014): 4792-4796.

[78]   Dimitrov, V., and Komatsu, T. Correlation among electronegativity, cation polarizability, optical basicity and single bond strength of simple oxides. Journal of Solid State Chemistry 196 (2012): 574-578.

[79]   Yang, X.-F., et al. Single-Atom Catalysts: A New Frontier in Heterogeneous Catalysis. Accounts of Chemical Research 46 (2013): 1740-1748.

[80]   Fierro-Gonzalez, J.C., Bhirud, V.A., and Gates, B.C. A highly active catalyst for CO oxidation at 298 K: mononuclear Auiii complexes anchored to La2O3 nanoparticles. Chemical Communications (2005): 5275-5277.

[81]   Qiao, B., et al. Highly active Au1/Co3O4 single-atom catalyst for CO oxidation at room temperature. Chinese Journal of Catalysis 36 (2015): 1505-1511.

[82]   Alayon, E.M.C., Singh, J., Nachtegaal, M., Harfouche, M., and van Bokhoven, J.A. On highly active partially oxidized platinum in carbon monoxide oxidation over supported platinum catalysts. Journal of Catalysis 263 (2009): 228-238.

[83]   Serrano-Ruiz, J.C., Sepulveda-Escribano, A., and Rodriguez-Reinoso, F. Bimetallic PtSn/C catalysts promoted by ceria: Application in the nonoxidative dehydrogenation of isobutane. Journal of Catalysis 246 (2007): 158-165.

[84]   Jentoft, R.E., Deutsch, S.E., and Gates, B.C. Low-cost, heated, and/or cooled flow-through cell for transmission x-ray absorption spectroscopy. Review of Scientific Instruments 67 (1996): 2111-2112.

[85]   Vaarkamp, M., Linders, J.C., and Koningsberger, D.C. A New Method for Parameterization of Phase-Shift and Backscattering Amplitude. Physica B 208 (1995): 159-160.

[86]   Vaarkamp, M. Obtaining reliable structural parameters from EXAFS. Catalysis Today 39 (1998): 271-279.

[87]   Rehr, J.J., Booth, C.H., Bridges, F., and Zabinsky, S.I. X-ray-absorption fine structure in embedded atoms - Reply. Physical Review B 53 (1996): 9468-9470.

[88]   Krokidis, X., et al. Theoretical Study of the Dehydration Process of Boehmite to γ-Alumina. The Journal of Physical Chemistry B 105 (2001): 5121-5130.

[89]   Khom-In, J., Praserthdam, P., Panpranot, J., and Mekasuwandumrong, O. Dehydration of methanol to dimethyl ether over nanocrystalline Al$_2$O$_3$ with mixed γ- and χ-crystalline phases. Catalysis Communications 9 (2008): 1955-1958.

[90]   Martin, D., and Duprez, D. Evaluation of the acid-base surface properties of several oxides and supported metal catalysts by means of model reactions. Journal of Molecular Catalysis a-Chemical 118 (1997): 113-128.

[91]   Anderson, J.A., Mordente, M.G.V., and Rochester, C.H. Effects of oxidation-reduction treatments of Pt/Al$_2$O$_3$ on catalytic activity and selectivity for hexane reforming. Journal of the Chemical Society, Faraday Transactions 1: Physical Chemistry in Condensed Phases 85 (1989): 2991-2998.

[92]   Jiang, N., Rao, K.S.R., Jin, M.-J., and Park, S.-E. Effect of hydrogen spillover in decalin dehydrogenation over supported Pt catalysts. Applied Catalysis A: General 425–426 (2012): 62-67.

[93]   Hayashi, K., Horiuchi, T., Suzuki, K., and Mori, T. Sintering behavior of Pt metal particles supported on silica-coated alumina surface. Catalysis Letters 78 (2002): 43-47.

[94]   Wintterlin, J., Völkening, S., Janssens, T.V.W., Zambelli, T., and Ertl, G. Atomic and Macroscopic Reaction Rates of a Surface-Catalyzed Reaction. Science 278 (1997): 1931-1934.

[95]   Morajkar, P.P., and Fernandes, J.B. A new facile method to synthesize mesoporous γ-Al2O3 of high surface area and catalytic activity. Catalysis Communications 11 (2010): 414-418.

[96]   Magendie, G., et al. Toward a better understanding of residue hydroconversion catalysts using NiMo catalysts supported over silica grafted Al$_2$O$_3$. Applied Catalysis a-General 468 (2013): 216-229.

[97]   Beguin, B., Garbowski, E., and Primet, M. Stabilization of alumina toward thermal sintering by silicon addition. Journal of Catalysis 127 (1991): 595-604.

[98]   Daniell, W., et al. Enhanced surface acidity in mixed alumina-silicas: a low-temperature FTIR study. Applied Catalysis a-General 196 (2000): 247-260.

[99]   Narayanan, S., Sultana, A., Le, Q.T., and Auroux, A. A comparative and multitechnical approach to the acid character of templated and non-templated ZSM-5 zeolites. Applied Catalysis a-General 168 (1998): 373-384.

[100] Park, C.-M., et al. Characterizations and electrochemical behaviors of disproportionated SiO and its composite for rechargeable Li-ion batteries. Journal of Materials Chemistry 20 (2010): 4854-4860.

[101] Liu, X., et al. Improved catalytic performance in propane dehydrogenation of PtSn/gamma-Al$_2$O$_3$ catalysts by doping indium. Chemical Engineering Journal 247 (2014): 183-192.

[102] Lieske, H., Lietz, G., Spindler, H., and Völter, J. Reactions of platinum in oxygen- and hydrogen-treated Pt/γ-Al$_2$O$_3$ catalysts: I. Temperature-programmed reduction, adsorption, and redispersion of platinum. Journal of Catalysis 81 (1983): 8-16.

[103] Moses-DeBusk, M., et al. CO Oxidation on Supported Single Pt Atoms: Experimental and ab Initio Density Functional Studies of CO Interaction with Pt Atom on theta-Al$_2$O$_3$(010) Surface. Journal of the American Chemical Society 135 (2013): 12634-12645.

[104] Hippe, C., Lamber, R., SchulzEkloff, G., and Schubert, U. Influence of the strong metal-support interaction on the CO chemisorption at a Pt/SiO2 catalyst. Catalysis Letters 43 (1997): 195-199.

[105] Lamber, R., and Romanowski, W. Dispersion changes of platinum supported on silica glass during thermal treatment in oxygen and hydrogen atmospheres. Journal of Catalysis 105 (1987): 213-226.

[106] Karakaya, C., and Deutschmann, O. A simple method for CO chemisorption studies under continuous flow: Adsorption and desorption behavior of Pt/Al2O3 catalysts. Applied Catalysis A: General 445–446 (2012): 221-230.

[107] Tanksale, A., Beltramini, J.N., Dumesic, J.A., and Lu, G.Q. Effect of Pt and Pd promoter on Ni supported catalysts—A TPR/TPO/TPD and microcalorimetry study. Journal of Catalysis 258 (2008): 366-377.

[108] Gould, T.D., et al. Controlling Nanoscale Properties of Supported Platinum Catalysts through Atomic Layer Deposition. ACS Catalysis 5 (2015): 1344-1352.

[109] Altman, E.I., and Gorte, R.J. The desorption of CO from small Pt particles on Al$_2$O$_3$. Surface Science 172 (1986): 71-80.

[110] Miura, H., and Gonzalez, R.D. Temperature-programmed desorption and temperature-programmed reaction studies of carbon monoxide over well-

characterized silica-supported platinum-ruthenium bimetallic clusters. The Journal of Physical Chemistry 86 (1982): 1577-1582.

[111] Tanaka, H., et al. Preferential CO oxidation in hydrogen-rich stream over Pt catalysts modified with alkali metals: Part II. Catalyst characterization and role of alkali metals. Applied Catalysis A: General 343 (2008): 125-133.

[112] Marino, F., Descorme, C., and Duprez, D. Noble metal catalysts for the preferential oxidation of carbon monoxide in the presence of hydrogen (PROX). Applied Catalysis B-Environmental 54 (2004): 59-66.

[113] Widmann, D., and Behm, R.J. Activation of Molecular Oxygen and the Nature of the Active Oxygen Species for CO Oxidation on Oxide Supported Au Catalysts. Accounts of Chemical Research 47 (2014): 740-749.

[114] Ozawa, M., Okouchi, T., and Haneda, M. Three way catalytic activity of thermally degenerated Pt/Al_2O_3 and Pt/CeO_2-ZrO_2 modified Al_2O_3 model catalysts. Catalysis Today 242 (2015): 329-337.

[115] Boudart, M., and Rumpf, F. The catalytic oxidation of CO and structure insensitivity. Reaction Kinetics and Catalysis Letters 35 (1987): 95-105.

[116] Lee, C.H., and Chen, Y.W. Effect of basic additives on Pt/Al_2O_3 for CO and propylene oxidation under oxygen-deficient conditions. Industrial & Engineering Chemistry Research 36 (1997): 1498-1506.

[117] Minemura, Y., Kuriyama, M., Ito, S., Tomishige, K., and Kunimori, K. Additive effect of alkali metal ions on preferential CO oxidation over Pt/Al_2O_3. Catalysis Communications 7 (2006): 623-626.

[118] Virnovskaia, A., Morandi, S., Rytter, E., Ghiotti, G., and Olsbye, U. Characterization of Pt,Sn/Mg(Al)O catalysts for light alkane dehydrogenation by FT-IR Spectroscopy and catalytic measurements. Journal of Physical Chemistry C 111 (2007): 14732-14742.

[119] Nagaraja, B.M., Shin, C.H., and Jung, K.D. Selective and stable bimetallic $PtSn/theta$-Al_2O_3 catalyst for dehydrogenation of n-butane to n-butenes. Applied Catalysis a-General 467 (2013): 211-223.

[120] Kumar, M.S., Chen, D., Walmsley, J.C., and Holmen, A. Dehydrogenation of propane over Pt-SBA-15: Effect of Pt particle size. Catalysis Communications 9 (2008): 747-750.

[121] Castano, P., et al. Deactivating Species Deposited on Pt-Pd Catalysts in the Hydrocracking of Light-Cycle Oil. Energy & Fuels 26 (2012): 1509-1519.

[122] Bastl, Z., et al. NaX-encaged Pt carbonyls: reversible substitution of CO ligands by oxygen and ammonia. Evidence for a conservation of the polynuclear Pt skeleton. Physical Chemistry Chemical Physics 2 (2000): 3099-3104.

[123] Miessner, H., et al. The formation of a well defined rhodium dicarbonyl in highly dealuminated rhodium-exchanged zeolite Y by interaction with CO. Journal of the Chemical Society, Faraday Transactions 1: Physical Chemistry in Condensed Phases 85 (1989): 2113-2126.

[124] Dyer, A., Amini, S., Enamy, H., Elnaggar, H.A., and Anderson, M.W. Cation-Exchange in Synthetic Zeolite-L - the Exchange of Hydronium and Ammonium-Ions by Alkali-Metal and Alkaline-Earth Cations. Zeolites 13 (1993): 281-290.

[125] Miller, J.T., Schreier, M., Kropf, A.J., and Regalbuto, J.R. A fundamental study of platinum tetraammine impregnation of silica: 2. The effect of method of preparation, loading, and calcination temperature on (reduced) particle size. Journal of Catalysis 225 (2004): 203-212.

[126] Munozpaez, A., and Koningsberger, D.C. Decomposition of the Precursor [Pf(Nh3)(3)](Oh)(2), Genesis and Structure of the Metal-Support Interface of Alumina-Supported Platinum Particles - a Structural Study Using Tpr, Ms, and Xafs Spectroscopy. Journal of Physical Chemistry 99 (1995): 4193-4204.

[127] Hall, M.D., et al. Quantitative measurement of the reduction of platinum(IV) complexes using X-ray absorption near-edge spectroscopy (XANES). Metallomics 4 (2012): 568-575.

[128] Chen, S.M., et al. An X-ray absorption spectroscopic investigation of the geometry of Pt(IV) in H_2PtCl_6 ammonia solution. Journal of Molecular Structure 1041 (2013): 39-43.

[129] Takao, K., Takao, S., Scheinost, A.C., Bernhard, G., and Hennig, C. In situ spectroelectrochemical investigation of Pt(II/IV) oxidation in aqueous solution using X-ray absorption spectroscopy. Inorganica Chimica Acta 363 (2010): 802-806.

[130] Rodrigues, A.C.C., and Monteiro, J.L.F. Thermal decomposition of the $[Pt(NH_3)_4]^{2+}$ stop complex in NaX zeolite: Effect of calcination procedure. Journal of Thermal Analysis and Calorimetry 83 (2006): 451-455.

[131] Efremenko, I., Poverenov, E., Martin, J.M.L., and Milstein, D. DFT Study of the Structure and Reactivity of the Terminal Pt(IV)-Oxo Complex Bearing No Electron-Withdrawing Ligands. Journal of the American Chemical Society 132 (2010): 14886-14900.

[132] Tzou, M.S., Teo, B.K., and Sachtler, W.M.H. Formation of Pt Particles in Y-Type Zeolites - the Influence of Coexchanged Metal-Cations. Journal of Catalysis 113 (1988): 220-235.

[133] Akdogan, Y., et al. Platinum species in the pores of NaX, NaY and NaA zeolites studied using EPR, XAS and FTIR spectroscopies. Physical Chemistry Chemical Physics 10 (2008): 2952-2963.

[134] Chakarova, K., Mihaylov, M., and Hadjiivanov, K. FTIR spectroscopic study of CO adsorption on Pt-H-ZSM-5. Microporous and Mesoporous Materials 81 (2005): 305-312.

[135] Regali, F., Liotta, L.F., Venezia, A.M., Boutonnet, M., and Jaras, S. Hydroconversion of n-hexadecane on Pt/silica-alumina catalysts: Effect of metal loading and support acidity on bifunctional and hydrogenolytic activity. Applied Catalysis a-General 469 (2014): 328-339.

[136] Kim, M.Y., et al. Effect of Al content on hydrocracking of n-paraffin over Pt/SiO_2-Al_2O_3. Catalysis Communications 26 (2012): 78-82.

[137] Yoshida, H., Yazawa, Y., and Hattori, T. Effects of support and additive on oxidation state and activity of Pt catalyst in propane combustion. Catalysis Today 87 (2003): 19-28.

[138] Shibata, J., et al. Factors controlling activity and selectivity for SCR of NO by hydrogen over supported platinum catalysts. Journal of Physical Chemistry B 108 (2004): 18327-18335.

[139] van den Brink, R.W., Krzan, M., Feijen-Jeurissen, M.M.R., Louw, R., and Mulder, P. The role of the support and dispersion in the catalytic combustion of chlorobenzene on noble metal based catalysts. Applied Catalysis B-Environmental 24 (2000): 255-264.

[140] Shabaker, J.W., Huber, G.W., Davda, R.R., Cortright, R.D., and Dumesic, J.A. Aqueous-phase reforming of ethylene glycol over supported platinum catalysts. Catalysis Letters 88 (2003): 1-8.

[141] Liu, C.Y., Shao, Z.F., Xiao, Z.H., Williams, C.T., and Liang, C.H. Hydrodeoxygenation of Benzofuran over Silica-Alumina-Supported Pt, Pd, and Pt-Pd Catalysts. Energy & Fuels 26 (2012): 4205-4211.

[142] Kim, K.B., Kim, Y.H., Song, K.S., and Park, E.D. PROPANE COMBUSTION OVER Pt CATALYSTS SUPPORTED ON ZEOLITES. Reviews on Advanced Materials Science 28 (2011): 35-39.

[143] Garetto, T.F., Rincon, E., and Apesteguia, C.R. Deep oxidation of propane on Pt-supported catalysts: drastic turnover rate enhancement using zeolite supports. Applied Catalysis B-Environmental 48 (2004): 167-174.

[144] Primet, M. Electronic transfer and ligand effects in the infrared spectra of adsorbed carbon monoxide. Journal of Catalysis 88 (1984): 273-282.

[145] Li, G.-J., Fujimoto, T., Fukuoka, A., and Ichikawa, M. EXAFS and fourier transform IR characterization of platinum carbonyl clusters $[Pt_3(CO)_6]^{2-(n= 3, 4)}$ encapsulated in nay zeolites and their effective catalysis in the CO + NO reaction. Journal of the Chemical Society, Chemical Communications (1991): 1337-1339.

[146] Klier, K. Transition-metal ions in zeolites: the perfect surface sites. Langmuir 4 (1988): 13-25.

[147] Kappers, M.J., and Maas, J.H. Correlation between CO frequency and Pt coordination number. A DRIFT study on supported Pt catalysts. Catalysis Letters 10 (1991): 365-373.

[148] Besoukhanova, C., Guidot, J., Barthomeuf, D., Breysse, M., and Bernard, J.R. Platinum-zeolite interactions in alkaline L zeolites. Correlations between catalytic activity and platinum state. Journal of the Chemical Society, Faraday Transactions 1: Physical Chemistry in Condensed Phases 77 (1981): 1595-1604.

[149] Klunker, C., Balden, M., Lehwald, S., and Daum, W. CO stretching vibrations on Pt(111) and Pt(110) studied by sum-frequency generation. Surface Science 360 (1996): 104-111.

[150] Yoshinobu, J., and Kawai, M. Initial adsorption sites of CO on Pt(111) and Ni(100) at low temperature. Surface Science 363 (1996): 105-111.

[151] Haaland, D.M. Infrared studies of CO adsorbed on Pt/Al_2O_3: Evidence for CO bonded in 3-fold coordination. Surface Science 185 (1987): 1-14.

[152] Barth, R., Pitchai, R., Anderson, R.L., and Verykios, X.E. Thermal desorption-infrared study of carbon monoxide adsorption by alumina-supported platinum. Journal of Catalysis 116 (1989): 61-70.

[153] Bischoff, H., Jaeger, N.I., Schulz-Ekloff, G., and Kubelkova, L. Interaction of CO with platinum species in zeolites. Evidence for platinum carbonyls in partially reduced zeolite PtNaX. Journal of Molecular Catalysis 80 (1993): 95-103.

[154] Kustov, L., Ostgard, D., and Sachtler, W.H. IR spectroscopic study of Pt/Kl zeolites using adsorption of CO as a molecular probe. Catalysis Letters 9 (1991): 121-126.

[155] Mergler, Y.J., vanAalst, A., vanDelft, J., and Nieuwenhuys, B.E. CO oxidation over promoted Pt catalysts. Applied Catalysis B-Environmental 10 (1996): 245-261.

[156] Gracia, F.J., Bollmann, L., Wolf, E.E., Miller, J.T., and Kropf, A.J. In situ FTIR, EXAFS, and activity studies of the effect of crystallite size on silica-supported Pt oxidation catalysts. Journal of Catalysis 220 (2003): 382-391.

[157] Bamwenda, G.R., Tsubota, S., Nakamura, T., and Haruta, M. The influence of the preparation methods on the catalytic activity of platinum and gold supported on TiO_2 for CO oxidation. Catalysis Letters 44 (1997): 83-87.

APPENDICES

CALCULATION OF THE CRYSTALLITE SIZE

Calculation of the crystallite size by using the Debye-Scherrer equation

The crystallite size was calculated from the width at half of height (FWHM) of main diffraction peak of the XRD pattern by using the Debye-Scherrer equation.

$$D = \frac{K\lambda}{\beta cos\theta}$$

where D = Crystallite size, A°

K = Cyrstallite-shape factor or Scherrer constant depending on shape of

crystal (= 0.9 for FWHM of spherical crystals with cubic symmetry)

λ = X-ray wavelength, (=1.5418 A° for CuK_α)

θ = Observed peak angle, degree

β = X-ray diffraction broadening, radian

The X-ray diffraction broadening (β) is the pure full-width-half-max of powder diffraction peak free from all broadening because of the experimental equipment or diffractometer. For a standard sample, α-Alumina is used as a standard sample to observe the instrumental broadening due to its crystallite size larger than 2000 A°. The X-ray diffraction broadening (β) can be determined by using the Warren's formula.

According to Warren's formula:

$$\beta = \sqrt{B_M^2 - B_S^2}$$

Where B_M = Measured peak width at half of peak height, radian

B_S = Corresponding full-width-half-max of the standard material

(i.e., α-Alumina), radian

Example: Calculation of the crystallite size of γ-Al_2O_3

The major peak of γ-Al_2O_3 was observed at 2θ = 66.82°.

Full-width-half-max of diffraction peak at 66.82°   = 2.26°

$$= \frac{(2\pi \times 3.76°)}{360}$$

$$= 0.0197 \text{ radian}$$

Corresponding FWHM of α-alumina of diffraction peak at 66.94° = 0.00571 radian

$$\beta = \sqrt{B_M^2 - B_S^2}$$

$$= \sqrt{(0.0197)^2 - (0.00571)^2}$$

$$= 0.0189 \text{ radian}$$

Thus,

β = 0.0189 radian

2θ = 66.82° ➔ θ = 33.41°

λ = 1.5418 A° for CuK$_\alpha$

Crystallite size, $D = \dfrac{K\lambda}{\beta cos\theta}$

$$= \frac{0.9 \times 1.5418}{0.0189 \times cos33.41°}$$

$$= 88.03 \text{ A°}$$

$$= 8.8 \text{ nm}$$
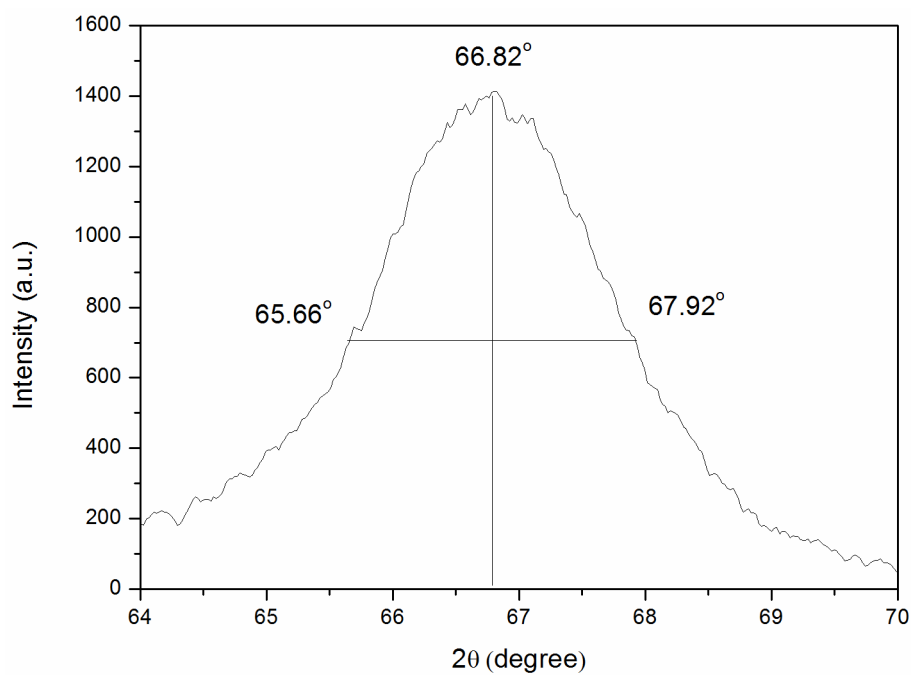
Figure A.1 The XRD main peak of γ-Al_2O_3 for calculation of crystallite size of γ-Al_2O_3.
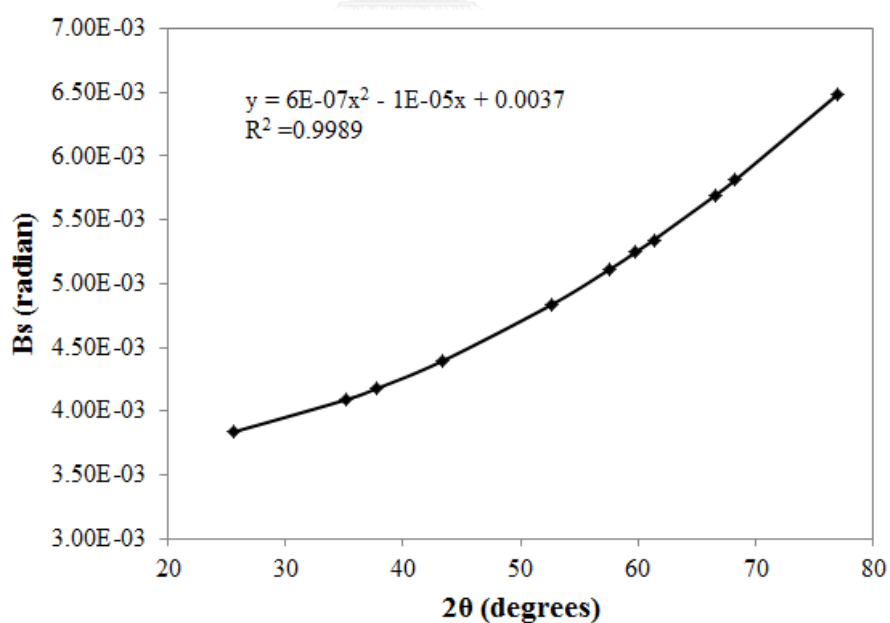
Figure A.2 The plot demonstrating the value of line broadening because of the equipment (Data were obtained by using α-alumina as a reference material).

APPENDIX B

CALCULATION FOR PLATINUM ACTIVE SITES AND DISPERSION

The determination of the metal active sites and metal dispersion of the catalyst samples by using CO-chemisorption technique is shown as follows:

Calculation of metal active sites

Volume of CO adsorbed on catalyst, $V_{ads} = \frac{V_{inj}}{g_{cat}} \times \sum_1^{sat}[1 - (\frac{A_i}{A_f})]$ L of CO/g_{cat}

where V_{inj} = volume of CO injected portion

g_{cat} = weight of catalyst used, g

A_i = integral area of CO peak after adsorption, unit

A_f = average integral area of saturated-CO peak, unit

Mole of CO adsorbed on catalyst $= \frac{P \times V_{ads}}{R \times T}$ mol of CO/g_{cat}

where P   = pressure at CO adsorbed = 1 atm

R   = gas constant = 0.08206 L·atm/(mol·K)

T   = temperature at CO adsorbed = 30 °C

Molecules of CO adsorbed on catalyst $= \frac{P \times V_{ads}}{R \times T} \times 6.02 \times 10^{23}$ molecule CO/g_{cat}

Metal active sites $= \frac{P \times V_{ads} \times S_f}{R \times T} \times 6.02 \times 10^{23}$ molecule CO/g_{cat}

where S_f = stoichiometry factor of CO adsorbed on Pt

Calculation of metal dispersion

Metal dispersion (%) $= 100 \times \frac{amount\ of\ Pt\ determined\ by\ adsorbed-CO}{amount\ of\ Pt\ loading}$

Figure C.1 SEM images of xSiAl supports at 20,000 magnification: (a) 0, (b) 0.6, (c) 1.2, (d) 5.6, and (e) 12.4 wt% SiO_2.
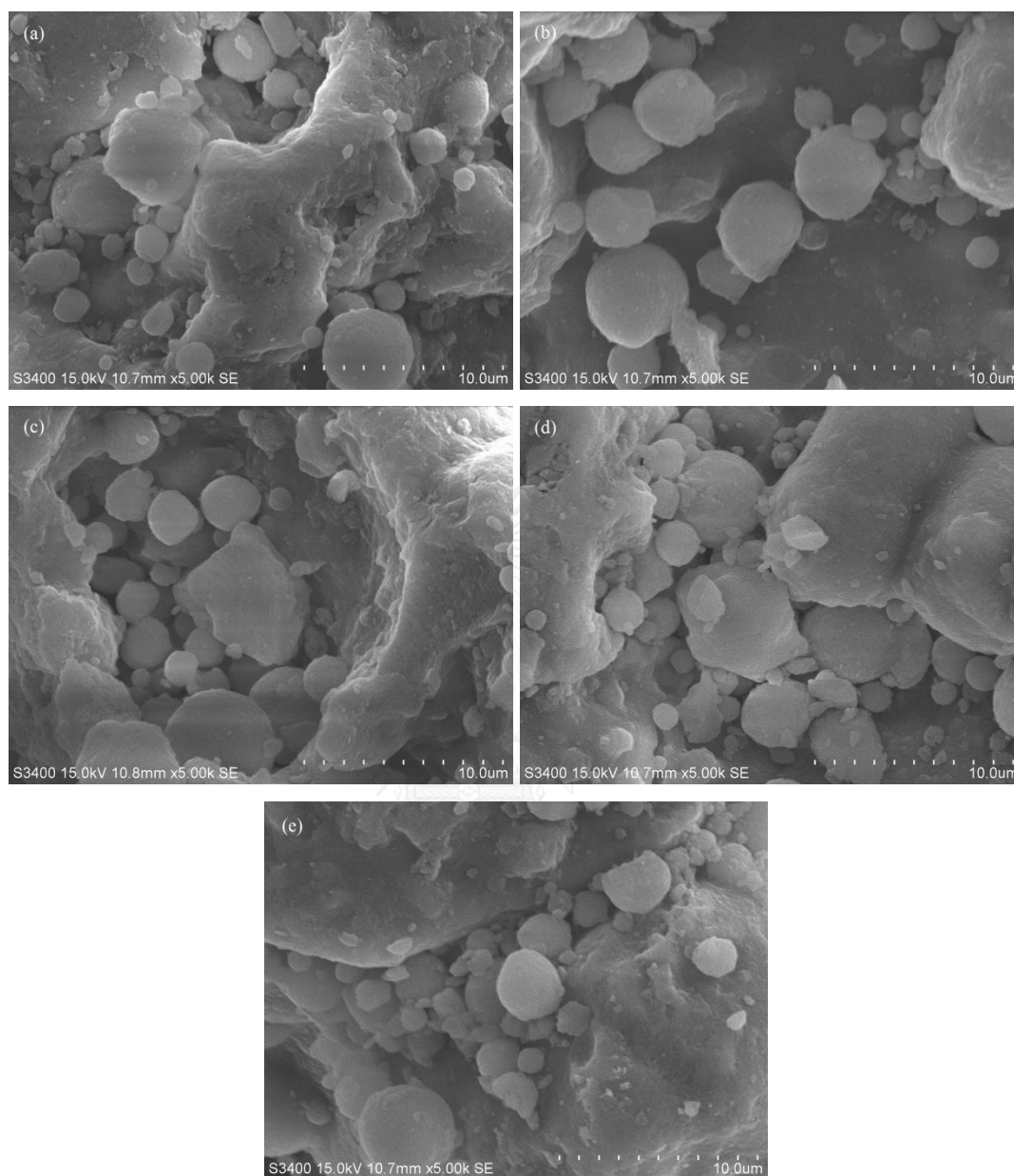
Figure C.2 SEM images of xSiAl supports at 5,000 magnification: (a) 0, (b) 0.6, (c) 1.2, (d) 5.6, and (e) 12.4 wt% SiO_2.
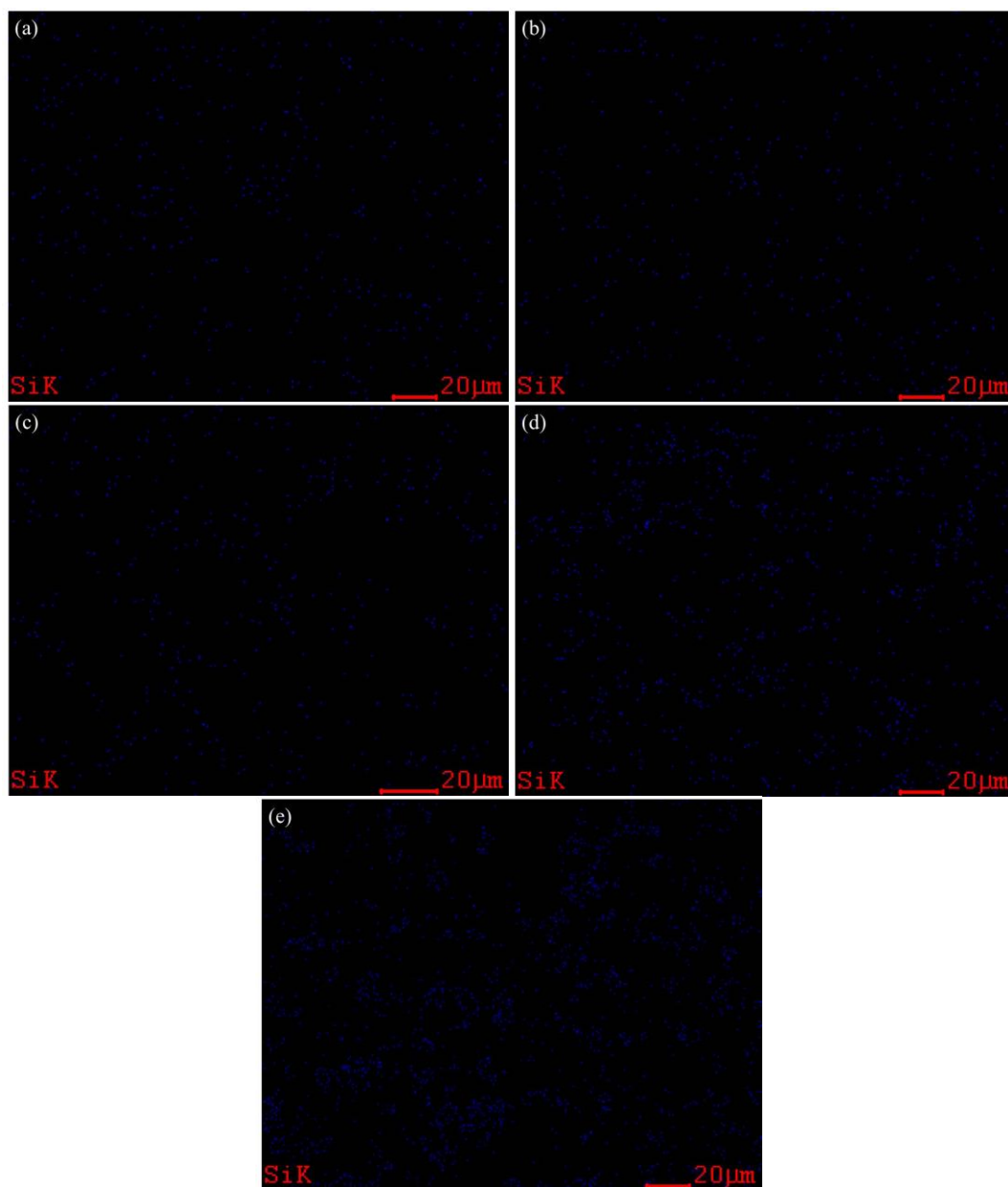
Figure C.3 EDX maps for Si of xSiAl supports: (a) 0, (b) 0.6, (c) 1.2, (d) 5.6, and (e) 12.4 wt% SiO_2.

Table D.1 Comparison of aluminosilicate supported Pt catalyst: CO uptake and Pt dispersion.

Catalyst	Support supplier	SiO$_2$ contents (wt.%)	Pt contents (wt.%)	Calcination (°C)	CO uptake (μmol/g)	Pt dispersion[b] (%)	Reaction	References
Pt/xSiO$_2$/Al$_2$O$_3$	Detail is in experimental*	0	0.3	500	8.0	52	CO oxidation	This work
		0.6			14.5	95		
		1.2			11.5	75		
		5.6			8.3	54		
		12.4			6.9	45		
Pt/Siral1	Sasol	1	0.33	500	-	80[c]	n-hexadecane hydrogenolysis	[135]
Pt/Siral40		40			-	91[c]		
Pt/SiO$_2$-Al$_2$O$_3$	Co-precipitation*	0.6	0.5	600	-	60.2	Diesel oxidation	[38]
		2.0			-	67.6		
		4.0			-	62.1		
Pt/Si$_{0.1}$Al$_{0.9}$O$_x$	Co-precipitation*	11.5[a]	1.07	500	17.7	32	n-paraffin hydrocracking	[136]
Pt/Si$_{0.2}$Al$_{0.8}$O$_x$		23[a]	1.04	500	15.4	29		
Pt/SiO$_2$-Al$_2$O$_3$	JRC-SAL-2	86[a]	5	400	-	40	C$_3$H$_8$ combustion	[137]
Pt/SiO$_2$-Al$_2$O$_3$	JRC-SAL-2	86[a]	1	500	-	13[d]	SCR of NO	[138]
Pt/SiO$_2$-Al$_2$O$_3$	Akzo Nobel	88	2	600	-	23	Chlorobenzene combustion	[139]

Catalyst	Support supplier	SiO$_2$ contents (wt.%)	Pt contents (wt.%)	Calcination (°C)	CO uptake (µmol/g)	Pt dispersion[b] (%)	Reaction	References
Pt/SiO$_2$-Al$_2$O$_3$	Grace, MS-25	75	0.79	260	13.7	34	Ethylene glycol reforming	[140]
Pt/SiO$_2$-Al$_2$O$_3$	Not available	20[a]	0.5	300	3.9	30.4	Benzofuran hydro-deoxygenation	[141]
Pt/NaY	Tosoh	77[a]	0.84	500	6.8	16	C$_3$H$_8$ combustion	[142]
Pt/HY	Zeolyst	75[a]	0.84		7.8	18		
Pt/H-ferrierite	Zeolyst	92[a]	0.86		12.4	28		
Pt/KL	Tosoh	78[a]	0.44		-	71[c]		[143]
Pt/HY	UOP-Y 54	74[a]	0.32	300	-	40[c]	C$_3$H$_8$ combustion	
Pt/ZSM5	Zeocat Pentasil PZ-2/54	96[a]	0.36		-	30[c]		

* Synthesis method

[a] wt.% was obtained by calculating from Si/Al ratio

[b] Pt dispersion was calculated by CO chemisorption

[c] Pt dispersion was calculated by H$_2$ chemisorption

[d] Pt dispersion was calculated by CO-H$_2$ titration

APPENDIX E

PHYSICAL PROPERTIES OF KLTL ZEOLITE

Table E.1 Elemental analysis of KLTL Zeolite (provided by the supplier, UOP).

Component	Content (wt%)
Al_2O_3	18.0
SiO_2	64.6
K_2O	17.4
Na_2O	0.2
Si/Al atomic ratio	3.05
K/Al atomic ratio	1.05
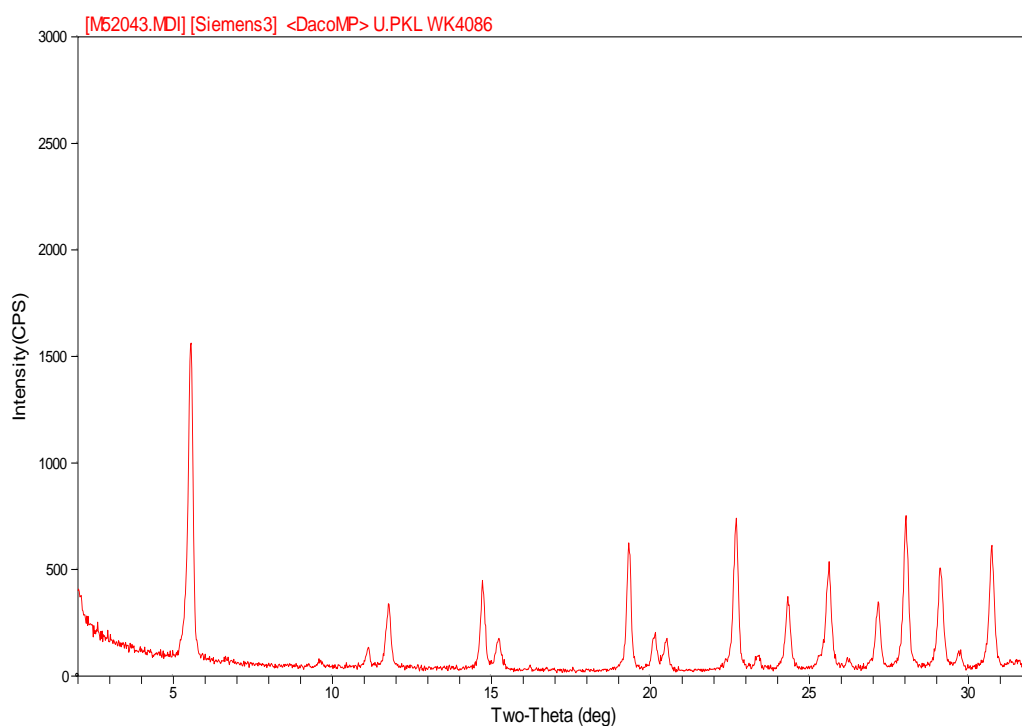
Figure E.1 XRD pattern of KLTL zeolite.
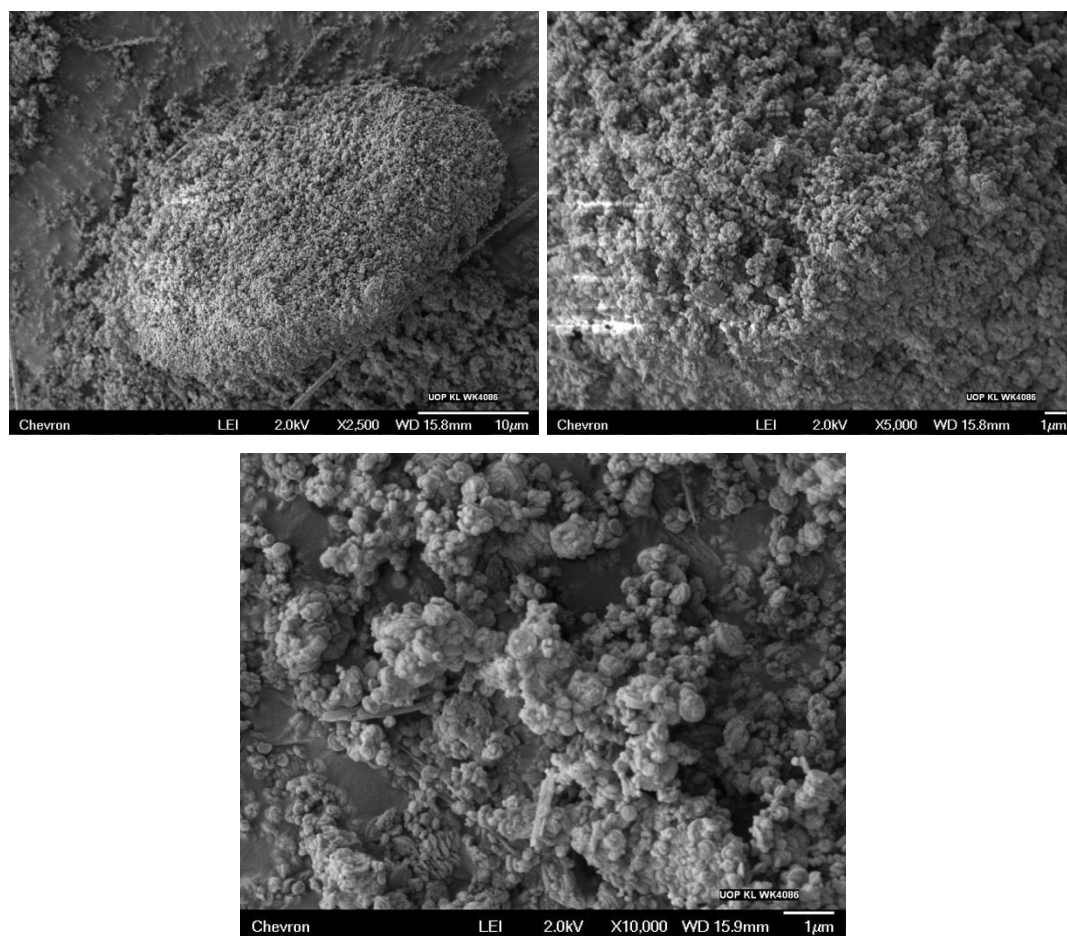
Figure E.2 SEM images at different magnification of KLTL zeolite.

APPENDIX F

SUPPLEMENTARY INFORMATION OF MICROSCOPY

Platinum atom location determination

All electron microscopy images were analyzed using Digital Micrograph software. For each sample, more than 70 individual atomic sites were chosen for calculation. The data were taken from 1 or more images in order to obtain a statistically significant number of data points. The approximate error for each calculation is $\pm$ 2.1%.

The estimated error is calculated to be the average of the standard deviations of the three different sites. As shown in the Table below, the standard deviation for each site was calculated over 4 individual micrographs of the same sample.

Table F.1 Statistics of single-site Pt atoms in various channels.

	% of Pt atoms in D sites	% of Pt atoms in A/B sites	% of Pt atoms in C/E sites
Micrograph 1	56.4	23.1	20.5
Micrograph 2	54.5	27.3	18.2
Micrograph 3	60	20	20
Micrograph 4	58.3	25	16.7
Average	57.3	23.85	18.85
Standard Deviation	2.0	2.7	1.5
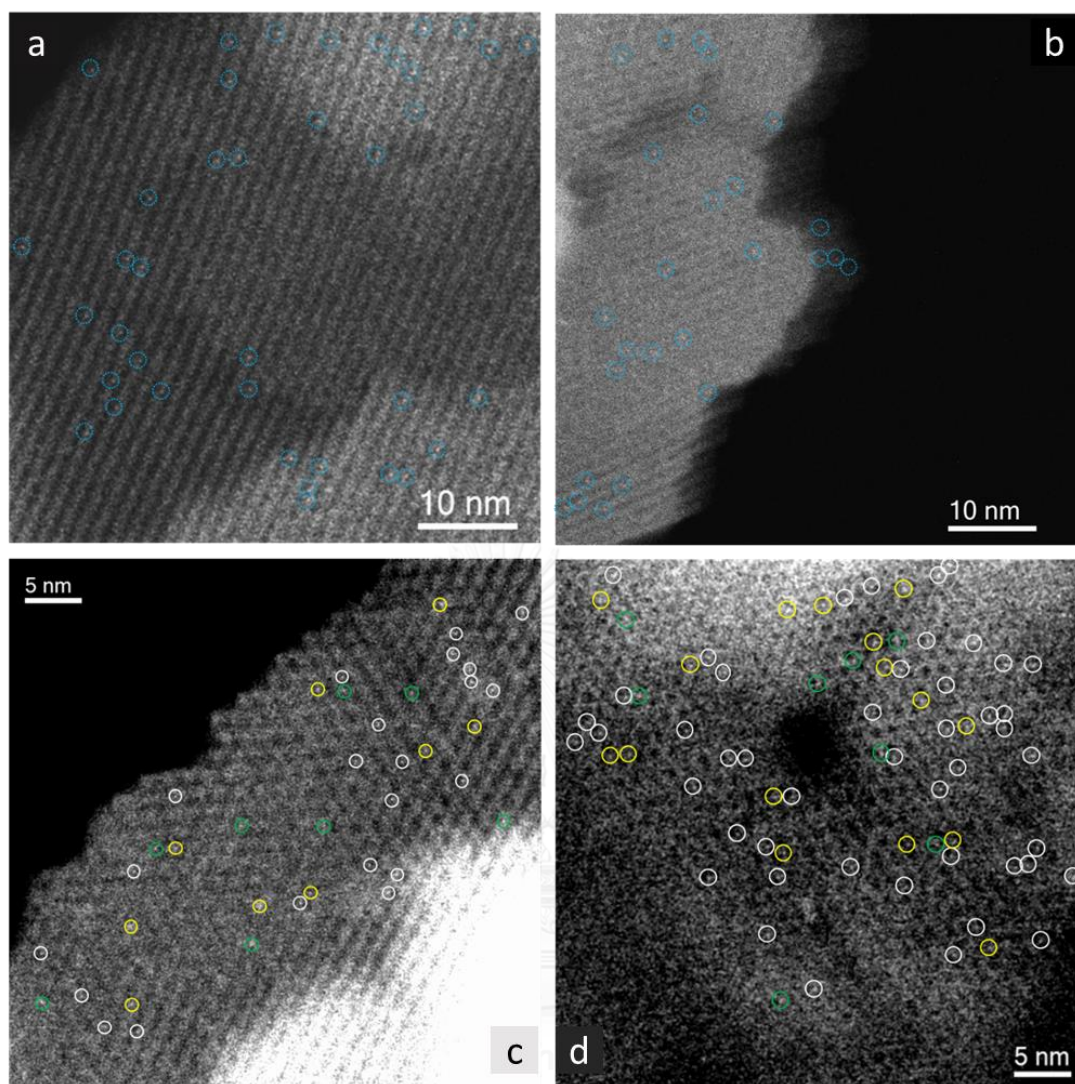
Figure F.1 STEM images of site-isolated Pt atoms in KLTL zeolite in the as-prepared samples are shown in (a) and (c), in the oxidized samples are shown in (b) and (d). White circles indicate species in the D sites. Yellow circles represent species in the A and B sites. Green circles represent species in the C and E sites. Note that (c) and (d) are view in the [110] direction, which has minimum zeolite framework overlaps and thus are ideal for determination of the locations of the Pt species. Crystallographic models superimposed on the STEM images help to determine the locations of the Pt atoms as described elsewhere [71] and as illustrated in **Figure 5.20**.
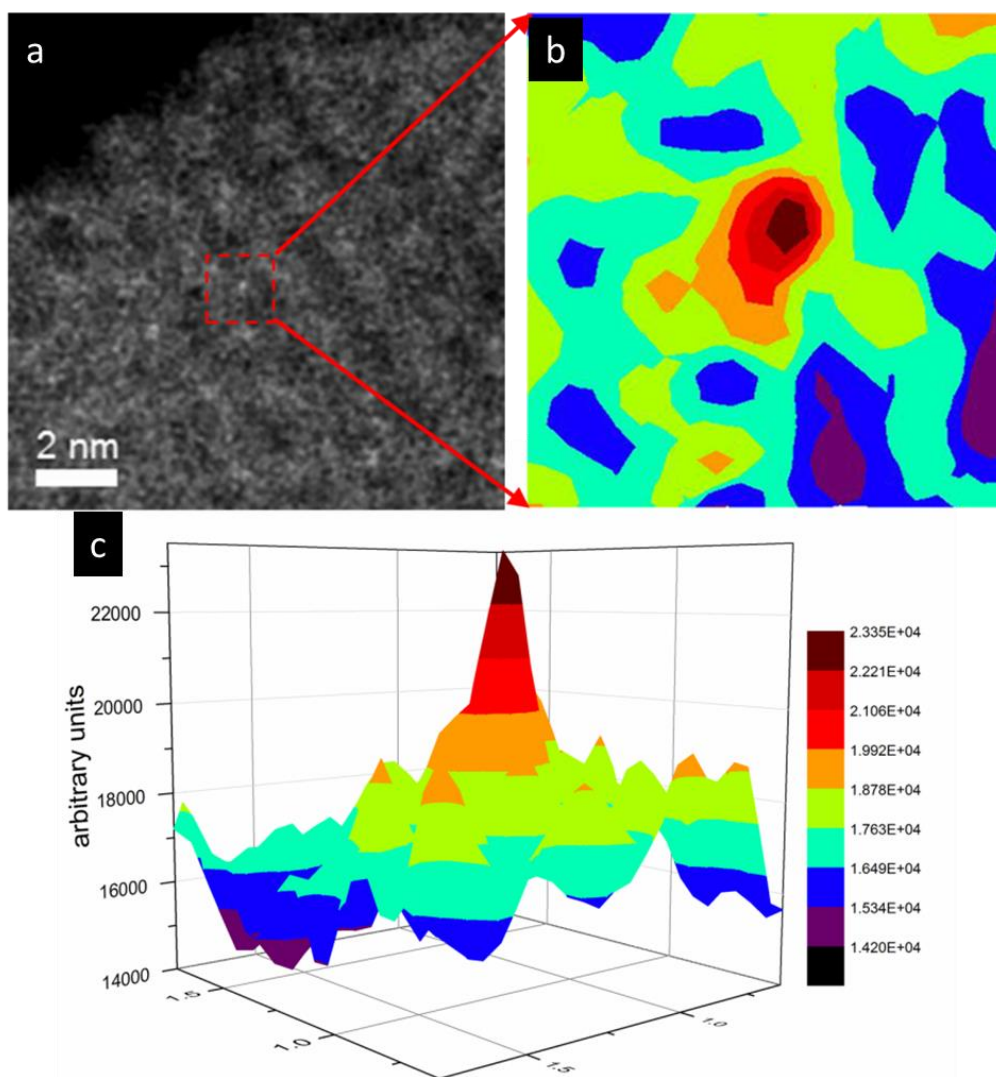
Figure F.2 a) STEM images showing site-isolated Pt atoms in the as-prepared KLTL zeolite sample. b) Intensity surface plot of the area in the red dashed regions in (a). c) Three-dimensional Intensity surface plot of (B). White feature captured in the red dashed region is the platinum species (at D sites).
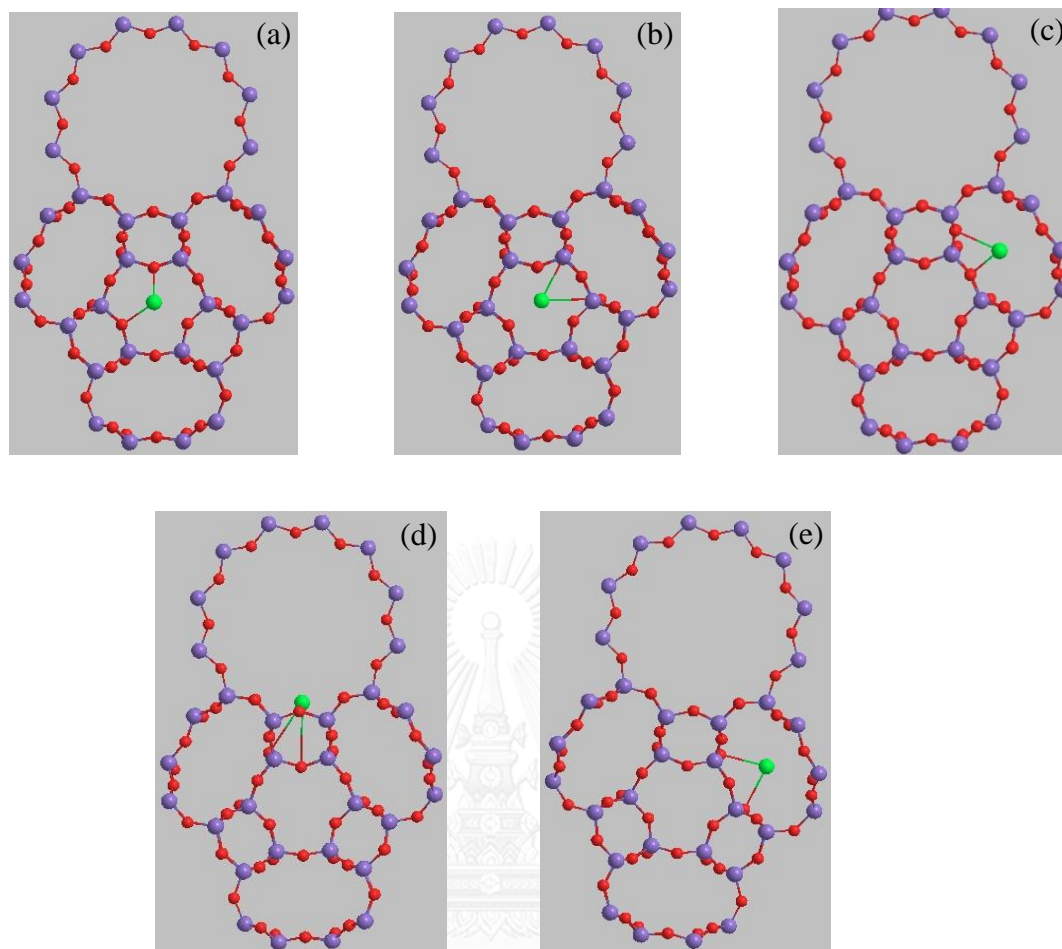
Figure F.3 ChemDraw 3D models of zeolite LTL incorporating oxidized PtO_x complexes located in different channels

(a) in the 6-membered ring in the A position, (b) in the 6-membered ring in the B position, (c) in the 8-membered ring in the C location, (d) in the 12-membered in the D position and (e) in the 8-membered ring in the E position. Locations of the Pt atoms are only relative locations to show the 5 unique bonding sites as described elsewhere [51, 124]. Pt-O bond distances as determined by EXAFS were also taken into account when modeling locations of Pt atoms. Color scheme: oxygen (red), T-site silicon/aluminum (purple), platinum (green).

APPENDIX G
FITTING DETAILS OF EXAFS
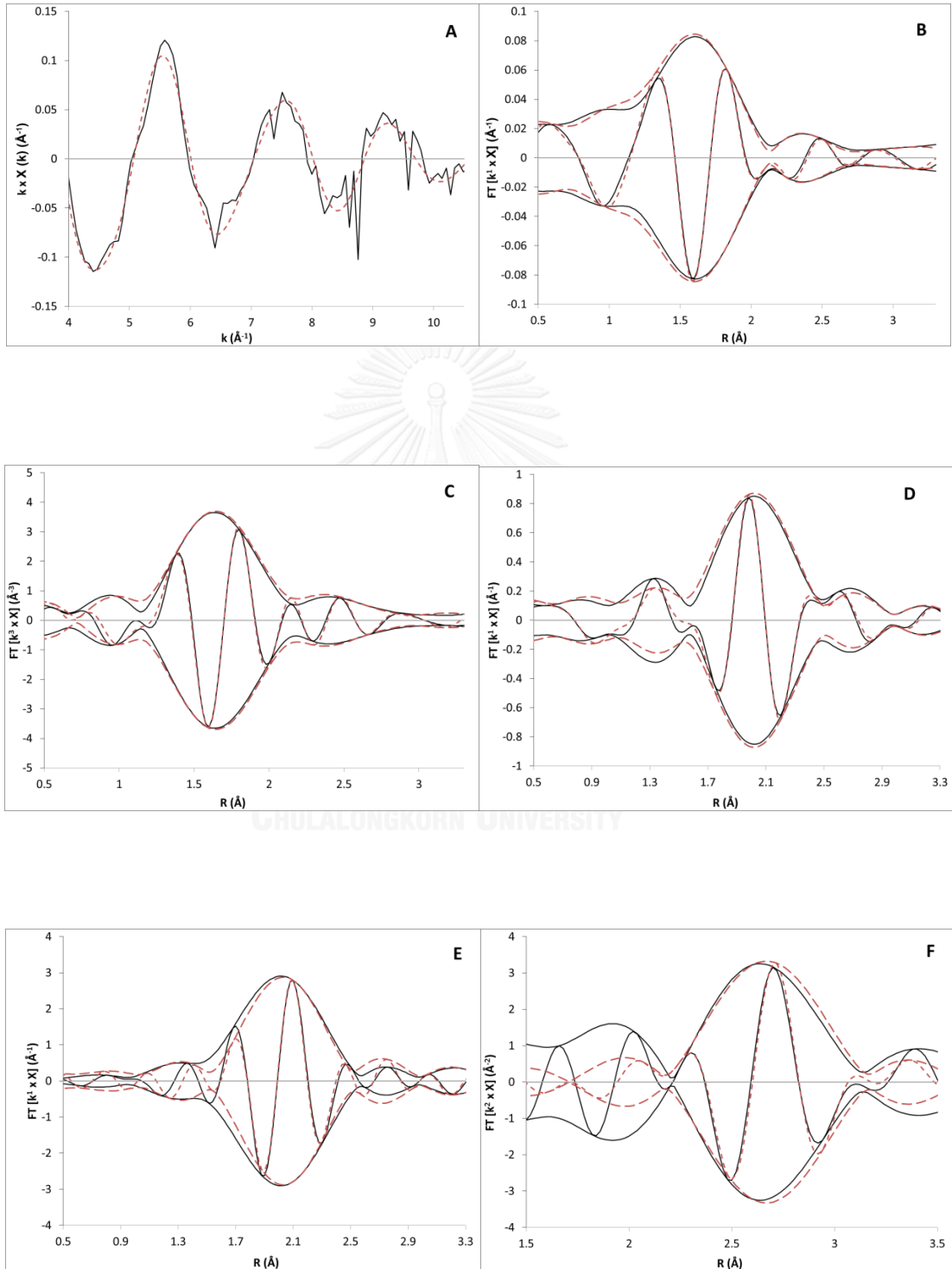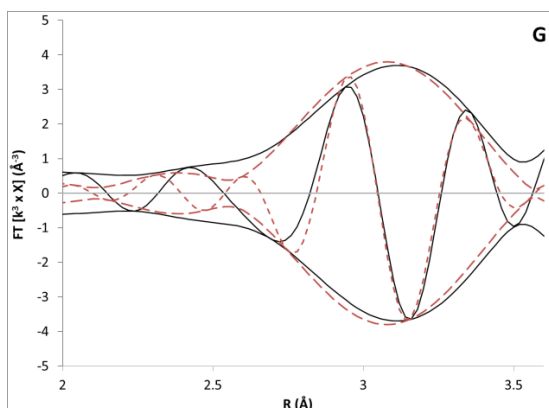
Figure G.1 EXAFS data recorded at the Pt L$_{III}$ edge characterizing sample formed by adsorption of Pt(NH$_3$)$_4$(NO$_3$)$_2$ in zeolite KLTL (Table 1, Sample 1) (A) k^1-weighted EXAFS function, $k^1(\chi)$ (solid line) and sum of the calculated contributions (dashed line); (B) k^1-weighted imaginary part and magnitude of the Fourier transform of the data (solid line) and sum of the calculated contributions (dashed line); (C) k^3-weighted imaginary part and magnitude of the Fourier transform of the data (solid line) and sum of the calculated contributions (dashed line); (D) k^1-weighted, phase- and amplitude-corrected imaginary part and magnitude of the Fourier transform of the data (solid line) and calculated contributions (dashed line) characterizing the Pt-N shell; (E) k^2-weighted phase- and amplitude-corrected imaginary part and magnitude of the Fourier transform of the data (solid line) and calculated contributions (dashed line) characterizing the Pt–O$_{support}$ shell; (F) k^2-weighted phase- and amplitude-corrected imaginary part and magnitude of the Fourier transform of the data (solid line) and calculated contributions (dashed line) characterizing the Pt-O$_{long}$ shell; (G) k^3-weighted phase- and amplitude-corrected imaginary part and magnitude of the Fourier transform of the data (solid line) and calculated contributions (dashed line) characterizing the Pt-Al shell (Δk = 4.0–10.6 Å^{-1}). The approximate experimental uncertainties are as follows: coordination number N, ±20%; R, ± 0.02 Å; $\Delta\sigma^2$, ±20%; and ΔE_0, ±20%. The terms are defined in the main text. The EXAFS data were fitted with 16 free parameters.
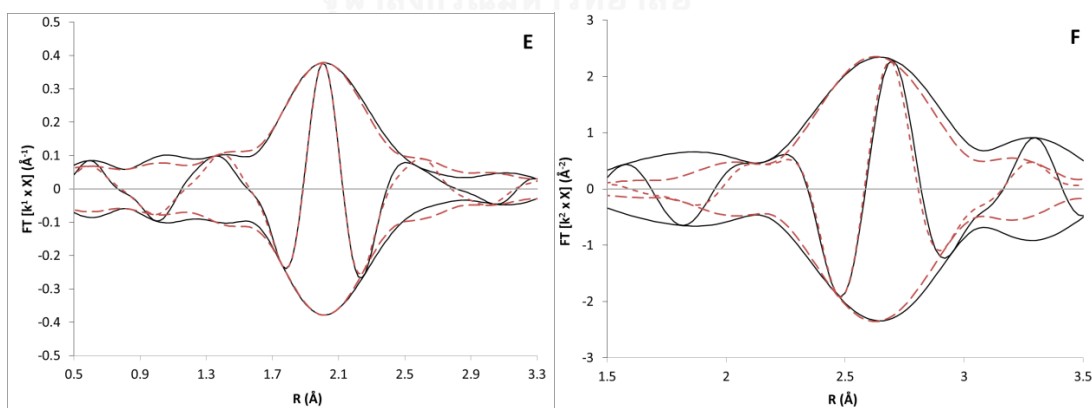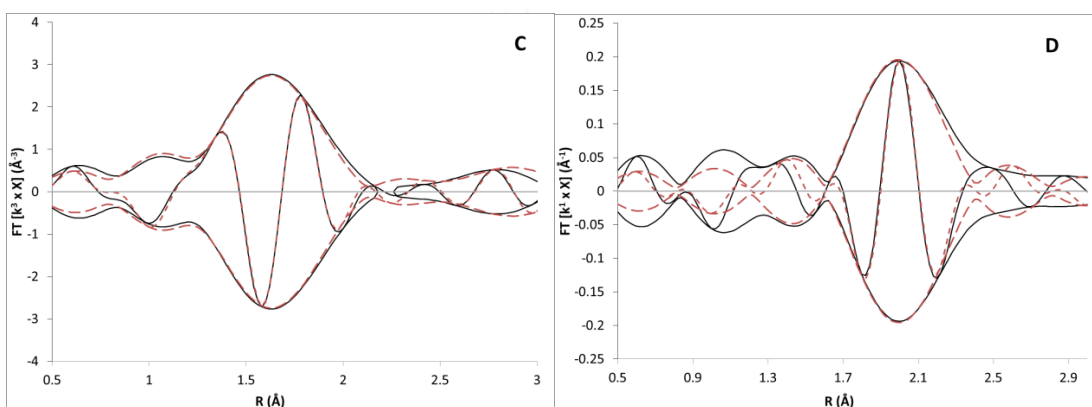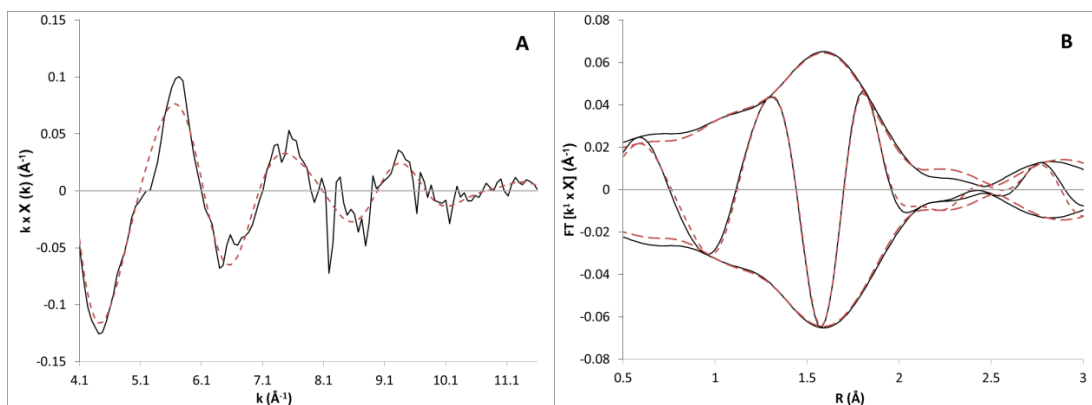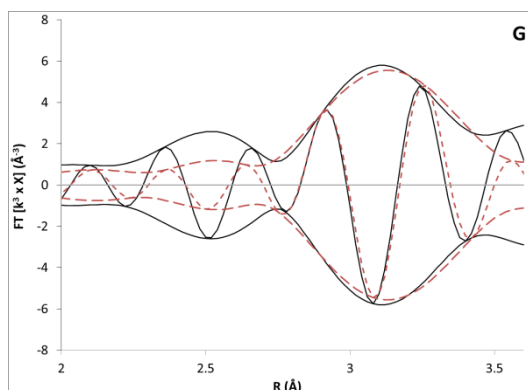
Figure G.2 EXAFS data recorded at the Pt L_{III} edge characterizing sample formed by adsorption of $Pt(NH_3)_4(NO_3)_2$ in zeolite K-LTL following treatment in 10% O_2 at 633 K for 4 h (Table 1, Sample 2)

(A) k^1-weighted EXAFS function, $k^1(\chi)$ (solid line) and sum of the calculated contributions (dashed line); (B) k^1-weighted imaginary part and magnitude of the Fourier transform of the data (solid line) and sum of the calculated contributions (dashed line); (C) k^3-weighted imaginary part and magnitude of the Fourier transform of the data (solid line) and sum of the calculated contributions (dashed line); (D) k^1-weighted, phase- and amplitude-corrected, imaginary part and magnitude of the Fourier transform of data (solid line) and calculated contributions (dashed line) characterizing the Pt-N shell; (E) k^2-weighted phase- and amplitude-corrected imaginary part and magnitude of the Fourier transform of the data (solid line) and calculated contributions (dashed line) characterizing the Pt–$O_{support}$ shell; (F) k^2-weighted phase- and amplitude-corrected imaginary part and magnitude of the Fourier transform of the data (solid line) and calculated contributions (dashed line) characterizing the Pt-O_{long} shell; (G) k^3-weighted phase- and amplitude-corrected imaginary part and magnitude of the Fourier transform of the data (solid line) and calculated contributions (dashed line) characterizing the Pt-Al shell ($\Delta k = 4.1–11.6$ Å^{-1}). The approximate experimental uncertainties are as follows: coordination number N, ±20%; R, ± 0.02 Å; $\Delta\sigma^2$, ±20%; and ΔE_0, ±20%. The EXAFS data were fitted with 16 free parameters.

Table G.1 EXAFS models considered for the as-prepared $Pt(NH_3)_4^{2+}$/KLTL zeolite sample.

The models were chosen for their potentially realistic coordination shells, and the fit with each was optimized to give the lowest goodness of fit, $(\Delta\chi)^2$, indicating the best agreement between the model and the data.

Sample	Coordination shell	N	R (Å)	$10^3 \times \Delta\sigma^2$ (Å^2)	ΔE_0 (eV)	$\Delta\chi^2$	Reasons for acceptance or rejection of model
Model 1: $Pt(NH_3)_4^{2+}$/ KLTL zeolite	Pt–N	4.0	2.00	4.2	-7.3	2.05	Model 1 has lowest value of goodness of fit parameter of all models and is therefore the preferred model. The ΔE_0 values were within a physically acceptable range. The model also includes coordination numbers that make good chemical sense, specifically including a Pt-N shell confirming the replacement of two NO_3 ligands with two support oxygen atoms as ligands upon adsorption of the precursor.
	Pt–O$_{short}$	2.0	2.05	2.3	8.0		
	Pt–O$_{long}$	6.0	2.68	7.0	3.7		
	Pt–Al	1.0	3.00	6.5	-11.0		
Model 2: $Pt(NH_3)_4^{2+}$/ KLTL zeolite	Pt–N	4.0	1.92	3.7	-8.2	3.68	Model 2 goodness of fit value is greater than those of Models 1 and 3. The ΔE_0 value characterizing the Pt-O$_{short}$ shell is high and slightly out of the acceptable range. The Pt-O$_{short}$ shell with a coordination number of 3.6 does not make good chemical sense without a change in the oxidation state of the platinum, for which there is no evidence.
	Pt–O$_{short}$	3.6	2.00	0.0	12.4		
	Pt–Al	1.1	3.05	5.0	-13.9		
Model 3: $Pt(NH_3)_4^{2+}$/ KLTL zeolite	Pt–N	3.7	2.00	4.2	-8.1	3.66	Model 3 goodness of fit value is greater than that of Model 1, indicating preference for the latter. Model 3 is similar to Model 1 in terms of coordination numbers of individual shells, but when a Pt-Al shell is not included (Model 3), the coordination number of the Pt-O$_{long}$ shell is increased by approximately 1, to a value of dubious meaningfulness, for which the ΔE_0 value is also high.
	Pt–O$_{short}$	2.0	2.05	5.3	7.9		
	Pt– O$_{long}$	6.9	2.62	6.5	12.6		

Table G.2 EXAFS models considered for the oxidized PtO_x/KLTL zeolite sample.

       The models were chosen for their potentially realistic coordination shells, and the fit with each was optimized to give the lowest goodness of fit, $(\Delta\chi)^2$, indicating the best agreement between the model and the data.

Sample	Coordination shell	N	R (Å)	$10^3 \times \Delta\sigma^2$ (Å^2)	ΔE_0 (eV)	$\Delta\chi^2$	Reasons for acceptance or rejection of model
Model 1: PtO_x/ KLTL zeolite	Pt–N	0.6	2.00	1.2	-1.8	2.53	Model 1 has lowest value of goodness of fit parameter of all models and is therefore the preferred model. The ΔE_0 values are within a physically acceptable range. The model also includes a Pt-N coordination shell which was demonstrated to be present by the IR data.
	Pt–O$_{short}$	2.8	2.01	8.9	-3.8		
	Pt–O$_{long}$	5.9	2.64	10.5	8.0		
	Pt–Al	1.1	3.19	2.6	11.3		
Model 2: PtO_x/ KLTL zeolite	Pt–O$_{short}$	3.1	2.01	7.1	-3.8	2.64	Model 2 goodness of fit value is greater than Model 1 and less than Model 3 values. The ΔE_0 value characterizing the Pt-O$_{long}$ shell is high and slightly out of the acceptable range. Coordination numbers of the three coordination shells are similar to those of Model 1. The Pt-N and Pt-O$_{short}$ coordination shells are of similar distance and can be fit as one shell here. However, IR data demonstrate the presence of the Pt-N shell, and so the model was not chosen. The comparison of the fits with Models 1 and 2 confirms the difficulty of distinguishing light backscatterers such as O and N with EXAFS spectroscopy.
	Pt–O$_{long}$	5.8	2.60	9.5	14.8		
	Pt–Al	1.1	3.19	2.0	10.8		
Model 3: PtO_x/ KLTL zeolite	Pt–N	0.5	1.99	0.7	3.5	7.65	Model 1 has greatest value of goodness of fit parameter of all the plausible models and therefore was not chosen. Model 3 is similar to Model 1 in terms of coordination numbers of individual shells, but when a Pt-Al shell is not included (Model 3), the coordination number of the Pt-O$_{long}$ shell is increased by approximately 0.5, to a value of dubious meaningfulness. Evidence of a Pt-Al shell is provided by the expected cationic character of the platinum complex (occupying a cation exchange site near Al in the zeolite).
	Pt–O$_{short}$	2.8	2.01	9.0	-3.5		
	Pt–O$_{long}$	6.5	2.64	9.6	7.8		

Figure H.1 IR spectra in v_{NH3} region characterizing $[Pt(NH_3)_4]^{2+}$ complexes supported on K-LTL zeolite before (upper curve) and after oxidation (lower curve).
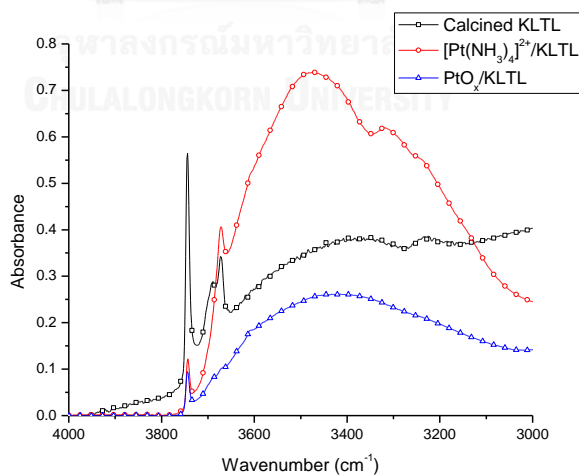
Figure H.2 IR spectra in v_{OH} region characterizing bare KLTL zeolite and $[Pt(NH_3)_4]^{2+}$ complexes supported on KLTL zeolite before and after oxidation.
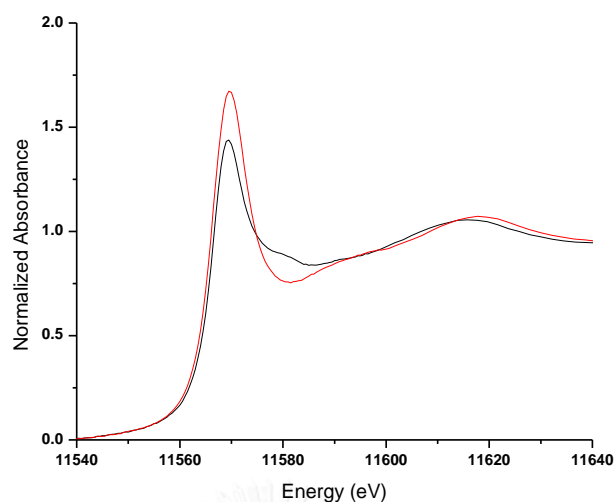
Figure H.3 Pt L_{III} edge XANES characterizing $[Pt(NH_3)_4]^{2+}$ complexes supported on KLTL zeolite before (black) and after oxidation (red).
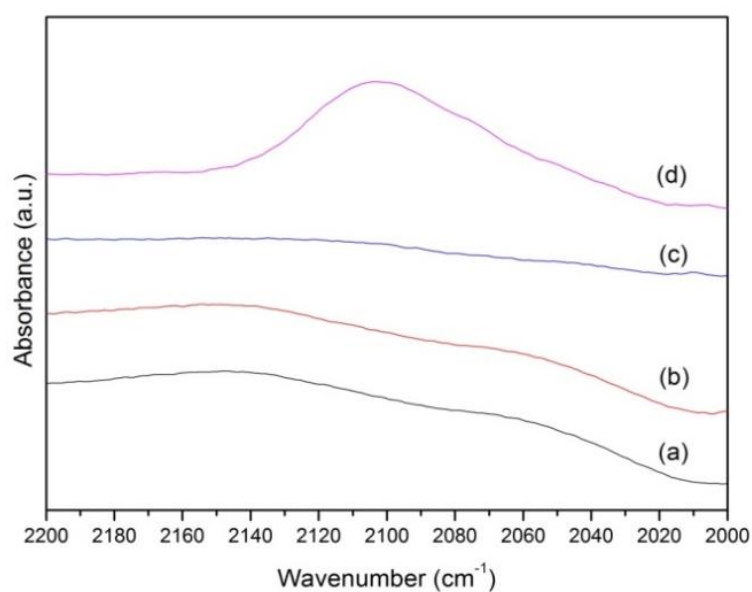
Figure H.4 IR spectra in the v_{CO} stretching region characterizing (a) $[Pt(NH_3)_4]^{2+}$/KLTL zeolite, (b) $[Pt(NH_3)_4]^{2+}$/KLTL zeolite after exposure to a CO pulse, (c) PtO$_x$/K-LTL zeolite, and (d) PtO$_x$/KLTL zeolite after exposure to a CO pulse.
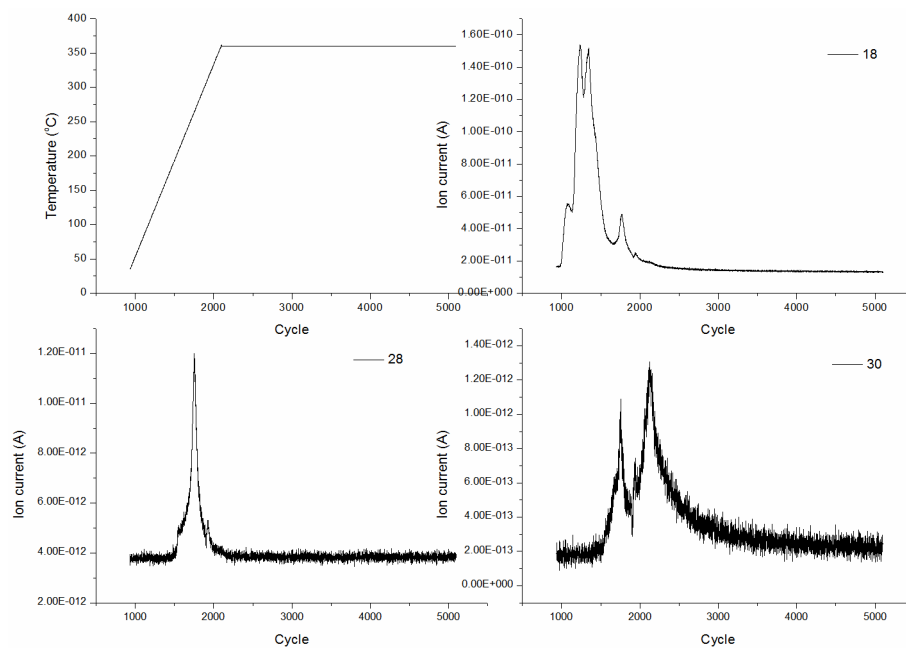
Figure H.5 Mass spectroscopy (a) $[Pt(NH_3)_4]^{2+}$/KLTL zeolite, (b) $[Pt(NH_3)_4]^{2+}$/KLTL zeolite after exposure to a CO pulse, (c) PtO_x/K-LTL zeolite, and (d) PtO_x/KLTL zeolite after exposure to a CO pulse.

Table H.1 Examples of CO bonded to platinum species including IR band locations in the υ_{CO} region.

Species	Frequencies (cm^{-1})	Support	Conditions	Reference
O–Pt–CO	2120	Al$_2$O$_3$	CO + O$_2$, 298 K	[144]
Pt^{2+}–CO	2110	NaY zeolite	Pco: 72–76 kPa, 353 K	[145]
Pt$^{\delta+}$–CO	2100-2120	NaY zeolite	298 K	[146]
Pt$^{\delta+}$–CO	2126	KLTL zeolite	298 K	[147]
Pt$^{\delta+}$–CO	2100-2120	KLTL zeolite	298 K	[148]
Pt–CO	2070-2076	Pt(111) (110)	UHV	[149]
Pt–CO	2095	Pt(111)	UHV	[150]
Pt–CO	2100	Al$_2$O$_3$	300-460 K	[151]
Pt–CO	2083	Al$_2$O$_3$	Pt crystal faces, 423-523 K	[152]
Pt–CO	2025-2090 (HF) 2000-2025 (LF)	NaX zeolite	HF d_{Pt} >1.2 nm LF d_{Pt} < 1.2 nm	[153]
Pt–CO	2075-2090 (large particle) 2066, 2051, 2031	KLTL zeolite	300 K	[154]
Pt^{2+}–CO	**2100**	**KLTL zeolite**	**298 K**	**This work**

APPENDIX I
COMPARISON TOF VALUES FOR CO OXIDATION OF
SUPPORTED PLATINUM CATALYSTS

Table I.1 Comparison TOF values of supported platinum catalysts for CO oxidation. Data shown were recorded at atmospheric pressure.

Sample	Feed Composition (% by volume)	Pt loading (wt%)	CO Oxidation Temperature (K)	TOF x 10^2 (s^{-1})	Reference
Pt/Θ-Al$_2$O$_3$	3.7% CO 3.7% O$_2$ 93.6% He	0.18	473	1.3	[103]
			524	18.7	
		1.0	473	1.4	
			485	3.4	
		2.0	473	5.1	
			455	1.7	
Pt/Al$_2$O$_3$	2.67% CO 1.33% O$_2$ 97.0% He	0.4	423	0.36	[155]
Pt/SiO$_2$		5.0	423	0.072	
Pt/SiO$_2$	1% CO 10% O$_2$ 89.0% He	2.0	403	0.8	[156]
Pt/FeO$_x$	1% CO 1% O$_2$ 98% He	0.17	300	13.6	[42]
Pt/TiO$_2$	1% CO 99% Air	0.5	300	0.90	[157]
		1.0	300	0.38	
Pt/CeO$_x$/Al$_2$O$_3$	2.67% CO 1.33% O$_2$	0.4	323	0.29	[155]
[Pt(NH$_3$)$_4$]$^{2+}$ /KLTL	**1% CO 5% O$_2$ 94% He**	**1.0**	**423**	**0.38**	**This work**
PtO$_X$ /KLTL		**1.0**	**423**	**1.20**	**This work**

VITA

Mr. Nutchapon Chotigkrai was born on April 20, 1988 in Nakhon Pathom, Thailand. He graduated high school from Phrapathom Witthayalai School in 2006. He received the Bachelor's degree in Chemical Engineering from Silpakorn University in March 2010. He consequently continued studying Doctoral degree of Engineering in Chemical Engineering at Chulalongkorn University since June 2010 and received a scholarship from the Royal Golden Jubilee PhD program of Thailand Research Fund (TRF). He had joined Professor Bruce C. Gates' group as a visiting scholar for a year (November 2012 – November 2013) at University of California, Davis, United States of America.